A Platform for Microbial Evolution and Characterization

Chris N. Takahashi

A dissertation
submitted in partial fulfillment of the
requirements for the degree of

Doctor of Philosophy

University of Washington

2015

Reading Committee:

Eric Klavins, Chair

Maitreya Dunham

Georg Seelig

Program Authorized to Offer Degree:
Electrical Engineering

University of Washington

Abstract

A Platform for Microbial Evolution and Characterization

Chris N. Takahashi

Chair of the Supervisory Committee:
Associate Professor Eric Klavins
Department of Electrical Engineering

In this document we describe a novel platform for the engineered evolution of microbes. Our platform consists of three major components, which we discuss in subsequent chapters.

Technology: We have developed a novel continuous culture device called the Flexostat. The Flexostat is a flexible, programmable, eight chamber, turbidostat with multiplexed fluidics. The design of the Flexostat is open sourced and has accompanying detailed assembly instructions. Modularity of the design also enables users to rapidly create derivative devices without needed to adapt unrelated components of the device.

Cell Chassis: While the majority of laboratory strains of *S. cerevisiae* do not form biofilms or flocs. Unfortunately, *E. coli* does form robust biofilms. To compound this, continuous culture and turbidostats in particular select strongly for biofilms as they are immune to washout. We have developed a new, MG1655 derived, strain of *E. coli* that does not form biofilms. The inability of our strain to form biofilms enables longterm evolution and characterization experiments in *E. coli*.

Theory: We develop a stochastic hybrid systems model for evolution in a turbidostat. With our model we show that there exists an optimally challenging environment as well as optimal population size for single evolutionary steps. We also use insights gained from our model to develop a control strategy for accelerated evolution in parallel turbidostats and demonstrate it's utility in a randomly generated model system.

At the time of this writing, the Flexostat or derivative has been built in over a dozen labs at institutions including the Massachusetts Institute of Technology, California Institute of Technology, Rice, University of California San Diego, and three companies, DuPont, Bolt Threads, and Arzeda.

TABLE OF CONTENTS

Page

LIST OF FIGURES

ACKNOWLEDGMENTS

I thank my thesis advisor, Prof. Eric Klavins for all his advice and support. Over the years of my graduate career I have learned much from him. He helped bootstrap my foray into synthetic biology from control theory, and fostered the communication skills that got me where I am today and will carry me into my future as a scientist and engineer. Most of all, he has taught me the value of collaboration, without which none of my work would have been possible. I also thank members past and present of the Klavins lab including, Josh Bishop, for being the first to expose me to synthetic biology as an undergraduate; David Thorsley, for his insights into dynamical systems and statistics; Rob Egbert, for his help designing experiments and formulating synthetic biological projects; Kevin Oishi, for his knowledge of systems theory and early advice about graduate school; Yaoyu Yang, for his hard work on Aquarium; Felix Ekness, for the awesome fluorostat he built; Tileli Amimeur, for our discussions on machine learning, and cat photos; Leandra Brettner, for her thoughts on evolution and being my BEACON buddy; David Younger, for his help framing and communicating difficult ideas with ease; Sunny Rao, for her science outreach leadership and constant supply of candy; Nick Bolten, for great discussions about programming and figure refinement; and Miles Gander for feedback on various talks. Special thanks to my lab-mate, friend, and cohort Shelly Jang, not only for many fruitful discussions, but also for her invaluable camaraderie which kept me going during difficult times.

I also thank my world-class committee members Maitreya Dunham, Ben Kerr, and Georg Seelig. My work has been much improved due to their feedback, comments, and discussions. I look forward to continued collaborations.

Outside of the Klavins lab I thank Luis Zaman for his deep understanding of evolution and many great discussions (on all topics); Anthony LaMarca and Jeffrey Scofield for "coffee time"; and the Flexostat early adopters and adapters, including Prof. Jeff Tabor and Evan Olson for their help documenting, debugging, and evangelizing.

Finally I thank my parents Terry and Binky Takahashi for their support and most importantly my loving wife Elaine, without whom none of this would be possible.

DEDICATION

To my mother, father, and dear wife Elaine.

Chapter 1

BACKGROUND AND MOTIVATION

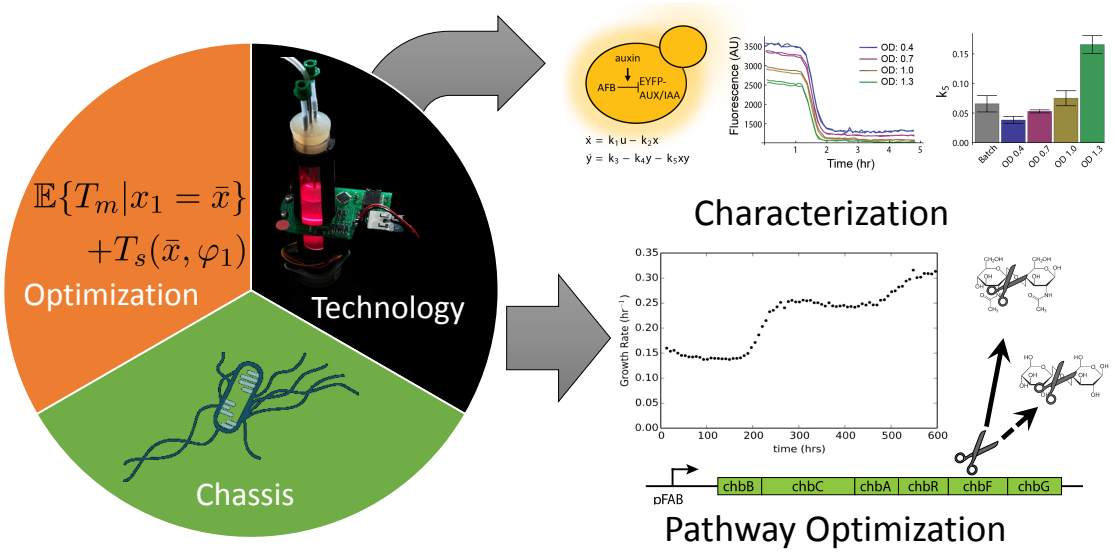

Figure 1.1: Our platform consists of three core components. The first component is the Flexostat, a parallel continuous culture technology that enables feedback controlled culture conditions. The second component is a cell chassis strain of *E. coli* that grows without biofilms in continuous culture. The third component is an optimization theory and control algorithm that informs the choice of culture conditions for rapid evolution. These components form a platform that can be used for rapid laboratory evolution. Additionally, the Flexostat may be used for characterization of synthetic systems in microbes where a constant environment is important.

Recently, there has been much interest in using biology to solve pressing human problems such as carbon fixation, bioremediation, biofuel production, and drug and chemical synthesis [4,5]. These process involve starting with a low value feedstock, which is used as the carbon source for a microbial community. The microbes then use the energy they extract from the feedstock to create useful byproducts. Often the carbon source of interest (such as cellulose

or formate) is not metabolizable by *E. coli* or other easily engineered organisms. Therefore, a synthetic pathway that converts the feedstock to a utilizable intermediate is used to enable growth.

The enzymes for synthetic pathways either come from foreign organisms or they are engineered *de novo*. Either way, the pathways are not initially optimal. A pathway of one enzyme needs only its expression level tuned. Two enzymes need their expression and ratio tuned. Three enzymes need three quantities tuned, and so on. In general, as you increase the number of steps in a metabolic pathway, the dimensionality of the tuning problem increases proportionally. To combat this, protein engineers measure kinetic rates, make models, and find theoretically optimal expression levels. They then use this information to choose DNA sequences that are predicted to give the desired expression levels. Finally, these sequences are synthesized and cloned into a vector. Unfortunately, even with the best characterization, modeling, and prediction, expression usually varies significantly from the expectations due to the context dependence of gene expression [6].

Tuning of metabolic pathways must inevitably be done *in vivo*. The exact methods vary but typically involve creating a diverse library of mutants and screening for high performers. This process, generally called directed evolution [7], can be a laborious requiring the experimenter to manually clone in variation and screen hundreds or thousands of clones. In contrast to directed evolution, this work is motivated by the idea that metabolic pathways can be optimized through "hands off" evolution in an engineered context. Specifically, we rely on mutations that occur without manual intervention, either naturally or due to genomic modifications such as the knockout of DNA mismatch repair [8]. Furthermore, we consider an engineered environment to influence the trajectory of natural selection rather than manual screening.

The use of laboratory evolution for engineering brings up a natural set of questions. In particular, this document addresses questions surrounding optimizing hill climbs such as what culture method is fastest? How do you make such an environment? Does population size matter? How challenging should the environment be? Do parallel evolutions speed up the rate of discovery? In the following chapters we will address these questions.

In this work we present answers to the above questions and compose a platform for

microbial evolution that consists of technology, biology, and theory (Figure 1.1). The technology consists of an open source bioreactor called the the Flexostat. In order to enable the use of the Flexostat with *E. coli*, we have developed a novel anti-fouling strain. Finally, we develop a theory and an algorithm for optimizing the rate of evolution in the Flexostat.

In chapters 2 and 3, we discuss the Flexostat, a novel continuous culture device that addresses the question of what culture method should be used and the specifics of design, build, and characterization of one such device. The Flexostat is an open source, flexible, multiplexed turbidostat that can be built using a combination of 3rd party services and simple tools. While batch culture is used extensively in laboratory evolution, it suffers from the uncontrolled change in environment that happens as a result of cell growth. Eventually the cells reach stationary phase and growth stops until an experimenter can dilute the culture. The changing environment of batch not only gives the process of evolution a "moving target," but also limits the effective population size to the amount transferred during serial dilution and number generations per day to $\log_2$ of the dilution factor. The Flexostat addresses the limitations of batch culture by growing cells continually at constant density allowing both longterm evolution and a stable environment for characterization of synthetic circuits.

In chapter 4, we develop a cell chassis strain of *E. coli* that does not form biofilms. Biofilm formation in continuous culture is counterproductive because it provides an alternative evolutionary path to improve fitness by avoiding washout rather than outgrowing planktonic competitors. Additionally, biofilms provide spacial structure leading to heterogeneous cultures, which are difficult to model and characterize.

In chapter 5, we present a model for studying evolution in the Flexostat. We use our model to develop an optimal choice of environment and population size to maximize the rate of a single evolutionary step. Applying the same model to multiple evolutionary steps we then develop a set of heuristics for optimizing evolution in parallel cultures where the landscape is not known.

In the remainder of this chapter, we provide a brief review of the background necessary understand the results presented in later chapters.

1.1 Continuous Culture

The first continuous culture device was the *chemostat* [9]. In a chemostat, the dilution rate and media source are constant over the course of an experiment. The constant dilution rate of a chemostat leads to one of two steady states. If the dilution rate out paces the maximal growth rate of the cultured cells, then the population will decline and approach zero. The dilution rate (in volumes per hour) equal to the growth rate is referred to as the *washout rate*, as higher dilution rates will wash cells out of the culture chamber. Below the washout rate cells consume nutrients until the concentration of some limiting nutrient (typically, but not necessarily, the carbon source) has been depleted to the point where the growth rate is equal to the dilution rate. Since chemostats always operate in a nutrient limited regime they excel at optimizing towards efficient utilizers and good importers, but this same feature makes it difficult to study populations that are not nutrient limited.

To address the shortcomings of a chemostat, the *turbidostat* was invented [10]. A turbidostat is a device similar to a chemostat except the dilution rate is feedback controlled. In a turbidostat, a sensor measures optical density (turbidity), which is directly proportional to cell density, and the dilution rate is controlled to follow a desired turbidity. As elaborated in Chapter 5 both the turbidostat and chemostat have the conserved quantity $s + \frac{1}{\gamma}x = C$ where s is the substrate concentration, x is cell density, C is the concentration of input substrate, and γ is the conservation constant. This implies that for low cell densities in a turbidostat $s \approx C$ making defining the chemical environment equivalent to defining the input medium.

Presently, new sensors and devices, the advent of computer control, and new fabrication techniques have enabled or simplified the construction of a wide array of new devices including the adaptastat, PACE machine, ministat, etc [11–18]. The breadth of devices is a testament to the creativity of scientists and engineers developing the vast array of needs presented by each new experiment. These devices also highlight the need for flexibility and open design in tools as new applications cannot be anticipated. In Chapters 2 and 3, we present our contribution, the Flexostat, which addresses the need for a flexible device while also lowering the barrier to entry.

1.2 Adaptive Laboratory Evolution

Adaptive Laboratory Evolution (ALE) is a term that describes evolution of microbial populations as they adapt to environmental stress in a laboratory [19]. ALE is usually accompanied by regular collection of population samples and the use of next-generation DNA sequencing technology to monitor and understand the path of evolution. It has been used with much success to add to our understanding of microbiology and as synthetic biology and metabolic engineering are becoming increasingly relevant it has the potential to become increasingly relevant for engineering.

There is a large body of literature on evolution and laboratory evolution. The majority of modeling work in this area presents models that attempt to capture, explain or predict phenomenology. Unfortunately, most models do not provide much insight into optimizing the rate of evolution for the sake of engineering. Here, we will describe some of the related literature.

An important illustration of a gene's fitness contribution as a function of the environment was given by Uri Alon et al. [20] Alon measured the fitness penalty associated with producing proteins in the lac operon as well as the fitness benefit of digesting lactose at different concentrations. He then grew populations of *E. coli* in IPTG(a lactose analog) and varying concentrations of lactose for 80 days, diluting 1:100 each day. Alon hypothesized that there would be a natural equilibrium where just enough enzyme would be made to digest the available lactose, but no extra resources would be spent producing unneeded proteins. Indeed, he found that after approximately 200 generations each culture had adapted.

Alon et al. also demonstrated that varying the environment toward and *away* from the desired goal can speed up evolution [21]. Using a computer model, Alon showed that changing goals caused a traversal through a fitness landscape that was actually able to jump between plateaus in fitness. This evidence motivates us to examine systems where the environment can be change to steer evolution between local fitness maxima.

Fisher gave a geometric argument that smaller mutational steps (normalized by distance to optimum) had a higher probability of being beneficial, with a 50% chance of being beneficial as the step size approached zero [22]. This implies that in a static environment,

there will almost always be a next evolutionary step. In contrast to Fisher's theory, Gillespie modeled adaptive walks using extreme value theory (EVT, a branch of probability theory concerned with only the most extreme values drawn from a distribution) to choose the next fitness. He showed that adaptive walks would, on average, consist of only a small number of steps (less than five) [23].

In a continuing twenty-year experiment, Richard E. Lenski has grown 50,000 generations of *E. coli* in batch culture, which has generated an extensive body of work [24]. Lenski observed a near-constant rate of evolution over 20,000 generations of *E. coli* over which fitness increased. This contradicts theoretical findings that imply that adaptive walks terminate quickly [23] and imply that even rugged fitness landscapes may be traversable given their high dimensionality (the typical 3-D visualization of a fitness landscape leads to the incorrect intuition that there are very few mutational neighbors, or that many mutational neighbors are similar). It is worth pointing out that using continuous culture we could do in two years what took Lenski twenty.

Chapter 2

THE FLEXOSTAT

The characterization of biological building blocks and complex synthetic systems is fundamental to synthetic biology [25, 26]. Historically, characterization of biological systems has been carried out using batch culture methods [1, 27–32]. The low cost, ease of culture propagation and scalability through use of well plates and culture flasks have contributed to the prevalence of this culture method. However, in batch culture the chemical environment is continually changing as cells grow, divide, consume nutrients, and excrete waste products [33]. These changes associated with growth have substantial effects on cellular physiology [34–36] and engineered biological components, which can in turn cause the mischaracterization of a system's input-output response or require the consideration of uncontrolled disturbances to the system.

To more accurately characterize biological systems, researchers must turn to static environments, which yield lower noise in quantitative phenotyping. A primary tool for culturing cells in a static environment is continuous culture, where inoculated growth medium is continually diluted with fresh medium. At steady state, a continuous culture device will dilute cells and waste products at the same rate that they are being produced leading to an unchanging environment [37, 38].

Two main categories of continuous culture devices are chemostats and turbidostats. Chemostats dilute liquid culture at a fixed rate and reach steady state when a limiting nutrient has been depleted, or toxins have been accumulated, at which point the growth rate is equal to the dilution rate. Therefore, chemostats are ideal for interrogating the effects of nutrient limitation or where defined growth rates are desired. In contrast, turbidostats use a feedback control loop to keep cell density constant; in a turbidostat, the cell density is continually monitored and used to compute the dilution rate that achieves a prespecified cell density. Thus, turbidostats are ideal for characterization of systems without nutrient

limitation, when cells are growing at their maximum rate.

In spite of the advantages, use of chemostats and turbidostats is not commonplace. Factors that limit the use of continuous culture systems include the fact that commercially available bioreactors either lack feedback capability, have such large volumes that dilution rates needed to sustain a log phase culture would be impractical, or are prohibitively expensive. As a result, researchers often design their own turbidostats which vary widely in implementation based on the needs of the experimenter [11–18]. Unfortunately, the design and construction can be laborious and uncertain. Design decisions that are seemingly innocuous can lead to failures or inflexible devices. Furthermore development of turbidostats requires specialized knowledge of electrical and computer engineering, which has further limited their popularity.

We have developed an open source turbidostat design (the Flexostat) that contrasts with other publicly available continuous culture devices [13, 15, 39]. Using common hand tools and standard laboratory equipment combined with inexpensive online or university provided fabrication services and 3D printing, our instrument can be built for under $2000 USD. Indeed, many individuals from a wide range of backgrounds have already built turbidostats from our design. Currently, five laboratories have at least one complete instrument (see acknowledgments), some with custom modifications. As part of our commitment to the community, the authors will continue to contribute updated designs to the website and ask, but do not require, that all derived designs be submitted so that the community may benefit.

The Flexostat implements eight parallel culture chambers, which enable users to gather replicate data and perform parallel experiments requiring no extra pumps or controllers. Each chamber contains electronics that enable distributed sensing and mixing control allowing users to add new chamber modules with new capabilities with minimal hardware redesign. A platform agnostic Python program collects data from each chamber and computes dilution rates through a user programmable function.

To demonstrate the utility of our device over standard batch culture, we recharacterized part of the auxin plant hormone pathway cloned into *S. cerevisiae* and grown at various constant cell densities. Previous work has characterized the interactions between the small

molecule auxin and the family of F-box proteins in batch culture resulting in a table of key parameters for each interaction [1]. Here, we show that one of these parameters, a degredation rate in the presence of auxin that was previously considered a constant, varies by more than four fold depending on the cell density.

Finally, we showcase how the modular design and 3D printed nature of the Flexostat allows us to add new capabilities. In particular, we show a proof of concept single chamber, mixture controlled variant that is capable of detecting strongly fluorescent cultures (the Fluorostat) such as *E. coli* expressing super folder GFP. Fluorescence detection is accomplished through the addition of a single blue excitation source and a pair of low cost, spectrally orthogonal filters. The light sources for the OD measurement and fluorescence measurements alternate in time and share the same photodetector. The dual use of the photosensor allows us to use the same electronics for the standard Flexostat and the Fluorostat, requiring that only software and a single 3D printed part be changed.

2.1 Results and Discussion

Theory of Operation

The operation of the Flexostat (Figure 2.1) consists of a discrete dilution cycle with an adjustable period (typically one minute). First, the current optical density of each chamber is measured. Then, for each chamber, a user-programmable Python module computes the dilution rate as a function of error between desired OD and measured OD. The dilution rates, which may be different for each chamber, are then sent to the embedded circuitry, which controls the media pump and valve system. As new media is added, it is mixed by magnetic stir bars diluting old media, cells, and waste products. When the media level rises to the mouth of the effluent tube waste it is forced out by positive pressure provided by an aeration input.

Specifications and Characterization

Biochemical reactions in cells are highly sensitive to experimental preparation, equipment variation, and environmental changes. Indeed, some systems even have multimodal steady

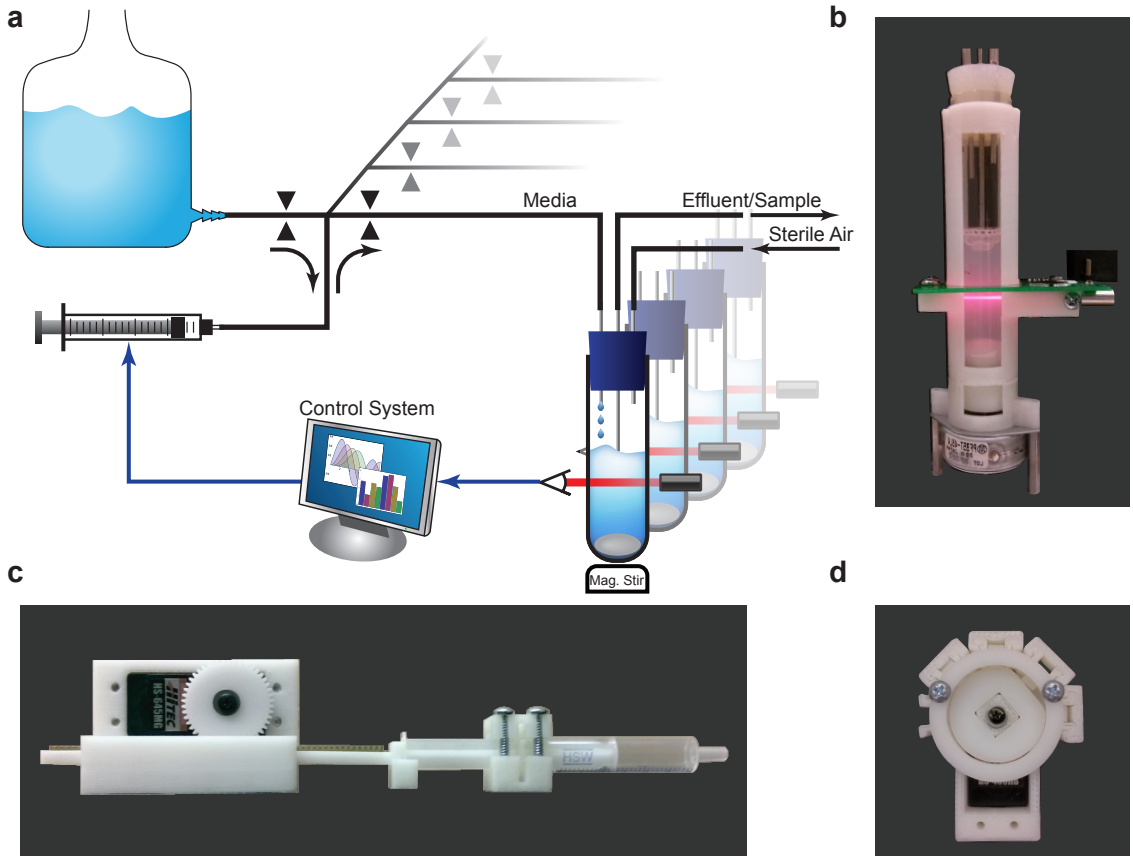

Figure 2.1: (a) A schematic of the Flexostat. OD is measured through the chamber wall and reported to a control system. A dilution rate is then calculated for each chamber, which is carried out by the pumping system. Valves select the flow source or destination while a single multiplexed syringe pump determines the volume and direction of flow. (b) A photograph of the turbidostat chamber with integrated OD measurement and stirring. (c) A 3D printed syringe pump. (d) A 3D printed four way normally-closed pinch-valve with the upper right valve selected.

state distributions [40] which are sensitive to initial conditions and require replicates to thoroughly probe. Furthermore most experimental outcomes must be compared to those of a control experiment or between multiple variants. In a single chamber turbidostat, each replicate and control must be performed serially, which is time consuming and susceptible to day to day variations in experimental conditions. For the Flexostat, we choose to multiplex

eight culture chambers into the same media source and pump, which allows us to perform eight experiments in parallel, all of which are subjected to the same conditions. A single multiplexed pump has the additional advantage lowering cost relative to buying eight pumps.

In the continuous culture literature, culture volumes can range from a few femto-liters [41] to industrial fermenters containing thousands of liters of media. The culture volume has logistical impacts that need to be carefully weighed. Yeast in rich media go through approximately 16 generations in a day if kept at maximal growth rates. Since one volume must be replaced for every generation and there are eight culture chambers, 16 generations/day/chamber $\times$ 1 volume/generation $\times$ 8 chambers = 128 volumes per day will be consumed, which quickly adds up for large culture volumes. Small volumes also have drawbacks. If sampling is required for characterization enough effluent must be available for a single measurement. A typical flow cytometer for example requires at least 50 µL for measurement [42]. Sampling the 50 µL required for flow cytometry from a 1 mL vessel would require close to five minutes of collection time from effluent. We have found that a culture volume of 15 mL is a good balance allowing for enough effluent to be collected over a sample period of two minutes while limiting the amount of media used to less than 2 L a day.

For characterization in replicate, all chambers must measure OD uniformly. Commercial OD probes are too large to fit into a 15 mL volume without interfering with other essential processes (e.g. stirring, dilution, etc.), so we developed a customized solution. We measure optical density through the walls of the culture tube using a 650 nm laser diode, similar to those found in common laser pointers, and a pair of photo sensors configured to reject changes in transmitted light intensity caused by temperature variation and electrical noise (Figure 2.2). Tests with reference medium consisting of black dye, which has an absorbance spectrum similar to *E. coli* (in the 500-700nm range), show chamber to chamber variation of less than $\pm 2.5\%$. For further characterization information including noise, linearity, and detection threshold see supporting section B.2.

A large component of the cost of a continuous culture device is the pump. In the Flexostat we multiplexed a single syringe pump that feeds all eight chambers (Figure 2.1). A multiplexed pump saves the cost of seven additional pumps, and reduces the number of valves needed from 16 to 9. To further reduce the cost we have designed a 3D printed syringe

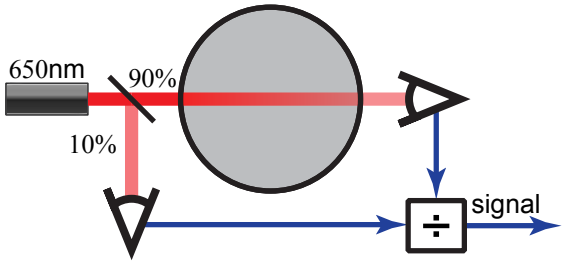

Figure 2.2: In each chamber, a laser diode emits a 650 nm beam that is then split two ways. Approximately 10% of the light is sent to a photosensor used to measure noise while the remaining 90% is used to measure light transmitted through the cell culture. The ratio of these two signals is a linear function of the transmitted light, which is then normalized to a blank measurement and log transformed to obtain the optical density.

pump which may be used in place of a commercial syringe pump. These two strategies have reduced pumping costs by 96% compared to designs that utilize commercial peristaltic pumps.

Modeling and Programming

A continuous culture device can be modeled by a simple set of ordinary differential equations (ODEs) [37],

$$\begin{aligned} \dot{x} &= \varphi(s)x - xu \\ \dot{s} &= -\varphi(s)x\gamma^{-1} + (s_0 - s)u, \end{aligned} \tag{2.1}$$

where $x(t)$ is the cell mass, $s(t)$ is the mass of substrate, s_0 is the substrate concentration of the feedstock, $\varphi(s)$ is the growth rate, γ is the growth yield in biomass per substrate mass, and u is the dilution rate. It is worth noting that the units of x can be substituted by OD, which only changes the units of γ to OD per cell mass.

If a turbidostat's setpoint is too close to the maximal cell density, γs_0, then it is possible that slight variations in media, conditions, or cell morphology may cause large changes in dilution rate, or even prevent dilution entirely. More formally, if we assume the growth rate

as a function of substrate concentration is a Hill function without cooperativity [33]

$$\varphi(s) = \frac{\varphi_{max} s}{(k+s)},$$

with max growth rate φ_{max} and half maximum constant k, we can examine the sensitivity to substrate concentration

$$\frac{d\varphi(s)}{ds} = \frac{\varphi_{max} k}{(k+s)^2}, \tag{2.2}$$

which rises sharply as the substrate mass goes to zero. The high sensitivity to low substrate concentrations makes running a turbidostat in nutrient limited regimes impractical. Difficulty maintaining setpoints near the maximal OD is analogous to the difficulty chemostats have maintaining setpoints near the washout rate.

Assuming cultures will be run sufficiently far from maximal densities, where substrate is not limiting, we can assume a nearly constant growth rate allowing us to simplify the model further

$$\dot{x} = \varphi x - xu. \tag{2.3}$$

Furthermore, because a turbidostat's culture is always near its reference point r, the bilinear model (2.3) can be further simplified to a linear model around the operating point $(x^*, u^*) = (r, \varphi)$:

$$\dot{x} = -ru. \tag{2.4}$$

As stated earlier, turbidostats maintain cell density through feedback control. We have chosen the proportional plus integral feedback controller [43]

$$\begin{aligned} u &= k_p x + k_i z \\ \dot{z} &= x, \end{aligned} \tag{2.5}$$

where k_p and k_i are proportional and integral gains, respectively. This controller eliminates

any steady state error in optical density and yields the system

$$\begin{aligned} \dot{x} &= -r(k_p x + k_i z) \\ \dot{z} &= x. \end{aligned} \tag{2.6}$$

System (2.6) can oscillate when the condition $rk_p^2/(4k_i) > 1$ is not met. To prevent oscillations we assume that the minimal OD setpoint will be 0.1 ($r > 0.1$) OD units and pick k_p and k_i so that $rk_p^2/(4k_i) = 5 > 1$. Indeed, gains so chosen have yielded robust, non-oscillatory OD signals with the Flexostat.

To measure error and validate the controller in the implemented system, we grew *S. cerevisiae* in duplicate at four different optical densities and quantified the average, maximum, and 95th percentile tracking error (difference between set OD and measured OD) over a period of 22 hours. Average tracking error was no more than 3.14×10^{-4} OD units between all eight chambers while the maximum error observed at any time point was $\pm 4.8 \times 10^{-3}$ ODs with 95% of the error inside of $\pm 2.3 \times 10^{-3}$ ODs. Thus, accurate maintenance of a desired OD set-point is achievable over experimentally relevant time periods.

Since the Flexostat is programmable through a Python application program interface (API) it can also be easily reprogrammed for different objectives (see supporting information section B.1 for details). Dilution and feedback can be turned off allowing for the measurement of growth curves in the same device (Supporting Figure B.3), which can be useful for determining batch growth rates and growth yields. It can also be programmed to follow arbitrary reference trajectories so long as they are physiologically feasible (Figure 2.3).

Gene Network Parameter Dependence on Cell Density

In previous work [1], we studied the auxin plant hormone pathway cloned into *S. cerevisiae*. In our engineered yeast strain, as *in planta*, indole-3-acetic acid (auxin) promotes the interaction between a member of the F-box family of plant proteins (AFBs) and a member of the Aux/IAA family of plant proteins. AFBs target our engineered EYFP-Aux/IAA proteins to promote degradation via the proteasome (Figure 2.4a). In yeast transformed with a mem-

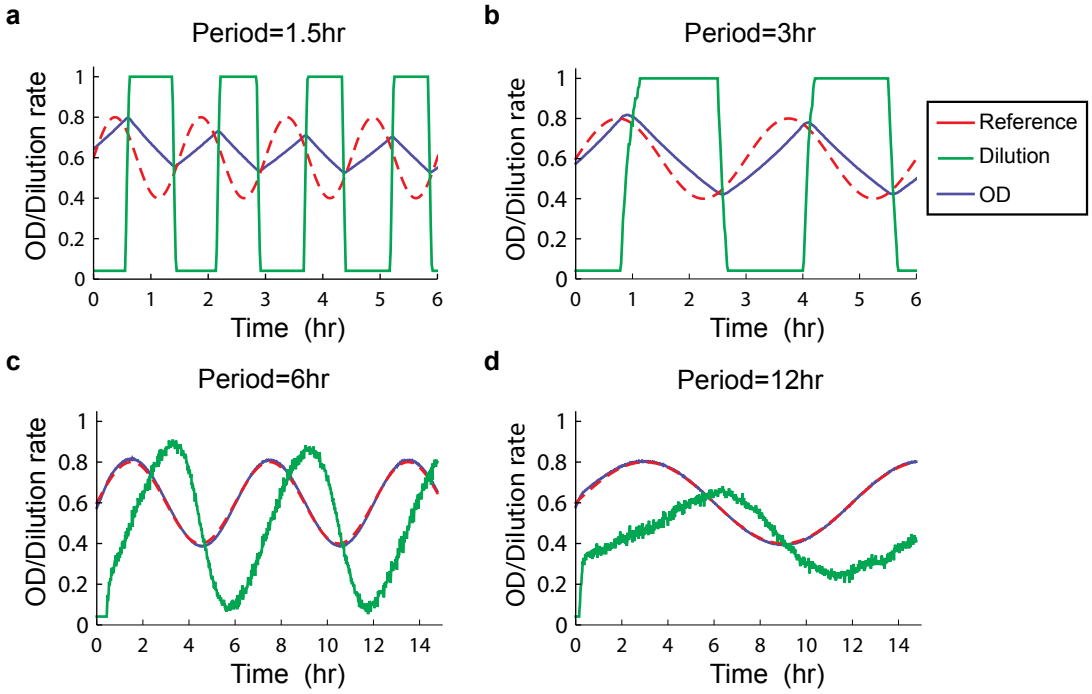

Figure 2.3: Experimental data collected from parallel experiments. *S. cerevisiae* was grown in synthetic complete media and made to track four sinusoidal reference trajectories (red). Measured OD values are shown in blue while the normalized dilution rate is shown in green. The maximum positive rate of change in OD is determined by the growth rate, while the maximum negative rate of change in OD is determined by the device's maximum dilution rate.

ber of each family of AFB and EYFP-Aux/IAA proteins, strong YFP fluorescence can be measured through flow cytometery. With the addition of auxin, the EYFP-Aux/IAA fusion protein is degraded and within two hours only background fluorescence is detectable. The exact degradation rates were characterized and shown to be dependent on the combination of AFBs and Aux/IAAs.

In previous work, each member of a combinatorial AFB Aux/IAA library was grown in synthetic complete medium (SC) under batch conditions at 30 °C in a shaker incubator over night. The following day, the cultures were diluted and allowed to reenter exponential growth phase before induction at a cell count roughly equivalent to OD 0.4 in the Flexostat.

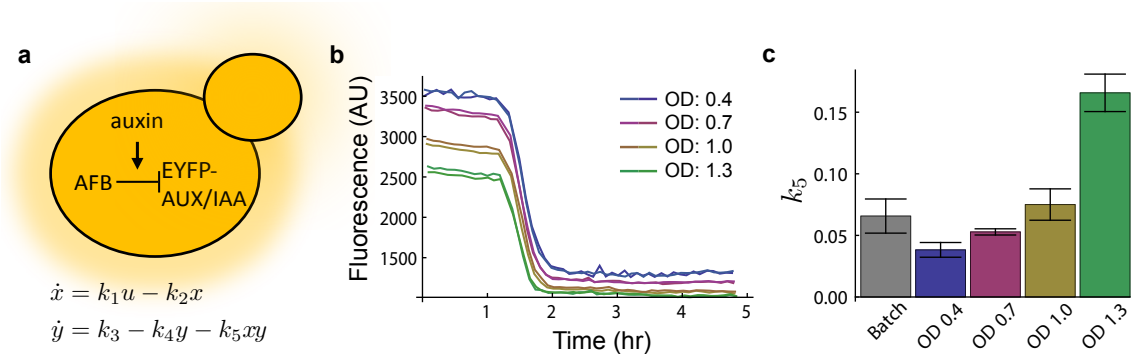

Figure 2.4: (a)Top: In the presence of auxin, AFB degrades the fusion protein EYFP-AUX/IAA. Bottom: A model from previous work [1] of the network shown above. State x represents auxin bound to AFB with input u being the auxin concentration, parameter k_1 the association rate of auxin and AFB, and k_2 the natural degradation rate of AFB. State y represents the concentration of EYFP-AUX/IAA where k_3 is the production rate, k_4 is the natural degradation rate and k_5 is the degradation rate in the presence of auxin bound to AFB. (b) YKL73 characterized in a turbidostat at four different ODs. At t=1.25 hours auxin was added to the culture chamber and media source to reach a concentration of 10 µM and the response was measured by sampling effluent and reading mean fluorescence in a flow cytometer at a period of roughly six minutes. The cytometery data was gated to only include singlet (non-budding) yeast in a healthy size range. An untreated time course is available as supporting information figure B.9 and shows no singnifigant change in fluorescence. (c) Model parameter k_5 was fit to the data collected in b (See Havens et al. [1] supplemental for detaled methods) and compared to previous work(grey) [1].

Over the course of three or more hours, cells were sampled from batch and fluorescence was measured in a flow cytometer. These data were then fit to an ODE model (Figure 2.4a) where the parameter k_5 represents the degradation rate of EYFP-Aux/IAA in the presence of auxin bound to AFB.

We hypothesize that culture density has an effect on degradation rates either directly or indirectly through changes in nutrients, signaling molecules, and waste products that correspond with cell density in a given media. To test our hypothesis we selected a strain YKL73 from previous work that co-expresses AFB2 and EYFP-Aux/IAA6. YKL73 was grown in SC in our turbidostat inside of a 30 °C incubator at four different ODs: 0.4, 0.7, 1.0, and 1.3 in duplicate. Although we chose OD ranging from 0.4 to 1.3, we did not observe a significant difference in growth rate between cultures, which is typical for growth at non-limiting nutrient concentrations. To measure fluorescence in each chamber, 200 µL

of effluent was sampled every six minutes and measured in the same flow cytometer as previous work(Figure 2.4b). After fitting the new degradation curves we found k_5 to vary from 0.036±0.006, an average degrader, to 0.171±0.015 (Figure2.4c and Table B.2), which is 35% faster than the fastest (AFB,Aux/IAA) pair previously reported [1] from batch data.

Another apparent feature of the data are the initial AUX/IAA levels (quantity k_3/k_4 in the model). The initial expression levels also show an inverse relationship between OD and untreated expression of AUX/IAA. Figures 2.4c, B.10 and B.11 illustrate the relationship between OD, initial expression, and degradation rates though the exact cause of the relationships is unknown.

In continuous culture, steady state levels of waste products and other exportable chemicals are proportional to cell density. Through the use of cytometer gating we controlled for cell size and morphology (singlets vs. budding cells). This leads us to hypothesize that either the rate k_5 and the ratio k_3/k_4 are highly sensitive to differences in growth rate (within the error margin of our measurements), or that the cells' internal state was affected by the density dependent effects in environment. Since k_5 is modeled as a constant, the density dependent effects on fits, which could not have been measured in batch, highlight the utility of continuous culture in model validation and the need, in this case, for a higher order model to explain the data when density cannot be controlled. Further study is required to determine the exact nature and source of the physiological changes that influence expression and degradation rates.

A fluorescence detecting turbidostat

A key capability in synthetic and systems biology is the ability to read fluorescent reporters. In the previous section we used a flow cytometer, which resulted in individual cell data but was labor intensive. An alternative method to collecting cytometry data is to obtain bulk fluorescence *in situ*, which can be collected without user intervention.

We modified the original chamber design to include a blue excitation light source at a right angle to the absorbance photo sensor (Figure 2.5a). The new design multiplexes the original light sensor in time to serve the dual purpose of measuring absorbance and

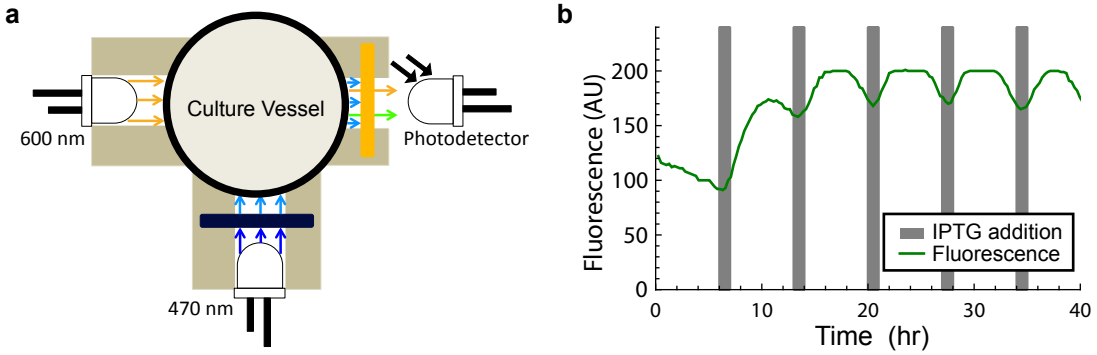

Figure 2.5: (a) A diagram representing the layout of the modified fluorostat culture chamber. The light sensor is time divison multiplexed between light from the absorbance source (600 nm) and fluorescence excited by the excitation source (470 nm). A filter set ensures that only light generated by fluorescence is detected. (b) An IPTG inducible GFP expressing strain of *E. coli* was grown at OD 0.6 in alternating M9 media with (grey area) and without IPTG.

fluorescence. For OD measurements, the chamber works as described in earlier sections. When fluorescence measurements are made, the 600nm LED is turned off and the 470nm LED excitation source is turned on. To prevent bleed over from the excitation source into the emissions wavelengths we added a band pass optical filter (See methods and supporting information section B.4). Similarly, to prevent the excitation source from being detected by the photo sensor a long-pass optical filter was added.

To test the fluorescence detection capability of our fluorescence detecting turbidostat (or Fluorostat for short), we measured a range of fluorescent cultures. Wild type *E. coli* (BL21) and BL21 containing a high expression super folder green fluorescent protein (sfGFP) plasmid were cultured for use in quantification. The cultures were then mixed at various ratios and measured in the Fluorostat, which showed a linear relationship between mix ratio and measured fluorescence (Supporting Figure B.13).

Next we tested the Fluorostat under more experimentally realistic conditions. We cultured an IPTG inducible sfGFP expressing strain of *E. coli* in the Fluorostat. At periods of 1 h and 6 h media containing 1 mM and 0 mM IPTG respectively were alternated and the resulting fluorescence signal was measured (Figure 2.5b). The results of this experiment

demonstrate the ability of an LED based fluorimeter to read sfGFP reported outputs during the course of a turbidostat experiment. These results also highlight the adaptability of our design to work with evolving experimental needs.

While linear within its dynamic range and capable of measuring changes in expression levels, we discovered that only cultures bright enough to be visibly fluorescent under blue light transillumination were capable of being detected. The YFP expressing strain of yeast measured using cytometry in the previous section was too dimly fluorescent to measure in the Fluorostat. While its low sensitivity precludes the use of the Fluorostat in some experiments, we believe that through further refinement, the use of a more sensitive fluorometer, or an automatic cytometer sampling system all experiments requiring fluorescence measurement should be possible without manual sampling.

Conclusion

With the advent of 3D printing and other inexpensive custom fabrication processes, laboratories are now more capable of building their own equipment from open source designs than ever before. These community driven designs have the benefit of open design elements that allow labs to customize software and hardware for their own unique experiments rather than using designs optimized for industrial purposes. We presented a new 3D printable and customizable turbidostat for the next generation of "3D printed labs".

To demonstrate its utility, we have shown an example system with previously thought to be constant parameters that turned out to be dependent on cell density. We also demonstrated that our design can be adapted to accommodate fluorescence measurement, enabling the automatic collection of reporter expression data within the device.

Methods

All data fitting methods, yeast methods, strains, media, and flow cytometery are as in previous work [1], unless otherwise stated below.

Yeast Methods

Diploid *S. cerevisiae* strain YKL73 was obtained from previous work [1] and expresses AFB2 and IAA6 with EYFP fused to its N-terminus. All yeast cultures were grown at 30 °C in Synthetic Complete medium according to standard protocols. Batch cultures were grown from colonies in 15 mL tubes in a shaker incubator and used to inoculate turbidostat cultures. Auxin was dosed from a stock solution of 100 mM auxin in 95% ethanol to a working concentration of 10 µM into each turbidostat chamber while simultaneously dosing the media reservoir.

Fabrication

Complete construction and assembly instructions, design files (including 3D CAD and circuit boards), and a full bill of materials can be found on our website `http://klavinslab.org`. All ABS plastic parts were 3D printed with OEM natural colored filament on the UP! 3D printer from `http://www.pp3dp.com/`, which can be purchased for $1500 USD.

Delrin parts were laser cut from 5mm delrin sheet by `https://www.ponoko.com/`.

Circuit boards were manufactured by `http://www.seeedstudio.com/` and assembled by hand in the laboratory. Surface-mount soldering was done on a standard laboratory hotplate using CHIPQUIK Sn96.5Ag3.0Cu0.5 solder paste at a temperature of 230 C and through hole was done by hand using a Weller W60p soldering iron.

Fluorescence Detection

Fluorescence characterization was done with *E. coli* strain BL21 transformed with a plasmid containing the pLac promotor driving sfGFP. All growth of *E. coli* in the turbidostat was done in M9-1% glucose at an OD_{600} 2 cm of 0.6 and a temperature of 37 °C. Batch growth was done in M9-1% glucose media at 37 °C in a baffled shaker flask to stationary phase and diluted to OD_{600} 1 cm 1.0 in M9 salts. For fluorescent strains a saturating level of 100 µM IPTG was used to induce sfGFP expression.

The following filter set and excitation source was used for fluorescence measurement: Thorlabs part number FGB25, Thorlabs part number FGL530, ledsupply.com part number

L1-0-B5TH30-1.

Flow Cytometry

200 µL or greater samples were collected over three minute sampling periods into 2 mL 96 deep well plates. The plates were then transferred to an Accuri C6 flow cytometer with CSampler attachment for immediate measurement. All settings and analysis were done as in previous work [1].

Chapter 3

BUILDING THE FLEXOSTAT

In the previous Chapter 2 we discussed the design, specifications, and characterization of the Flexostat. One crucial aspect of the Flexostat that has aided it's wide spread adoption is adoption is it's open source design that can be inexpensively built with a 3d printer and minimal specialty tools. In this chapter we give complete instructions on how to build the turbidostat. Up to date instructions can be found at `http://klavinslab.org/hardware`.

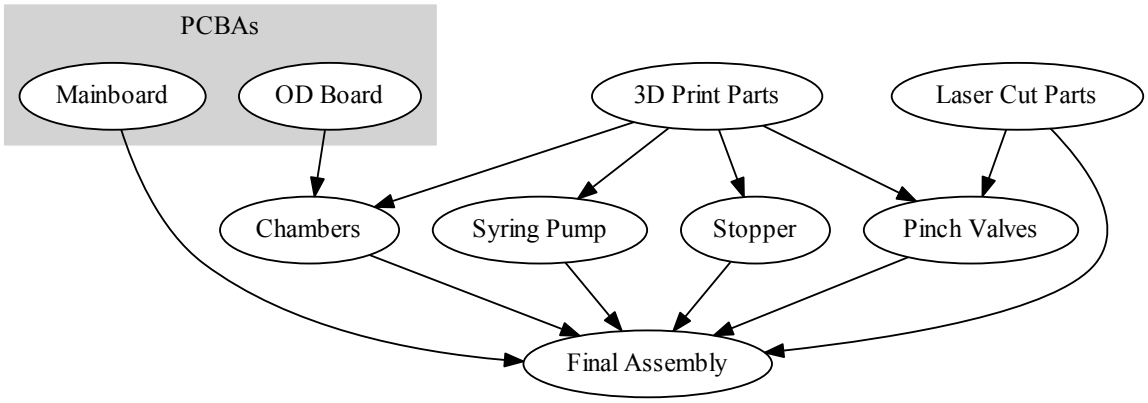

Figure 3.1: A graph of steps for each section of the Flexostat build. The top layer of the graph shows the basic components that are the output of machines or services. The middle layer of the graph shows the major assemblies of the Flexostat. The bottom layer of the graph show the final assembly, which composes assemblies from all previous steps.

Fig 3.1 depicts the assembly order and dependencies for the Flexostat. The Flexostat design is dependent on commodity parts that are readily available from supplies such as Digikey, Amazon.com, and VWR as well as customized mechanical and electrical components that can be built using inexpensive rapid prototyping technologies such as fused deposition modeling (FDM, a.k.a. fused filament fabrication, FFF) 3D printing and Laser

cutting. Commodity and fabricated parts are then assembled into modular assemblies, each of which may be modified or substituted with minimal impact on the design of connected assemblies. Finally, assemblies are mechanically and electrically connected into a complete device.

3.1 Printed Circuit Boards

Printed circuit boards (PCBs) and PCB assemblies (PCBAs) may be inexpensively produced through a variety of on-line and local vendors. We do not recommend making them in-house. At the time of this writing, the OD PCBA can be purchased from Seeed [sic] Stuido (`http://www.seeedstudio.com/service/`) with all components soldered except the light sensors, which are not part of the Seeed Open Parts Library (OPL). These instructions assume PCBAs for the OD boards were purchased from Seeed Studio. If unassembled PCBs were purchased then the assembly photos may also be used as a reference for component placement and orientation, and the mainboard instructions and be used as a reference for surface mount soldering technique. A complete bill of materials (BOM) is available in appendix [[xxxx]] and on the website [44].

3.2 Mainboard

To assemble the mainboard you'll need a soldering iron, temperature controlled hotplate, basic hand tools, and the components outlined in the digikey section of the BOM. Note that some photos may differ from the current version. For exact component placment for the Flexostat mainboard V2.0 please reference figure B.18 or the website [44].

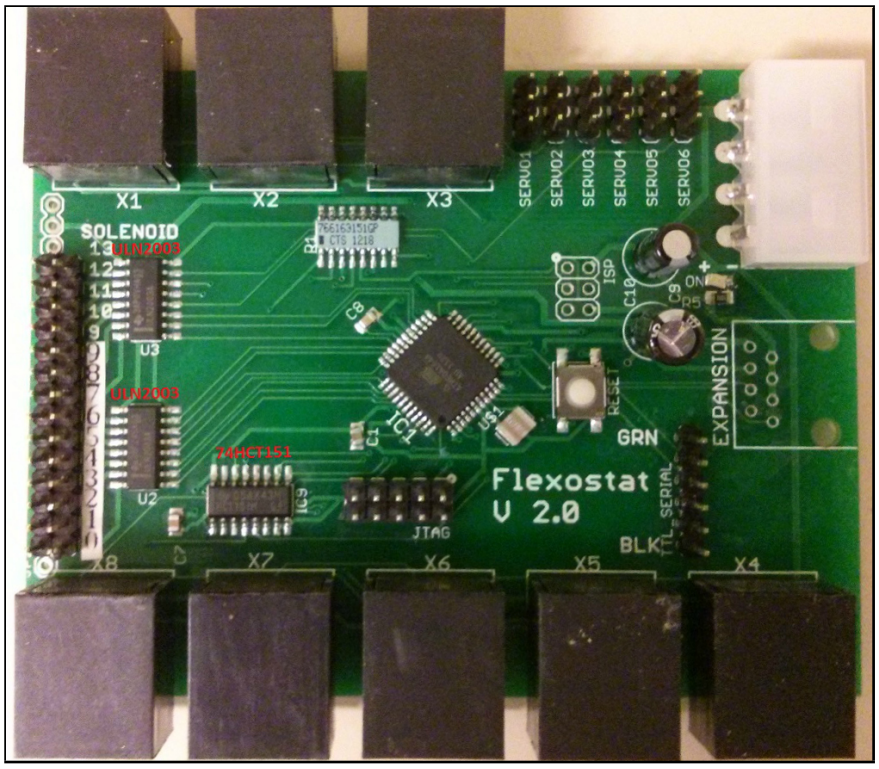

Figure 3.2: A complete assembled mainboard. Ambiguous components are labeled in red with part numbers.

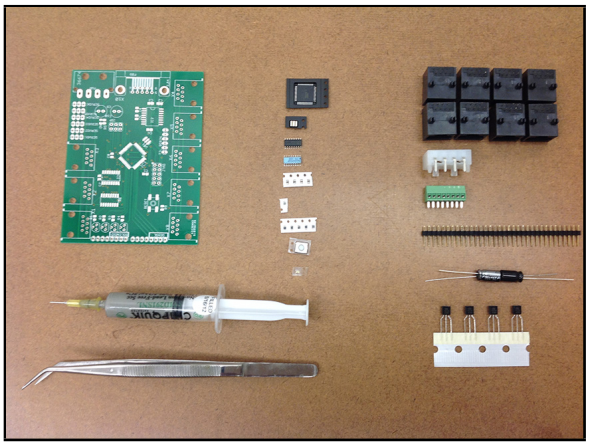

Step 2.1: **gather all components.**

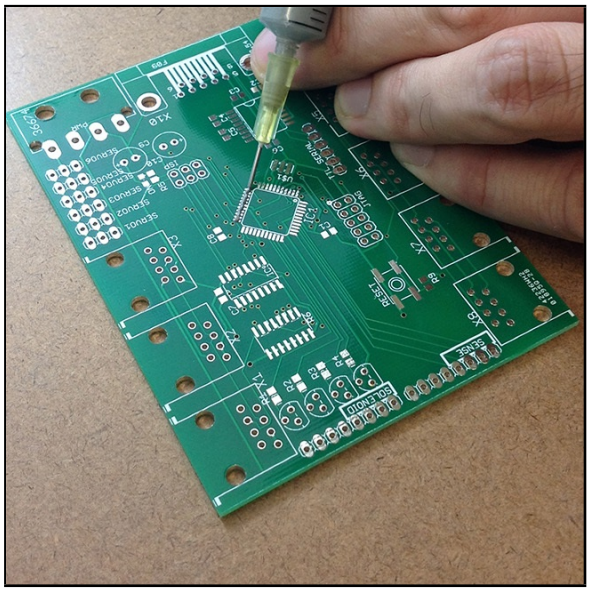

Step 2.2: **Apply solder paste using the syringe to the solder pads as shown.**

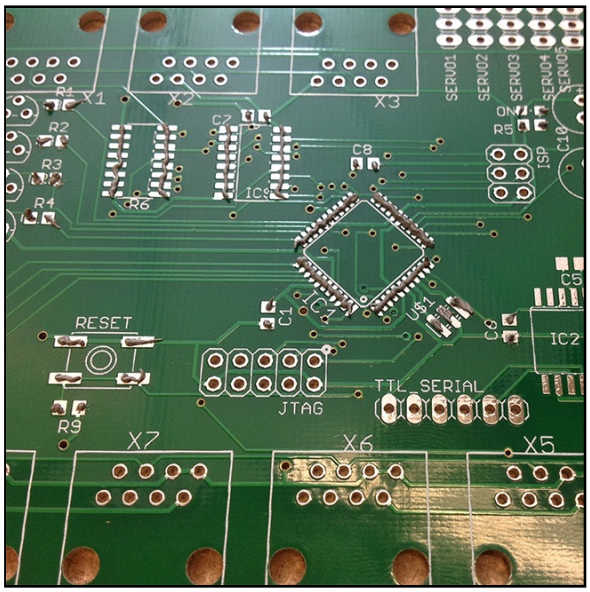

Step 2.3: **Repeat for all exposed pads.**

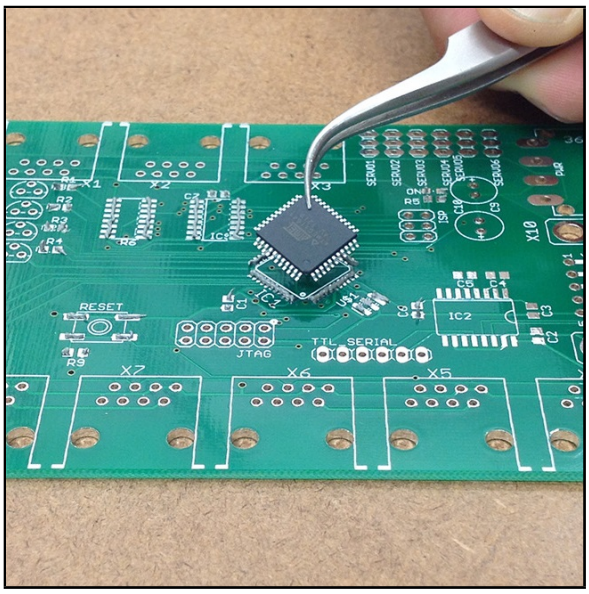

Step 2.4: **Place components minding correct orientation.**

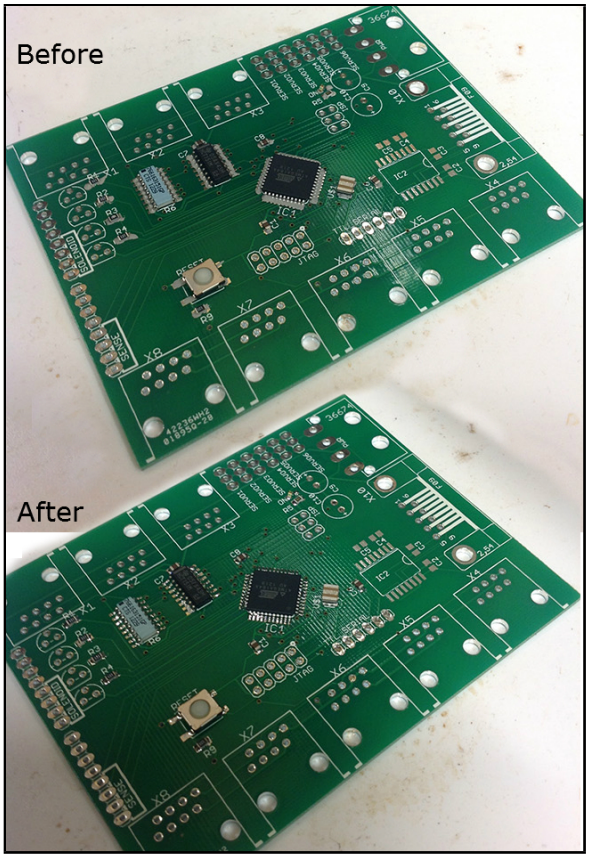

Step 2.5: **Solder the PCB with a temperature controlled hotplate.** Place the populated PCB on a reflow hotplate or standard laboratory hotplate Note that laboratory hotplates with stir functionality contain magnets that may effect placement of some components. Do not drag the soldered pcb across the face of the hotplate.. Set the hotplate to 230C. The parts may smoke, this is the solder flux burning off and completely normal. Once the PCB reaches the melting point of solder the paste should turn from gray to silver. At this point you may tap the PCB to allow capillary forces to center the parts. Once all solder has melted carefully remove the pcb and set it on a heat resistant surface to cool for 2-3 minutes.

Step 2.6: **Place the through hole components.** Place a through hole component. A piece of poster tack or lab tape will help the parts stay in place during soldering.

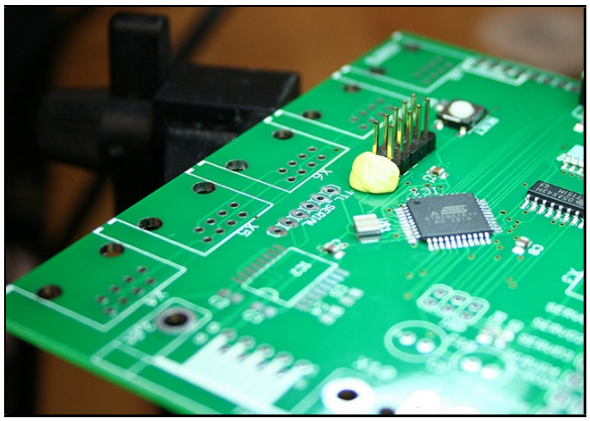

Step 2.7: **Solder the through hole components.** Solder the component you just placed. For instructions on through hole soldering see references [45, 46].

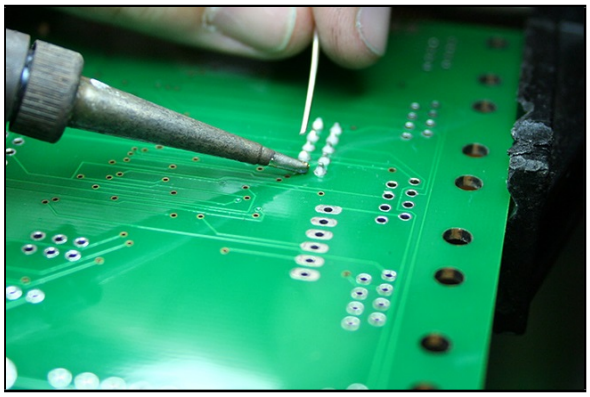

Step 2.8: **Trim excess length from through hole leads.** Any lead protruding further than a couple of millimeters should be trimmed just short of the solder joint.

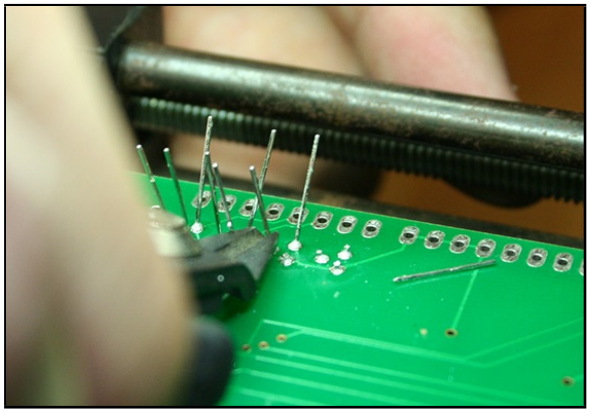

3.3 OD Board

To assemble the OD board you'll need the PCBA produced by Seeed Studios and two light sensors per board. A complete Flexostat consists of eight chambers and therefore eight OD Boards should be assembled.

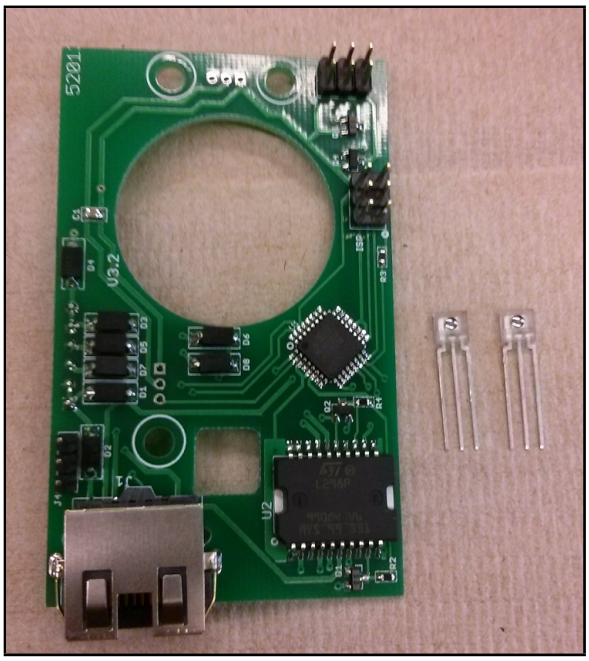

Step 3.1: **Collect a circuit board and two light sensors.**

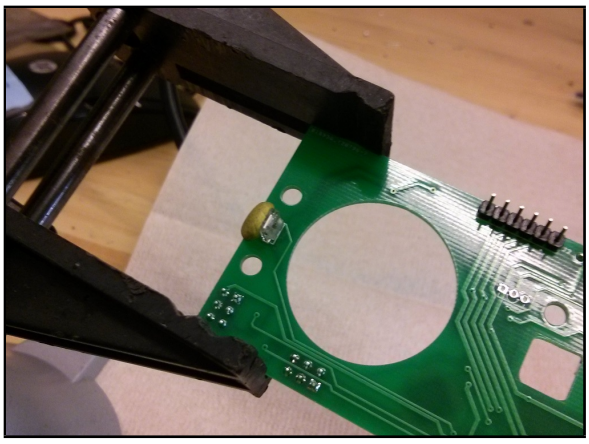

Step 3.2: **Solder the first light sensor in place.** Insert the first light sensor so the dome faces the center of the PCB. Make sure that you insert the light sensor on the back side of the circuit board as photographed. A small amount of tape or poster tack will help hold the part in place as you solder. Alternatively, a 3d printed holder is available to help hold and align the parts. Once the part is held in place, turn the board over and solder the component into place.

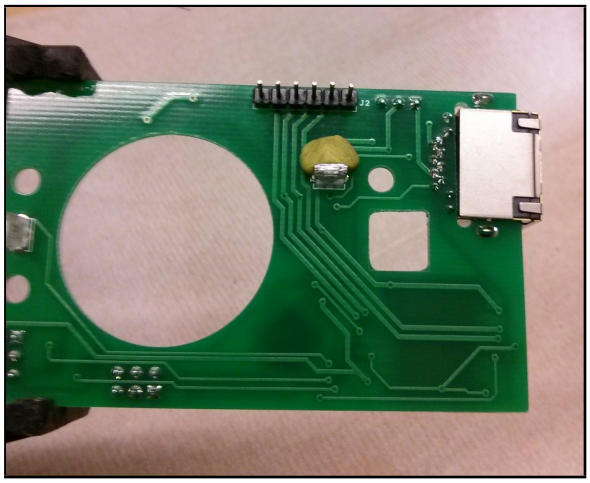

Step 3.3: **Repeat for the second light sensor.** Again, this sensor should be on the back side of the PCB with the dome facing inward.

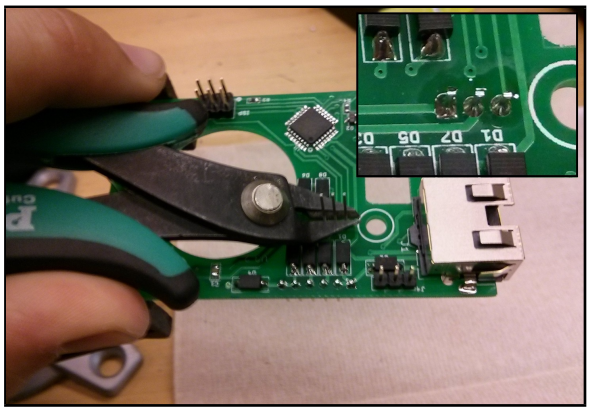

Step 3.4: **Trim the leads.** Trim the light sensor leads to just above the solder join. This prevents accidental shorting.

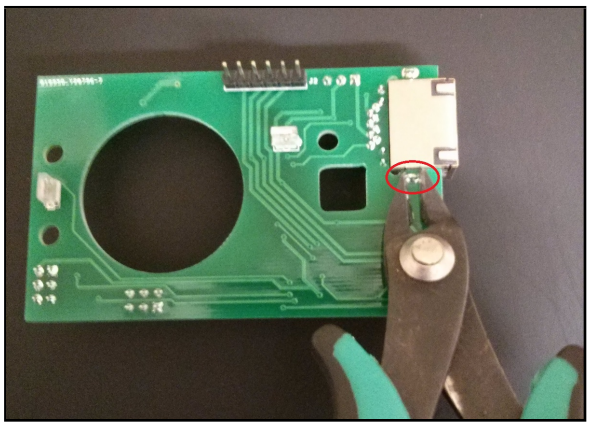

Step 3.5: **Trim inside tab off of the RJ45 jack.** Trim the inside tab off of the RJ45 jack. This prevents mechanical interference between the laser and the circuit board. Try and trim the solder tab as close to the PCB as possible. Don't worry about damaging the PCB as there are no traces near by and the tab you are cutting has no electrical function.

3.4 Fixing Surface Mount Shorts

Occasionally two pins will bridge during the surface mount soldering step. To remedy this excess solder may be removed with copper braid (a.k.a. solder wick). If possible use wick that comes precoated in flux.

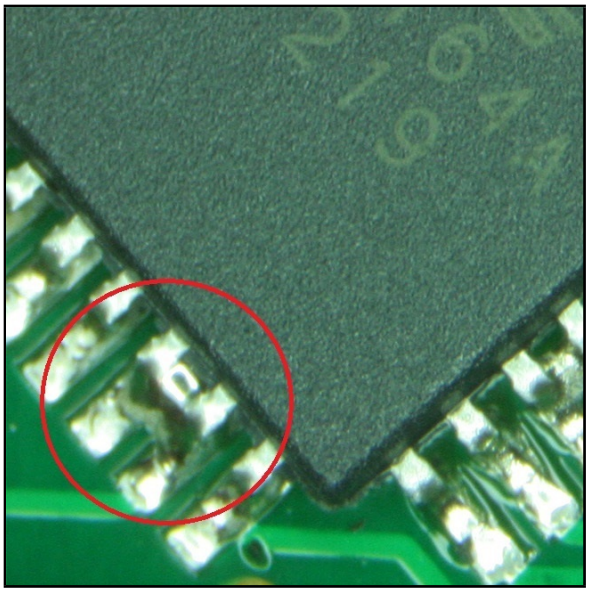

Step 4.1: **Identify solder bridges.** After the surface mount soldering step it's a good idea to use an inspection scope or magnifier to identify any bridged solder pads. Often times reheating the join with a tinned soldering iron tip is sufficient to correct the bridge. If it is not move to the next step.

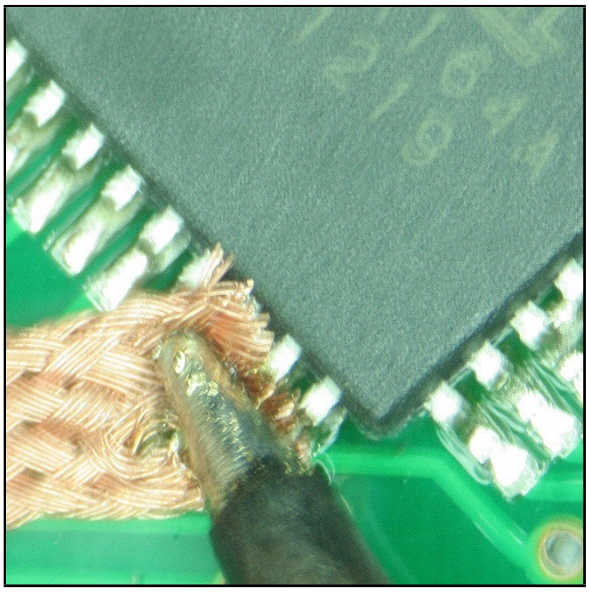

Step 4.2: **Apply wick and heat.** Place a clean section of wick over the bridged pads. Heat the wick from above with soldering iron. You should see the copper turning silver indicating that it is wicking melted solder. Be careful not to remove too much solder.

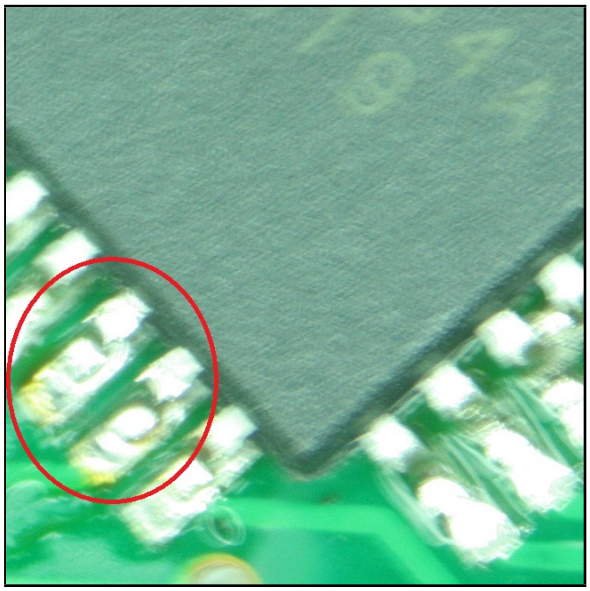

Step 4.3: **Remove wick and heat together.** At the same time remove the wick and soldering iron. Inspect the joint. It may be necessary to add flux and repeat, or add solder back to the joints.

3.5 Chamber Assembly

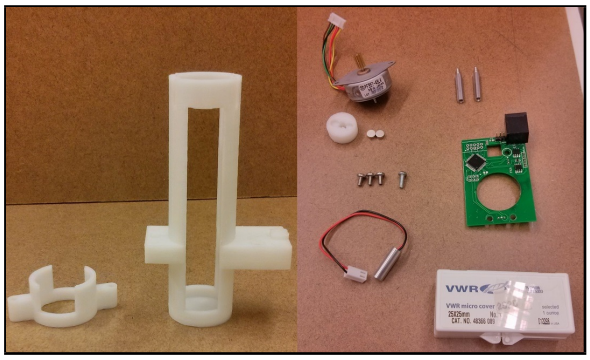

Step 5.1: **Gather all parts for the chamber assembly.** The 3D printed parts are Chamber, Motor mount, and Stir magnet holder. You'll also need the stir motor, stir magnets, narrow aluminum standoffs, 3 6-32x1/4" machine screws, 1x 6-32x3/8" machine screw or a 6-32 grub screw, the assembled OD board, 650 nm laser, and a microscope coverslip.

Step 5.2: **Gather necessary tools.** You will need actone, a 6-32 tap, #2 screwdriver, tweezers, and a paint brush.

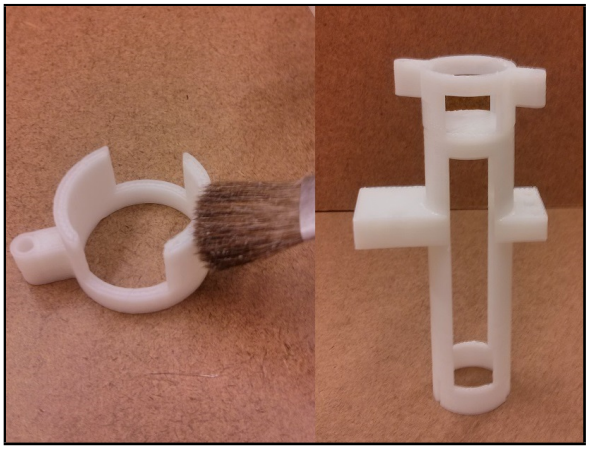

Step 5.3: **Using the acetone "glue" the motor mount to the 3D printed chamber.** Using the paint brush apply acetone to the mating faces of the motor mount and 3D printed chamber. Immediately press the parts together. They should become permanently bonded after several minutes.

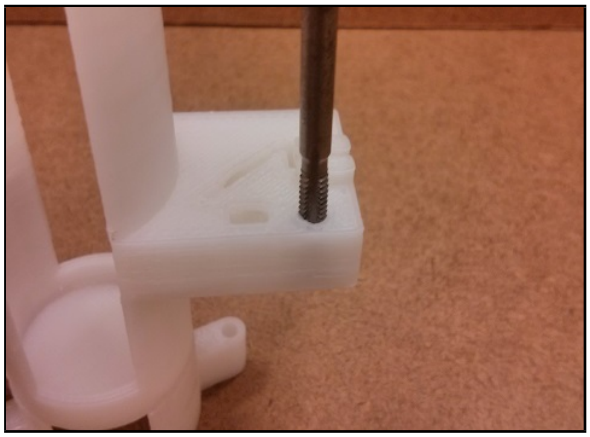

Step 5.4: **Tap all holes in the 3d printed chamber and motor mount.** Using the 6-32 tap, tap threads into the two motor mount holes from the bottom and the three PCB mount holes from the top.

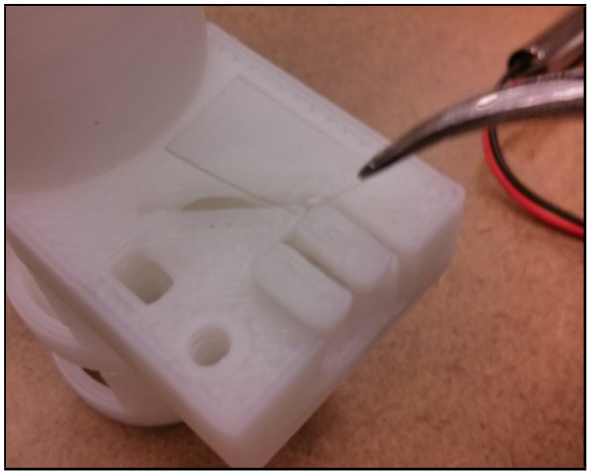

Step 5.5: **insert the cover slip into the slot.** Depending on the cover slip it may be necessary to cut it down to size.

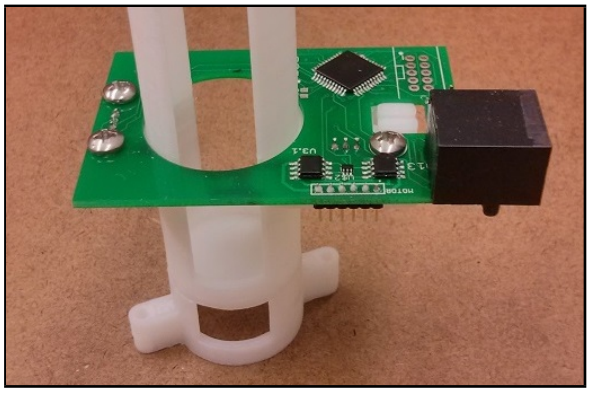

Step 5.6: **Attach the PCB.** Using the three 6-32 screws attach the PCB to the chamber a shown. Do not over tighten the screws.

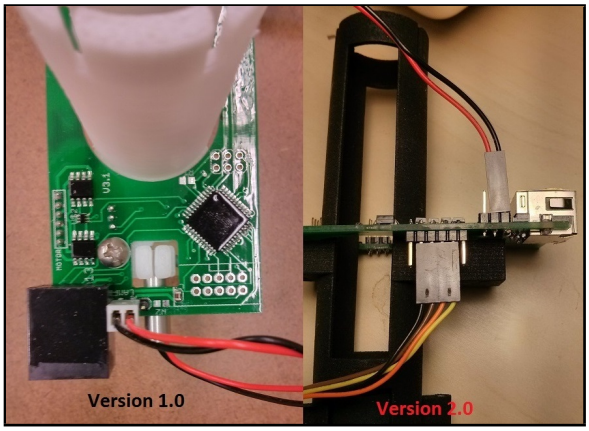

Step 5.7: **Attach the the laser.** Insert the laser into the 7mm hole in the front of the chamber. On some revisions a 3/8" long or grub screw may be necessary to retain the laser. Once mounted connect the laser to the PCB noting the position and orientation.

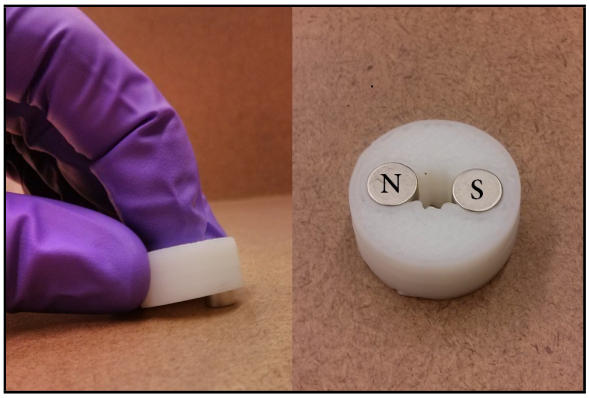

Step 5.8: **Insert the magnets into the magnet hole.** Insert the laser into the 7mm hole in the front of the chamber. On some revisions a 3/8" long or grub screw may be necessary to retain the laser. Once mounted connect the laser to the PCB noting the position and orientation.

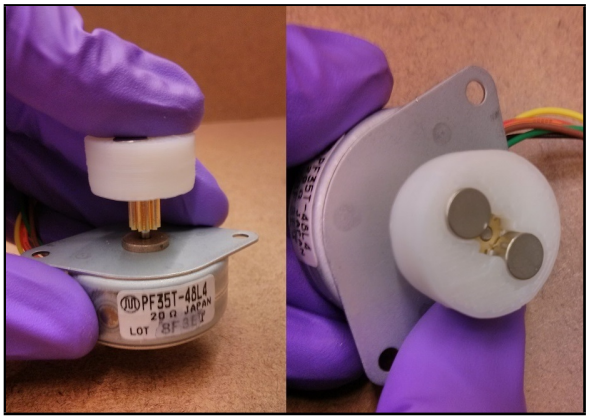

Step 5.9: **Attach the magnet holder to the motor.** Line up the gear teeth with the cutout in the bottom side of the motor mount. Press the magnet holder firmly onto the motor gear until the gear touches the bottom side of the magnets. Be sure to apply forces along the axis of motor shaft and only apply force to the magnet holder, gear, and motor shaft.
Note: Only apply force to the motor shaft, not the motor body. Doing so may damage the motor.

Step 5.10: **Attach the motor to the chamber body.** Using the two 1" standoffs, screw the motor to the chamber. Make sure the wires exit the laser side of the motor. Next attach the 6pin motor header onto the OD board.
Note: The 6pin header is not polarized and orientation does not matter. Changing the connector orientation only effects the direction the stir bar spins.
Note: It is easy to get this connector offset by one position. If the stir motor does not spin check this first.

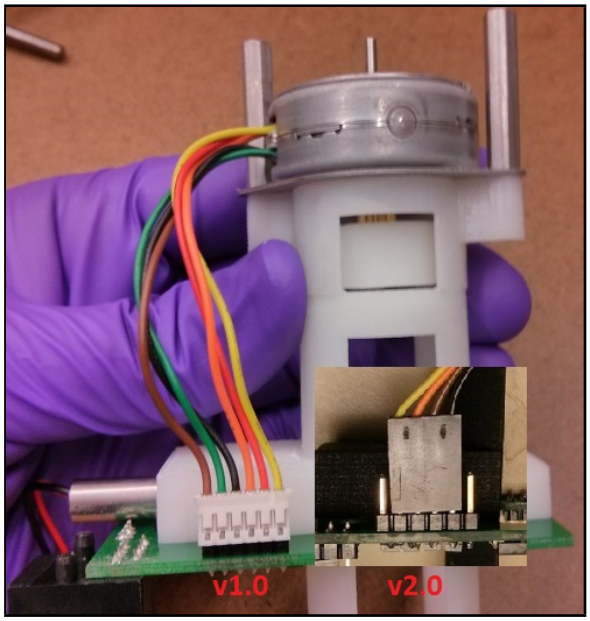

Step 5.11: **Mount the chamber.** Using the two standoffs as attachment points mount the chamber onto whatever you're using as a base.
We recommend using a piece of 3"-4" wide 18" long u-channel aluminum. Aluminum is easy to cut and machine and can be drilled with standard drill bits and a hand drill. Choosing u-channel will allow for the screw heads to protrude and keep the chambers up off the surface they are set on, which can help protect them from spilled media.

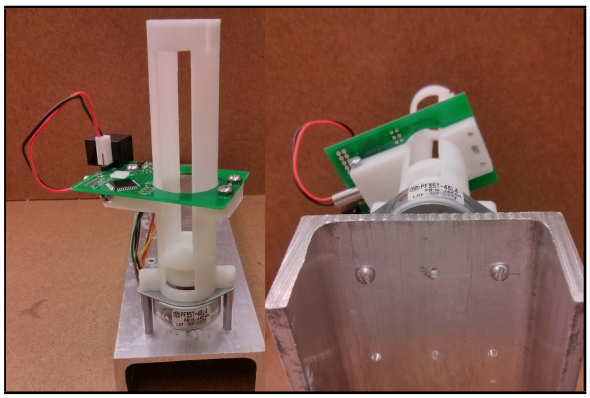

3.6 Stopper

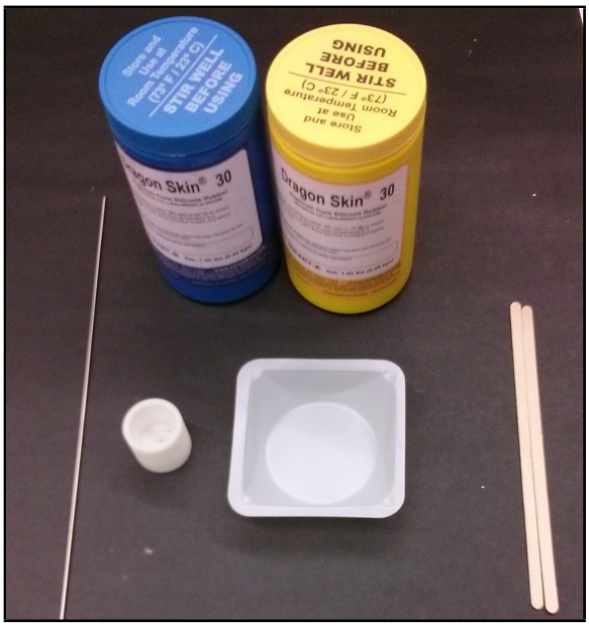

Step 6.1: **Gather components for stopper molding.** Gather two part silicone (shore 30a or less is recommended), approximately 20 cm per stopper of 2mm OD stainless tube, 3D printed stopper mold, a weigh boat and stir sticks.

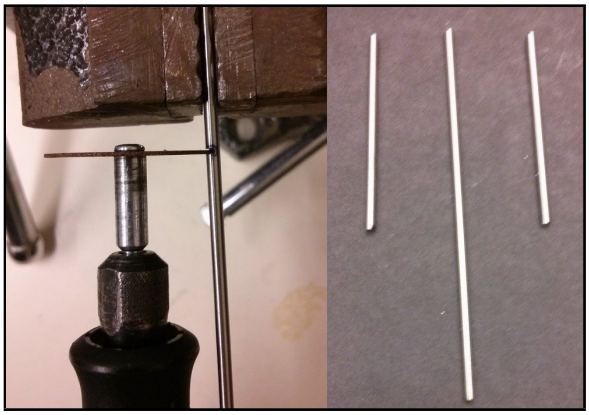

Step 6.2: **Cut the stainless steel tubing to length.** Using an abrasive cutoff wheel (A rotary tool or even 4.5 in grinder works well), cut a length of 9 cm and two lengths of 5 cm SS tube.

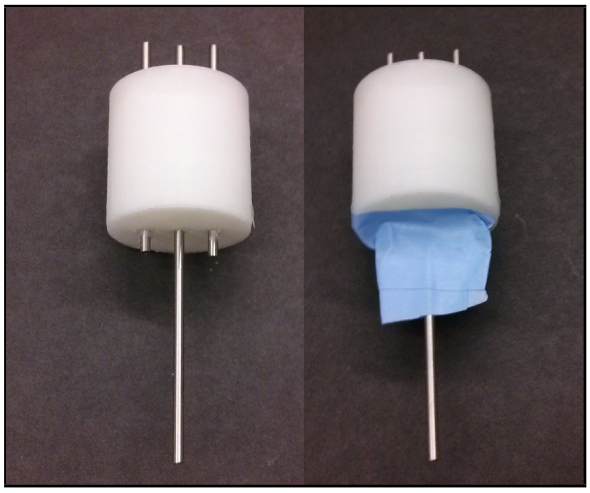

Step 6.3: **Insert SS tube into stopper mold.** Insert tube through holes in the mold with the long tube in the center. Adjust tubes so each tube protrudes from the top of the mold by about 1cm. Once adjusted, tape tubes together and to the bottom of the mold.

Step 6.4: **Mix and pour silicone rubber into stoppers.** Mix the rubber following the directions on the bottle, degassing if desired. Pour the mixture into the molds and leave to cure. Curing can be accelerated in a 65 °C oven. After the silicone has cured carefully remove the stopper from the mold and reuse if needed.

3.7 Syringe Pump

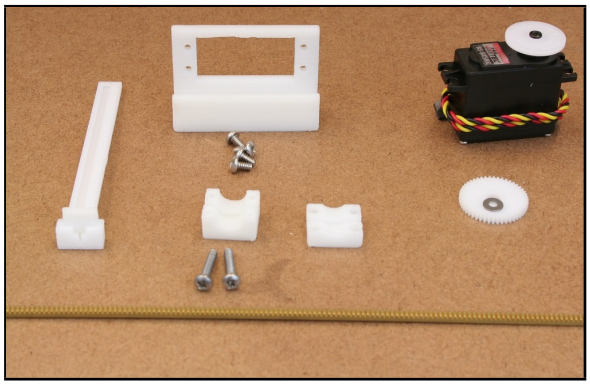

Step 7.1: **Gather parts.** Gather the 3d printed pump parts, HS-645MG servo motor, brass gear rack, pinion gear, and 6-32 screws.

Step 7.2: **Gather tools.** Tools you'll need are a 6-32 tap, #0 and #2 Phillips screwdrivers, a file or rough grit sand paper, and a hack saw or abrasive cutting wheel.

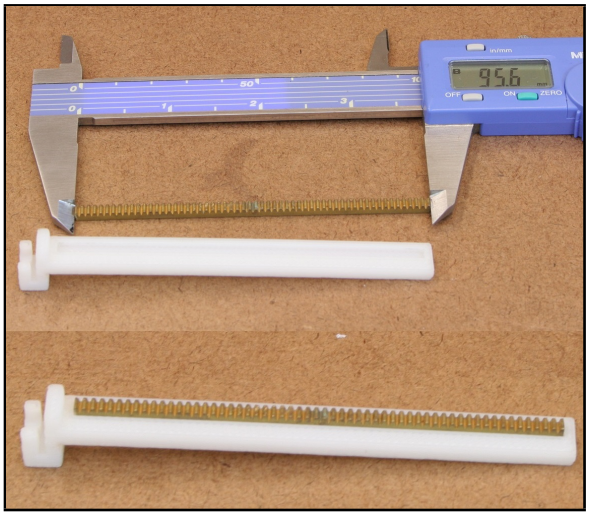

Step 7.3: **Assemble slide.** Cut gear rack to the length of recessed area in 3d printed pusher. Using the file clean up any rough edges. the gear rack should friction fit into the pusher.

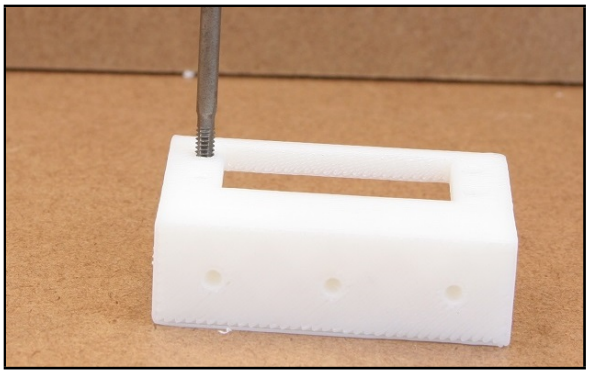

Step 7.4: **Thread 3d printed parts.** Using the 6-32 tap cut threads into all holes in the 3d printed pump parts. There should be 11 in all.

Step 7.5: **Prepare the servo motor.** Manually turn the survo motor counter clockwise until it stops. Then clip the vertical tabs near the mounting holes on either side. If using the most recent designs you may now also attach the servo mounted gear.

Step 7.6: **Place the pump slide in the pump body.** Make sure that it's placed 5mm from the end as it's important for indexing.

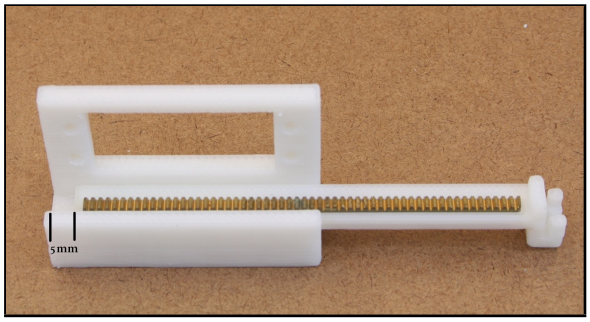

Step 7.7: **Prepare the servo motor.** Manually turn the survo motor counter clockwise until it stops. Then clip the vertical tabs near the mounting holes on either side. If using the most recent designs you may now also attach the servo mounted gear.

Step 7.8: **Mount the servo motor with gear.** Mount the servo to the pump body. Make sure not to disturb the location of the slide or the rotational orientation of the motor. This will ensure proper indexing.

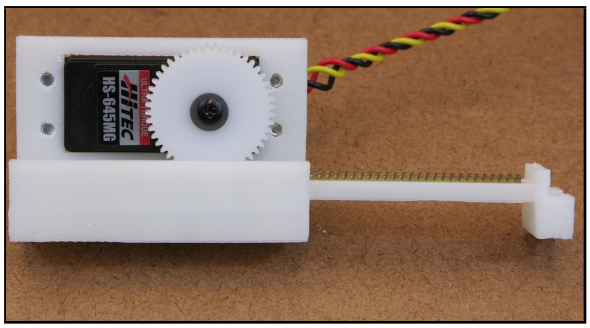

Step 7.9: **Mount the pump.** Mount to the pump to it's final mounting surface. be sure to observe the spacing shown.

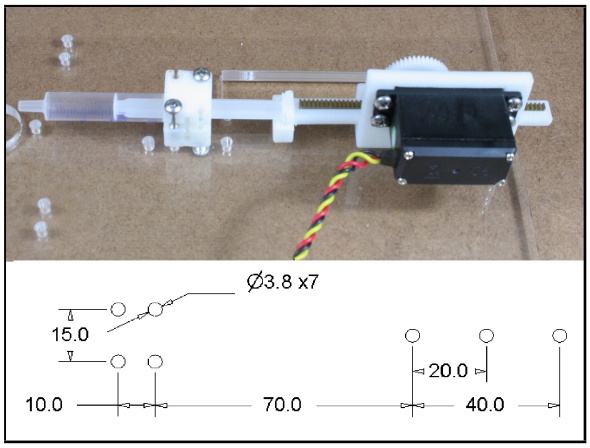

3.8 Syringe Pump

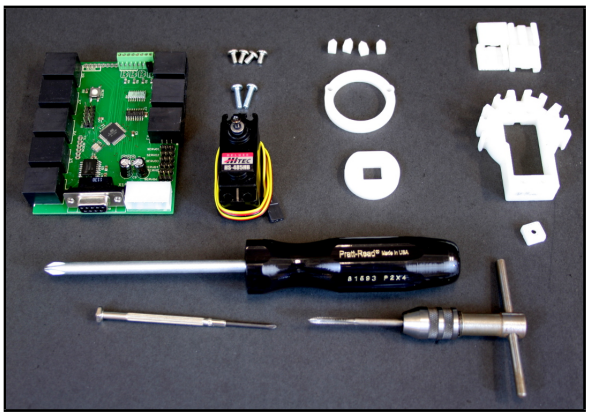

Step 8.1: **Collect parts for the pinch valve.** Collect the 3D printed parts, laser cut parts, HS-485HB servo motor, screws, main board, #0 and #2 screwdriver, and 6-32 tap.

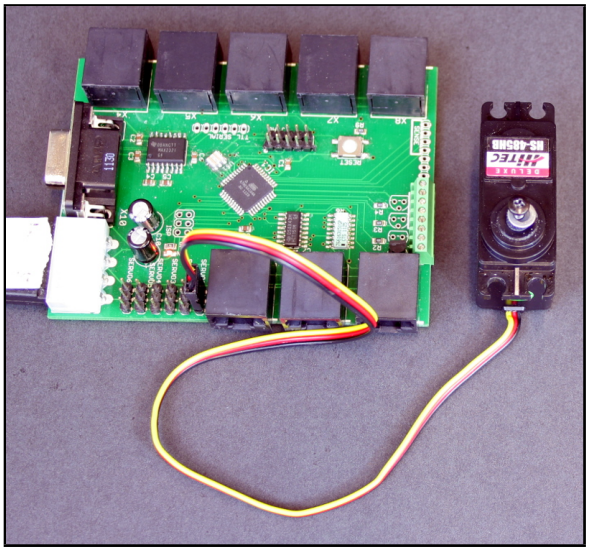

Step 8.2: **Center the servo motor.** Power the main board (make sure it's been programmed), and attach the servo as shown. The servo should move to it's centered location.

Step 8.3: **Press fit the 3d printed adapter onto the servo motor. Make sure that the adapter is aligned correctly, parallel with the sides of the motor.**

Step 8.4: **Tap the holes in the pinch valve body** Holes marked blue should be tapped from the front (as shown). Holes marked in red should be tapped from the back.

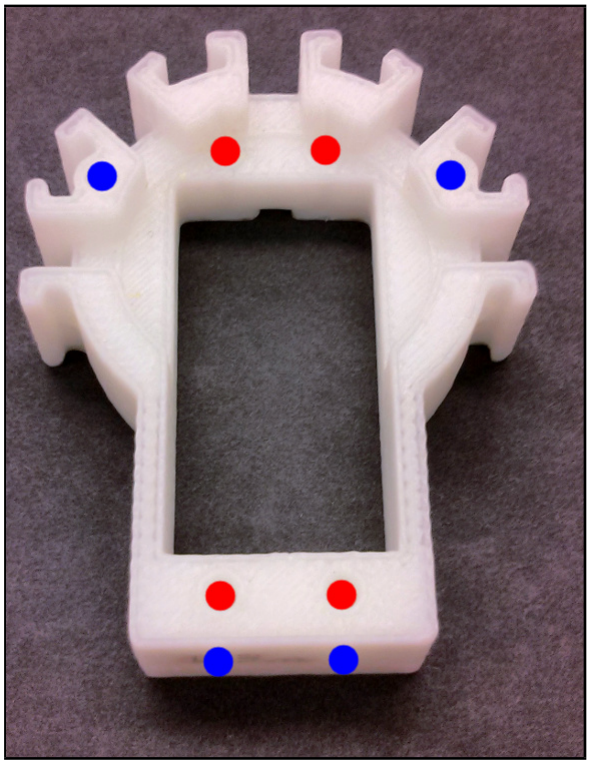

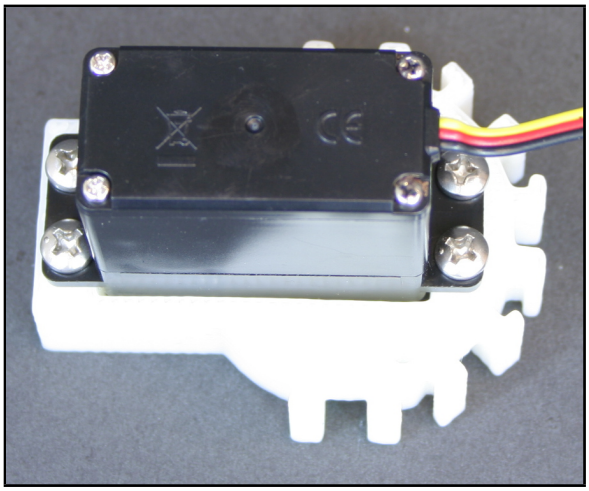

Step 8.5: **Mount the servo to the pinch valve body.** Turn the body face down. Using the four 1/4" screws, attach the servo motor to the pinchvalve body from the back side (as pictured from the previous step.

Step 8.6: **Attach the cam to the servomotor.** Turn the assembly back over and press fit the cam so that the flat side is facing up.

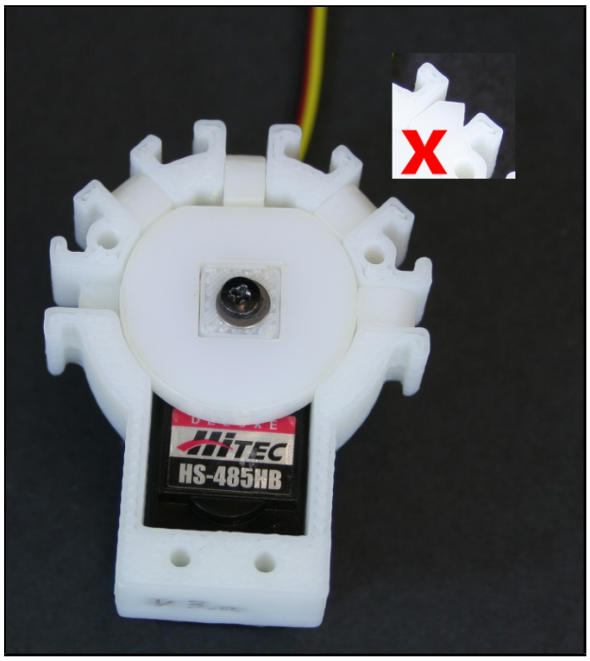

Step 8.7: **Insert four pinchers.** Insert the four delrin pinchers into the right most four openings, leaving the left most opening open. Make sure the pinching surface is oriented so that it spans the entire opening (see photo).
Note: from here until the last step, do not tip the assembly or the pinchers may fall out.

Step 8.8: **Attach the front cover.** Attach the delrin front cover using the two 1/2" screws.

Step 8.9: **Attach the four retention clips.**

Chapter 4

A BIOFILM FREE *ESCHERICHIA COLI*

Continuous culture provides constant culture conditions enabling better characterization of synthetic circuits as well as constant selective pressures for directed evolution. When characterizing synthetic circuits over generational timescales (tens of minutes to hours), cellular metabolism impacts batch culture conditions, which can act as a disturbance to synthetic circuits and change selective pressures in directed evolutions. In continuous culture, substrate concentrations and metabolic byproducts reach a steady state eliminating the drawbacks of batch culture. However, continuous culture selects strongly for phenotypes that are resistant to washout, such as flocculent yeast or adherent biofilms in *E. coli* [47]. Lab strains of yeast that are resistant to flocculation [48] are readily available, however a strain of *E. coli* that does not form biofilms in continuous culture has not yet been reported. Here, we have developed a five gene/operon *E. coli* knockout strain BF019 that is resistant to biofilm formation in continuous culture. We show that wild type *E. coli* can form disruptive biofilms in as little as 48 hours, while our novel strain remains biofilm free for at least two weeks, after which we ended the experiment. Strain BF019 and our previously reported [49] open-source turbidostat design [50] form a platform enabling characterization of long-term dynamics as well as directed evolution of better substrate utilizers and more tolerant strains required for consolidated bioprocessing.

4.1 Results

Candidate Genes for deletion

A bacterial biofilm is a community of adherent bacteria that live on a surface. In continuous culture, the adherent properties biofilms of protect cells from washout. Since only planktonic cells are washed out, there is a strong selective advantage given to those cells living in biofilms, which causes biofilms to become enriched. Biofilms can therefore be counter

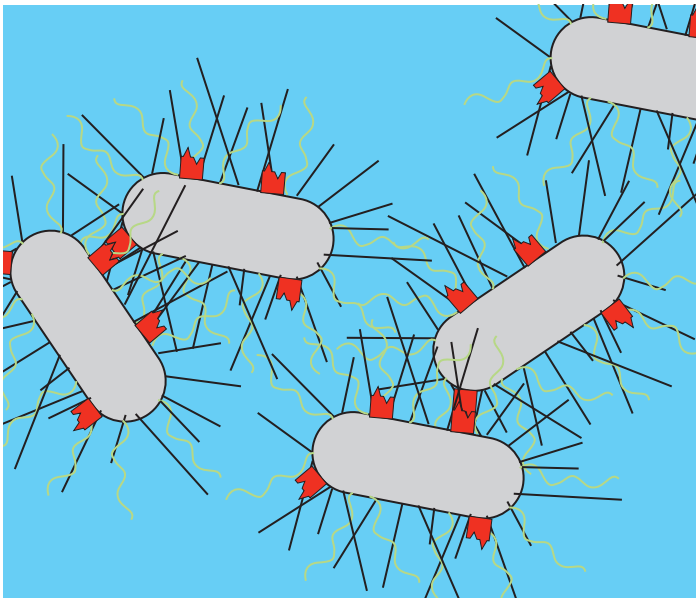

Figure 4.1: A depiction of an *E. coli* biofilm. Green: Curli created by the csg operon are curly hair like structures responsible for adhesion and extracellular matrix. Black: Fimbriae produced by the fim operon are straight hair like structures responsible for adhesion and extracellular matrix. Red: ag43 forms cell-cell dimers. Blue: Excreted polysaccharides form an extracellular matrix.

productive when preforming directed evolution or characterizing a synthetic circuit *in vivo*. In the case of directed evolutions the biofilm changes the selective pressures and ancestral cells be unfairly prevented from washout. In the case of genetic circuit characterization a biofilm changes the context under which the cells are grown by the inclusion of complex spacial structure (Figure 4.2b).

Table 4.1: List of genes and operons thought to be sufficient for biofilm formation

gene/operon	function
type 1 pili/fimbriae (fim)	sticky hair like structures
antigen 43 (ag43)	surface bound adhesive protein
curli (csg)	coiled hair like structure
pga	polysaccharide exportation system

Five genes/operons have been identified for deletion to create a biofilm free *E. coli* strain.

Of these, four are known to aid in either adhesion or extracellular matrix formation (Table 4.1, Figure 4.1), while the fifth (lux) is responsible for quorum sensing, which is used to detect the presence of biofilms.

Hair like structures formed by genes in the fimbriae operon (fim) and curlin operon (csg) are responsible for both attachment and extracellular matrix [51–53]. In *E. coli* fimbriae are expressed by the fim family of genes, which includes three adjacent transactional units the first two acting as regulators, while the the third is a seven gene operon coding the structural proteins that form fimbriae. Pratt and Kolter found that *E. coli* deficient in any of fimA-D were defective in growing biofilms on PVC surfaces, when grown in static ritch medium [54]. Unlike fibriae, the csgBAC operon expresses proteins that form coiled structures (curli) on the surface of *E. coli* citecurlin1989,curlin2000. Vidal *et al.* sampled biofilms that formed in continuous culture in minimal medium at 30 °C and found that in multiple cases, csg was up regulated [55].

A third gene thought to mediate cell-cell attachment is ag43 (aka flu). Diderichsen discovered that ag43 caused *E. coli* to autoaggregate and form frizzy colony morphologies [56]. Later, Danese *et al.* found that ag43 contributes to biofilm formation in minimal medium but not LB [57].

Quorum sensing also plays a roll in biofilm formation and maturation. In bacteria with luxS homologs, luxS was shown to both aid and hinder the form of bilofilms depending on strain and context. In mature biofilms, bacteria with mutant luxS homologs were shown to form thinner and looser biofilms likely because quorum sensing plays a role in the regulation of the extra cellular matrix [58].

Construction of a biofilm free E. coli

Starting with EcNR1, an MG1655 derived strain containing the lambda prophage [59], we made a series of sequential deletions requiring ten serial rounds of genome editing (Figure 4.2a and Table 4.2). The first three sequential knockouts, bla, fimAICDFGH, csgBAC, were accomplished by a recombineering method [60] that results in the insertion of a scar consisting of pcr homologies flanking an FRT site at the deletion locus. After the third

round integration efficiencies dropped to undetectable levels. The drop in efficiency came as a result of mistargeting due to left over homologies in previous rounds. The remaining rounds of serial deletions were accomplished through the use of a combination of the newer scarless recombineering method that includes the use of thyA selection/counter selection [61] and MAGE [59]. For each successful knockout the thyA gene was knocked out from the previous round using MAGE and screened on trimethoprim. Next, the thyA knock out was transformed with a double stranded constitutive thyA expression cassette that contained homologies flanking the deletion target. This sequence of insertion and scar-free deletion was repeated until all genes of interest were knocked out, yielding BF019.

Table 4.2: BF019 knockout homology list

deletion	5' homology / 3' homology
ag43	ATCTGAATACCTGCTACAGGCTGGTATGGAATCAC CAGCAGCGCTGAAGGGTATAACGGTCAGGCCACAC
csg	TGTACGACCAGGTCCAGGGTGACAACATGAAAAACAAATTG ATTTATCACAACAATGGCCGCCCTCTTCAGAAAAGTCTTAA
fim	ATTCGCCGACTGAAGAACGGATTTTCTACCGTTCACCCGTT AGTCACGCCAATAATCGATTGCACATTCCCTGCAGTCACCT
luxS	ATAGTTTACTGActaGATGTGCAGTTCCTGCAACT GGTATGATCGACTGTGAAGCTATCTAACAACGGca
pga	AGCCCGGGCGAACCGGGCTTTGTTTTGGGTGTTTA ATTACCCTTGCGAGCTTCAATAATCAATGCATCAT

Characterization of BF019

Biofilms are classically grown either by examining growth in micro titer plates or in continual flow devices [2]. We first characterized biofilm formation in round bottom 96 well plates using strain BF001 (EcNR1 Δbla) as a control. In the microtider assay, 24 of 24 wells inoculated with BF001 formed biofilms that were visible when crystal violet stained both at the air-liquid interface and on the well bottom, while 0 of 24 wells on the same plate inoculated with BF019 formed biofilms (Figure 4.1d).

With the microtider plate assay yielding positive results, we attempted to grow BF001

and BF019 in triplicate in the Flexostat, which is a continuous culture device capable of operating as a turbidostat [49]. Three culture vessels of each strain were inoculated and grown at an OD of 0.4 for two weeks or until a mature biofilm has formed. We define initial biofilm formation in the Flexostat as the point in time which dispersing biofilms cause disruptions and subsequent disturbances to the OD measurement and dilution rate. We define mature biofilms to be the point when the device can no longer dilute fast enough to maintain it's OD set point, meaning that the biofilm's contribution to OD is greater than the turbidostat set point. With in 2 days of reaching steady state OD, all BF001 strains had begun forming biofilms and by day 5 all three replicates had formed mature biofilms. In contrast, after two weeks the BF019 cultures had yet to show any signs of biofilms.

Phenotype changes

Aside from the inability to form biofilms, no other phenotypical changes were observed in BF019. Future work should include a more detailed study of important characteristics, such as transformation efficiency and gene expression to further validate it's suitability as a synthetic biology cell chassis.

4.2 Discussion

While not new, new techniques, technology, and scientific avenues are giving continuous culture new life. Until now no strain of *E. coli* has been reported that remains biofilm free for long durations in continuous culture. Our advancement, when combined with continuous culture devices such as the Flexostat [49], Ministat [15] or Morbidostat [12], will enable exciting new experiments in evolution, metabolic engineering, and synthetic biology.

The benefits to evolutionary biology and directed evolution are clear. The ability to hold cells in a consistent and well mixed environment enables experiments with constant selective pressures. Additionally, a simplified environment aids modeling where biomass, and substrate and metabolic byproduct concentrations are now constants rather than variables.

In addition to scientific applications our strain can be beneficial to synthetic biology. It is often the case that synthetic circuits like switches and oscillators have dynamics that can last longer than growth in batch will allow or have dynamics that are sensitive to changes

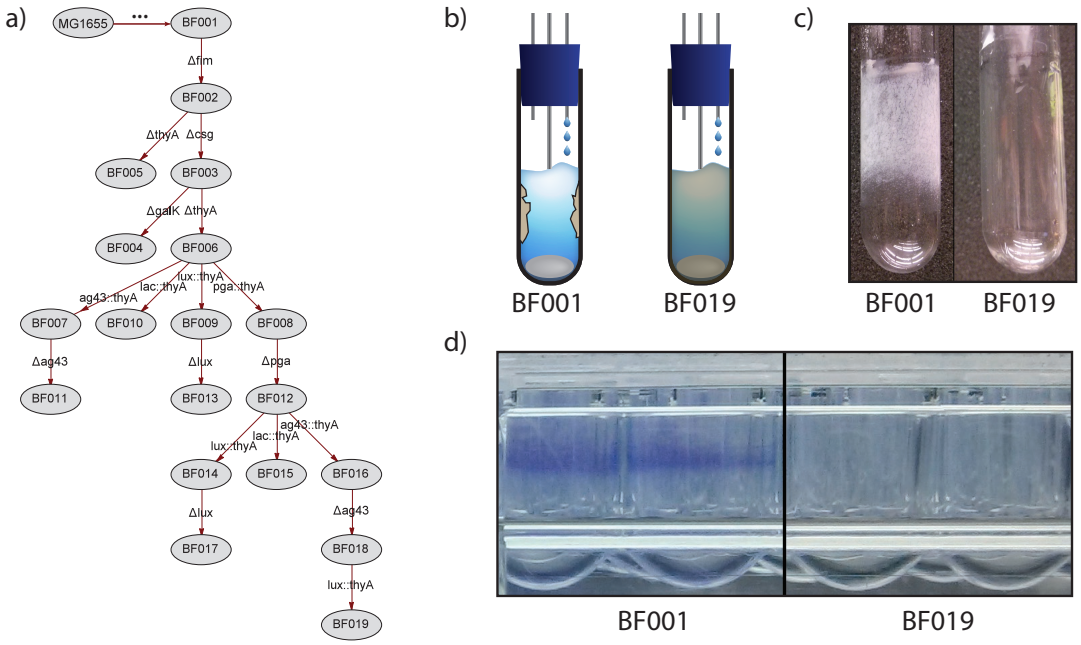

Figure 4.2: Comparison of wild type and BF019 a) A graph of sequential genomic manipulations used to create BF019. b) Cross-sectional schematic of a continuous culture vessel. Wild-type *E. coli* have formed a biofilm causing the washout of planktonic cells. BF019 cannot form biofilms and therefore stays in a planktonic state. b) Wild type vs. BF019 biofilm formation on glass culture tubes used in continuous culture. c) A standard crystal violet stained plate assay [2] showing WT vs BF019. Wild type *E. coli* readily forms biofilms near the gas-liquid interface and on the bottom of the well (not shown), while BF019 does not form detectable biofilms.

in environments [49]. When grown in well mixed continuous culture the dynamics of cell growth can be neglected as constants leaving only essential circuit characteristics to be identified. Additionally, BF019 can act as an anti-fouling chassis strain for circuits that are intended to be grown in continuous culture for long periods such as continual field testing of water sources [cite Hasty when published].

4.3 Materials and Methods

Recombineering

Recombining was done using two different protocols. BF001 through BF003 were created by inclusion of a kan cassette with flanking FRT recombination sites as described in Sharan et al. [62] for details. The only modification to this protocol was the use of strain EcNR1 [59] which has heat inducible lambda prophage integrated into it's genome, instead of on a plasmid.

BF004 through BF019 were constructed using a more modern, scarless thyA recombination protocol. The protocol was as in Wong [61] with the following exceptions. ThyA selection was done on plain LB agar plates while counter selection was done on LB agar plus $50\,\mu g\,mL^{-1}$ trimethoprim and $100\,\mu g\,mL^{-1}$ thymine. The thyA selectable marker was deleted using a MAGE oligo as opposed to a constructed dsDNA fragment.

Microtider plate assay

The microtider plate biofilm assay was conducted as in Merritt et al. [2]. 200 µL of LB was pipetted into each well of a 96 well plate and left at 30 °C in a shaker incubator for 24 h. The plates were then inverted and shaked empty. The emptied plates were then submerged in a rinse bath and inverted again to remove any planktonic cells. Finally, wells were stained with 300 µL crystal violet, rinsed a second time, dried and photographed.

Continuous culture assay

The continuous culture assay was preformed in the Flexostat [49] open source continuous culture device. Three replicates of each strain where gown in parallel at OD 0.4 from the same M9 0.1% glycerol 10mM Lactose media source. Once mature biofilms formed in a particular chamber, that chamber was shutoff individually to conserve media.

Chapter 5

EVOLUTIONARY HILLCLIMBS IN MANY TURBIDOSTATS

5.1 Introduction

There are many models of evolution [63–66], but they are typically designed to test hypothesis based on specific observations of natural phenomena [67]. Recently, with our increased capability to engineer biology, new questions need addressing. In particular, the class of problems related to optimizing metabolism in a laboratory environment, where fitness is far from optimal, is of particular interest to us. Such optimization problems are crucial for optimizing feedstock utilization in bioprocessing contexts and, with careful consideration for evolution, can be extended to synthetic biological circuits [68].

Here, we develop a model that eliminates the complexity of natural conditions in favor of the simplicity of laboratory conditions, in particular continuous culture. We combine steady state turbidostat and chemostat continuous dynamics with mutational events into a simple stochastic hybrid systems (SHS) [69] model. With our model we are able to compute analytically both the time to appearance of a more fit mutant and the time it takes to reach a majority of the population. This solution allows us to compute the optimal initial environment and population size for single and double step evolutionary hill climbs. We also show that for the case of two negatively epistatically interacting alleles the order of fixation may dramatically effect the time it takes to reach a fitness maximum.

Our model leads to the insight that for multi-step hill climbs uniformly sized steps are preferable to a combination of large and small steps due to the disproportionate time penalty small steps incur. This leads us to a control policy where large fitness jumps are counter-intuitively rejected in favor of smaller but more uniform fitness jumps. By applying this policy to a simulated metapopulation of multiple bioreactors we show that by replacing populations that are either unchanged or of higher fitness with populations that have undergone a modest fitness increase we can increase the rate of evolution. Finally,

we examine the effects of population and metapopulation size on the effectiveness of our control policy.

5.2 Evolutionary Dynamics

Fitness

Fitness is a property of an individual within a population that describes the likelihood of an individual's reproduction. Here, we define a cell's *fitness* to be its growth rate in units of 1/time.

In general, not all cells have the same fitness due to phenotypical differences. A cell's genome encodes the information necessary to consume substrate and reproduce, which along with the environment yields a phenotype with a particular growth rate. Therefore, depending on the desired level of detail one can define a map, called a *fitness function*, either from the space of genomes and environments or phenotypes onto fitness. The hypersurface defined by this map is often referred to as a *fitness landscape* because it resembles a hyper-dimensional landscape of valleys (fitness minima) and mountains (fitness maxima) [70].

Cellular reproduction is an error prone process occasionally resulting in a new type. Typically, an error will be neutral or deleterious, such as a defect in a vital protein. Occasionally, a mutation will convey an advantage that allows the mutant and its progeny to reproduce faster than its parent's type. When this happens, there is a chance that the new mutant type will take over the population (or "fixate") thereby moving the population "uphill" on the fitness landscape.

Selection in Fixed Sized Populations

A fixed (constant) population size means that for every microbe birthed one dies or is otherwise removed. Consider a population of N microbes of type A. A new mutant of type B may arise yielding a population of 1 B cell and $N-1$ A cells. The B cell may divide and give rise to a population of two cells of type B and $N-2$ of type A. Alternatively, the only cell of type B may be replaced by A and the population will return to N of type A. Two mutants of type B may then become three mutants or one, and so on. We model this

process as a "birth-death" process (Fig. 5.1) with state i_g which represents the number of cells with type g.

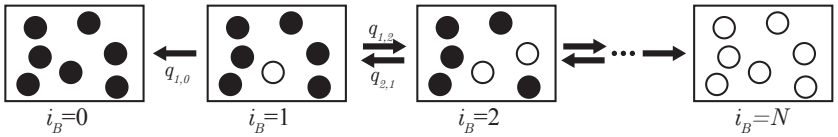

Figure 5.1: A birth death process with two absorbing states, $i = 0$ and $i = N$. In all other states transitions occur with $q_{i,i-1}$ and $q_{i,i+1}$ intensities.

At each epoch, a cell is chosen at random for division and a cell is chosen at random for death. Each type is chosen for division at a different rate so if type A is chosen at rate φ_A, B at rate φ_B, and B's relative fitness is $r := \varphi_B/\varphi_A$ then the state transition matrix Q is specified by

$$\begin{aligned} q_{i,i-1} &= \frac{N-i}{ri-N-i}\frac{i}{N} \\ q_{i,i} &= 1 - q_{i,i+1} - q_{i,i-1} \\ q_{i,i+1} &= \frac{ri}{ri+N-i}\frac{N-i}{N} \end{aligned} \tag{5.1}$$

and the probability that the absorbing state N is reached is

$$\rho(r) = \frac{1-1/r}{1-1/r^N}. \tag{5.2}$$

This birth death process is referred to as a Moran processes [71, 72].

Continuous Culture

Microbes are said to be grown in continuous culture when they are kept in an environment that continually adds growth medium. Here we consider the case of continuous culture with microbes growing in a constant volume of well mixed liquid media.

In large cultures, microbes of type i divide at a rate $\varphi_i(\mathbf{n}(t))$ that is a function of available nutrients $\mathbf{n}(t) = (n_1(t), n_2(t), ..., n_M(t))$ (from here on it will be implicitly assumed that $\mathbf{n}(t)$

is a function of time and its argument will be dropped). Here, we define a nutrient as any substance that affects the growth rate either beneficially or detrimentally. Given a nutrient concentration $\mathbf{n}$ and a population of microbes with type i of size $x_i(t)$, we have that

$$\dot{x}_i = \varphi_i(\mathbf{n})x_i, \tag{5.3}$$

where the growth rate $\varphi_i(\mathbf{n})$ is typically modeled as a monotonic function of its limiting nutrient (i.e. only a function of n_k for some k) with a bounded maximal growth rate (i.e. $\sup_{n\in\mathbb{R}^M_+} \varphi(\mathbf{n}) < \infty$) [33, 73].

Note that for unrestricted genome lengths there are potentially an infinite number of cell types and therefor the vector $\mathbf{x} := (x_1, x_2, \dots)$ may be of infinite length. However since microbial populations are finite, we can assume that there is only a finite number of types in existence over the course of an experiment.

As cells grow and divide, they consume nutrients and produce new cells. Including nutrient dynamics in (5.3) gives

$$\begin{aligned} \dot{x}_i &= \varphi(\mathbf{n})x_i \\ \dot{n} &= -\sum_i \frac{1}{\gamma}\varphi(\mathbf{n})x_i, \end{aligned} \tag{5.4}$$

where γ is the growth yield in terms of cells (or biomass) produced per unit nutrient.

In continuous culture, media is added at a rate $u(t)$ (from here on u) with concentration C and waste is removed at the same rate to maintain a constant volume. Adding dilution to the batch culture dynamics (5.4) gives

$$\begin{aligned} \dot{x}_i &= \varphi(\mathbf{n})x_i - ux_i \\ \dot{\mathbf{n}} &= -\sum_i \frac{1}{\gamma_i}\varphi_i(\mathbf{n})x_i - u\mathbf{n} + uC. \end{aligned} \tag{5.5}$$

Note that equation (5.5) applies to all well mixed communities of microbes including batch cultures ($u \equiv 0$), chemostats (u constant), and turbidostats, which we will discuss next.

Turbidostat Evolutionary Dynamics

A turbidostat is a continuous culture device where the total cell population is held constant. A fixed population size allows us to make simplifying assumptions and enables us to apply previous work by Moran [72] without loss of model accuracy. We begin by extending the chemostat model to a turbidostat. We then extend the ODE model to a stochastic hybrid systems model to capture the random nature of mutations.

Starting with the basic model of continuous culture, we have developed a refined model under the assumption that the turbidostat is at steady state density, i.e. that

$$\sum_i x_i(t) \approx \bar{x},\ \forall t > t_{ss} \tag{5.6}$$

for some desired population size $\bar{x}$. While a complete model would include turbidostat feedback dynamics, such a system would only differ in the moments soon after inoculation as any reasonable controller will act on timescales much faster than the growth of microbes.

Differentiating equation (5.6) we get $\sum_i \dot{x}_i(t) = 0$ (note: This differs from the steady state of the system where $\dot{x}_i = 0\ \forall i$), which implies that

$$u = \frac{\sum_i \varphi_i x_i}{\bar{x}}. \tag{5.7}$$

Substituting (5.7) into (5.5) yields,

$$\begin{aligned} \dot{x}_i &= x_i(\varphi_i(\mathbf{n}) - \bar{\varphi}(\mathbf{n})) \\ \dot{\mathbf{n}} &= -\sum_i x_i \varphi_i(n) \frac{1}{\gamma_i} + (C - \mathbf{n})\bar{\varphi}(\mathbf{n}), \end{aligned} \tag{5.8}$$

where $\bar{\varphi}$ is the weighted average growth rate,

$$\bar{\varphi}(\mathbf{n}) = \frac{\sum_i \varphi_i(\mathbf{n}) x_i}{\bar{x}}. \tag{5.9}$$

When considering basic bacterial growth in populations of billions of cells, mass action models such as (5.8) are accurate. However, when considering rare events such as muta-

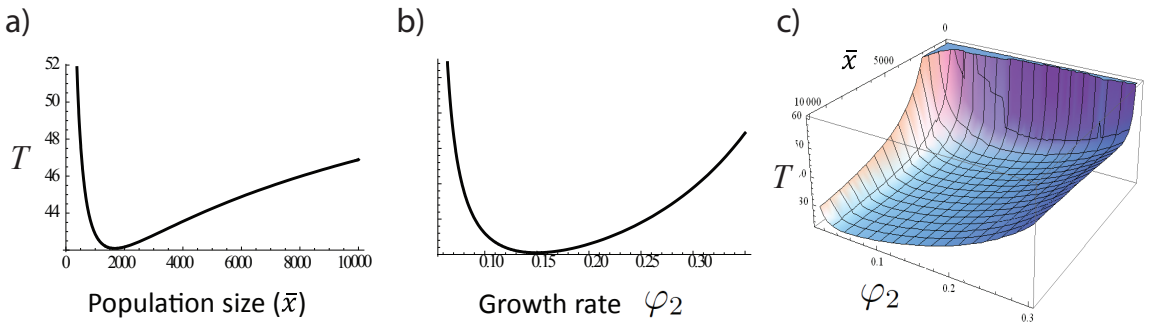

Figure 5.2: Expected time from homogeneous population to 50% novel mutant a) For small $\bar{x}$ the penalty grows close to $1/\bar{x}$ while for large $\bar{x}$ the penalty grows with $log(\bar{x})$ b) Growth rate, controlled through substrate concentrations, of the population also has an effect on the rate of evolution with a dramatic optimum. c) Evolutionary rate with with both variables left free.

tion mass action models become inaccurate accurate and stochastic models are preferable. To model growth dynamics and mutational dynamics together we use a stochastic hybrid systems(SHS) model [69]. In this model, equation (5.8) comprises the continuous state of a SHS that has reset maps

$$(x_i, x_j) \mapsto (x_i - 1, x_j + 1) \tag{5.10}$$

with transition intensities $\lambda_{ij}(x_i)$. For example, at rate $\lambda_{ij}(x_i)$ a member of type i mutates to type j, removing one cell of type i and adding one cell of type j. In order to model $\lambda_{ij}(x_i)$, we make the following assumptions:

1. Mutations are relatively rare and therefore fix sequentially in the absence of clonal interference.

2. The population is large ($\bar{x} > 1000$). This is true for most microbial populations of interest, excluding some microfluidic devices.

3. The population size is constant.

4. Mutations happen at a constant rate per reproduction event.

5. Cell and nutrient mass are at steady state.

Assumptions 1 and 2 imply the standard strong selection weak mutation (SSWM) assumption used in literature [74]. While assumptions 1 and 2 are stricter the SSWM assumption, assumption 2 is motivated by the experimental setup we are considering and is therefore more reasonable then simply taking SSWM outright. Assumptions 2 and 3 imply that substitution happens via a Moran process and therefore the probability that a new mutant fixes is a function of the relative fitness $r(\varphi_2, \varphi_1) := \varphi_2/\varphi_1$ given by

$$\rho(r) = \frac{1 - 1/r}{1 - 1/r^N} \approx \begin{cases} 1 - 1/r, & \text{if } r > 1 \\ 0, & \text{otherwise} \end{cases}. \tag{5.11}$$

For more detail see Nowak [71] and references within.

Suppose the current phenotype has fitness φ_1. The chance a new mutant that will eventually fix in the population arises in the next Δt seconds is proportional to the number of children born, $\varphi_1 x_1 \Delta t$, times the chance it has of fixing, $\rho(\varphi_2/\bar{\varphi})$. i.e.,

$$P(T_m < t + \Delta t | T_m > t, \varphi_2) \approx K_{1,2} \varphi_1 x_1 \rho\left(\varphi_2/\bar{\varphi}\right) \Delta t, \tag{5.12}$$

where T_m is the mutant's time of arrival and $K_{1,2}$ is some independent constant to represent proportionality as an equality. It follows from the definition of transition intensity [69] that

$$\begin{aligned} \lambda_{i,j}(x_i) &= \lim_{\Delta \to 0} P(T_m < t + \Delta t | T_m > t, \varphi_j) \\ &= K_{i,j} \varphi_i x_i \rho\left(\varphi_j/\bar{\varphi}\right). \end{aligned} \tag{5.13}$$

Evolutionary Rate in a Turbidostat

With the continuous dynamics (5.8) and the transition intensities (5.13) we can now compute the time it takes a small sub-population with greater than average fitness to sweep the population.

Here, we will define the *substitution time*, T_s, as the time it takes cell of type i to reach a population fraction of 50% starting from a single cell. This definition differs from what is

typically used when considering birth death processes. Since, these dynamics are continuous it is impossible to reach a population fraction of 1 in finite time when starting from an initial fraction of less than 1. Instead we choose a threshold where the novel cell type could be easily detected.

To compute the substitution time, we assume that the growth yield of subsequent mutants are similar yielding reduced dynamics

$$\dot{x}_i = x_i(\varphi_i - \bar{\varphi}), \tag{5.14}$$

where $\mathbf{n}$ is treated as constant at steady state cell densities and x may either be in units of cells or population fraction (i.e. x_i = number of cells of species i divided by the population size N) depending on the units of the initial conditions. For the remainder of this section we will use population fraction.

Equation (5.14) has solution

$$x_i(t) = \frac{\exp(\varphi_i t)}{\sum_j x_j(0)\exp(\varphi_j t)} x_i(0), \tag{5.15}$$

which may be used to solve $x_2(T_s) = 0.5$ for T_s yielding

$$T_s(\varphi_1, \varphi_2, \bar{x}) = \frac{\log(\bar{x} - 1)}{\varphi_2 - \varphi_1} \tag{5.16}$$

for $x_1(0) = 1 - 1/\bar{x}$, $x_2(0) = 1/\bar{x}$, and $\varphi_2 > \varphi_1$.

Next, we compute the time to appearance of the next mutant T_m, which is captured by a Poisson process [69]. If the population happens to be homogeneous, as we have assumed above, then we can compute the expected time to mutation by

$$E\{T_m | x_i = \bar{x}\} = \frac{1}{\sum_j \lambda_{i,j}}. \tag{5.17}$$

A turbidostat allows us to pick the population size $\bar{x}$, while a chemostat allows us to pick the average growth rate $\bar{\varphi}$. A turbidostat with mixture control enables us to control both $\bar{x}$ and $\bar{\varphi}$ by choosing a fixed dilution rate and then adjusting the ratio of media sources until

nutrient limitation is reached. This allows the population size $\bar{x}$ and the average growth rate $\bar{\varphi}$ to be free variables. The time to appearance and substitution of a new mutant with fitness φ_2 given a homogeneous population with fitness φ_1 is

$$\begin{aligned} T(\bar{x}, \varphi; 1, 2) &= \mathbb{E}\{T_m | x_1 = \bar{x}\} + T_s(\bar{x}, \varphi_1) \\ &= \frac{1}{K\varphi_1 \bar{x} \rho\left(\varphi_2/\varphi_1\right)} + \frac{\log(\bar{x} - 1)}{\varphi_2 - \varphi_1}. \end{aligned} \tag{5.18}$$

The time to appearance and substitution given in equation (5.18) has no closed form minimum over $(\bar{x}, \varphi_1)$ but may be minimized numerically (Fig. 5.2).

Avoiding Clonal Interference

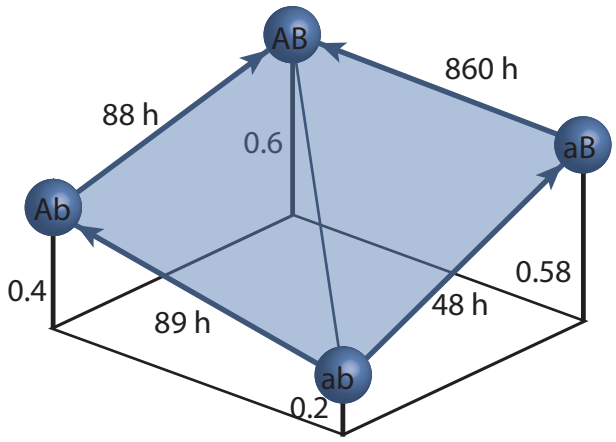

Figure 5.3: Example fitness landscape suffering from negative epistasis. In this example, two loci are considered each with two alleals, yielding four genotypes, ab, Ab, aB, and AB. Node weights denote growth rate per hour. Edge weights denote the expected time to sweep for an optimal population size, $T^*(\varphi; \cdot, \cdot)$, given a mutation rate of 10^{-7} per cell division.

We can now use our evolutionary model to explore a more complex landscape involving two alleles and negative epistasis (Fig 5.3). Applying our previous result to two substitution events with the optimal population size we get that the time to substitution of AB along the path ab $\rightarrow$ Ab $\rightarrow$ AB is $\arg\min_{\bar{x}}\{T(\tilde{\bar{x}}, \varphi; ab, Ab) + T(\tilde{\bar{x}}, \varphi; Ab, AB)\} \approx 177$ h while the substitution time along the path ab $\rightarrow$ aB $\rightarrow$ AB is approximately 907 h. Clearly the

former path is preferable from an engineering standpoint, however due to clonal interference, if phenotype aB arises at any point before phenotype AB, final fixation of AB will progress more slowly due to type aB's superior growth rate with respect to type Ab and AB's small improvement over aB [75]. Indeed, regardless of weather AB arises for Ab or aB, the population dynamics (5.15) imply that the progress of type AB's sweep relative to aB happens at a rate $\varphi_{AB} - (\varphi_{aB}x_{aB} - \varphi_{AB}x_{AB})/(x_{aB} + x_{AB})$, which is very small for small differences growth rate and will delay the fixation of AB when the ratio of x_{aB}/x_{AB} is significant.

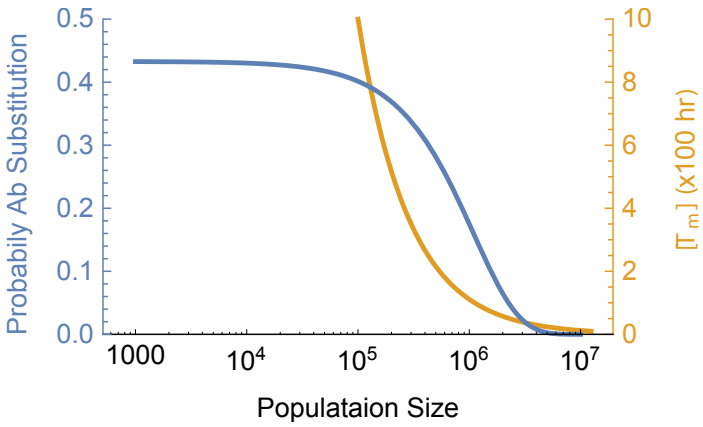

Figure 5.4: Tradeoff between T_m and chances that Ab fixes. Blue) The probability of evolution progressing through Ab as a function of population size ($\bar{x}$) expressed in equation (5.19) with mutation rate $k = 10^{-7}$. The probability remains nearly constant until $\bar{x} = 10^5$ at which point it drops off sharply reaching nearly zero by $\bar{x} = 10^7$. Orange) The expected time in hours it takes for type Ab to appear from a population of type ab.

To explore conditions under which evolution is optimized in this environment we compute the probability that an evolutionary trajectory will progress along ab $\rightarrow$ Ab $\rightarrow$ AB, which can be approximated by

$$\begin{aligned}\mathbb{P}[Ab] &:= \mathbb{P}\left[T_m(ab, Ab) + T_s(\varphi_{ab}, \varphi_{aB}, \bar{x}) < T_m(ab, aB)\right] = \\ &= \frac{\varphi_{aB}(\varphi_{ab} - \varphi_{Ab})(\bar{x} - 1)^{\frac{k\bar{x}\varphi_{ab}(\varphi_{aB} - \varphi_{ab})}{\varphi_{aB}(\varphi_{ab} - \varphi_{Ab})}}}{\varphi_{ab}(\varphi_{aB} + \varphi_{Ab}) - 2\varphi_{aB}\varphi_{Ab}}\end{aligned} \tag{5.19}$$

and plotted (Fig 5.4) with numerical values substituted from our example. Equation (5.19)

then allows us to optimize the rate of two step evolution for known fitness landscapes. We get that the expected time to substitution of AB starting from ab, T_{AB}, is

$$\begin{aligned} T_{AB} := &\left(T(\bar{x}, \varphi; ab, Ab) + T(\bar{x}, \varphi; Ab, AB)\right) \mathbb{P}[Ab] + \\ &+ \left(T(\bar{x}, \varphi; ab, aB) + T(\bar{x}, \varphi; aB, AB)\right) (1 - \mathbb{P}[Ab]). \end{aligned} \tag{5.20}$$

T_{AB} can be minimized over $\bar{x}$ to find an optimal population size. Indeed, equation (5.19) becomes

$$\begin{aligned} T_{AB}(\bar{x}) = &\frac{29}{67}(\bar{x}-1)^{-\frac{19\bar{x}}{290000000}} \left(\frac{175000000}{\bar{x}} + 10\log(\bar{x}-1)\right) + \\ &+ \left(1 - \frac{29}{67}(\bar{x}-1)^{-\frac{19\bar{x}}{290000000}}\right) \left(\frac{327050000000}{551\bar{x}} + \frac{1000}{19}\log(\bar{x}-1)\right) \end{aligned} \tag{5.21}$$

with all parameters substituted. When minimized over $\bar{x}$ we get $T_{AB}(1.12723 \times 10^7) = 907.278$. Minimizing just the path through aB gives

$$\arg\min_{\bar{x}} T(\bar{x}, \varphi; ab, aB) + T(\bar{x}, \varphi; aB, AB) = 1.12776 \times 10^7 \tag{5.22}$$

and

$$T(1.12776 \times 10^7, \varphi; ab, aB) + T(1.12776 \times 10^7, \varphi; aB, AB) = 907.28 \tag{5.23}$$

which is nearly identical to the solution that optimizes both paths simultaneously.

Intuitively, the reason why considering both paths does not give a substantially different optimum is because the expected time to first appearance of a new mutant ($\mathbb{E}[T_m]$) is proportional to the inverse of the population size. Therefore, the increase in probability that Ab will fixate (which precludes the appearance of aB) is out weighed by the increase in $\mathbb{E}[T_m]$ (Fig 5.4). However, if we instead pick a new optimal cell density after fixation of each new mutant, we can partially mitigate the effects of a low cell density. In this case

equation (5.20) becomes

$$T^*_{AB} := \left(T(\bar{x}, \varphi; ab, Ab) + T^*(\varphi; Ab, AB)\right) \mathbb{P}[Ab] + \\ + \left(T(\bar{x}, \varphi; ab, aB) + T^*(\varphi; aB, AB)\right) (1 - \mathbb{P}[Ab]), \tag{5.24}$$

where $T^*(\varphi; a, b) := \min_{\bar{x}} T(\bar{x}, \varphi; a, b)$. T^*_{AB} has now has a minimum 837 h at $\bar{x} = 7 \times 10^6$.

Rapid Evolution in an N-plex turbidostat

In the previous section, we showed that for the case of episatis there is a fastest evolutionary path. For the case of negative episatis, clonal interference ensures that the probability that the fastest path will be takes is never more than 50%. Recent developments have made small multiplex bioreactors possible [15, 49] enabling parallel evolutions. In the parallel case an experimenter only needs a single bioreactor's population to complete a hill climb before the evolved strain can be collected. This multiplex experimental setup then allows us to model the evolution of our meta-population (the population of individual communities within each bioreactor) as a N individual Bernoulli trials. For the two locus example, the probability of success (taking the faster path) is given in equation (5.19) and the probability that at least one of N cultures evolves along the fastest path is

$$P[\text{number fastest path} > 0] = 1 - (1 - \mathbb{P}[Ab])^N . \tag{5.25}$$

We can now subject equation (5.25) to either specification (e.g. Find $\bar{x}$ so that there is a 95% chance of at least one population taking the fastest path) or optimization. Fig. 5.5 shows the expected time and optimal per bioreactor population size as a function of number of bioreactors. Adding multiple bioreactors significantly decreases the wait time for an evolved strains with returns diminishing beyond 15 bioreactors.

A control strategy for evolutionary hill climbs in parallel turbidostats

In prior sections, our optimization strategies have required exact knowledge of the fitness landscape. In practice this information is rarely known. Instead, estimates of optimal fitness

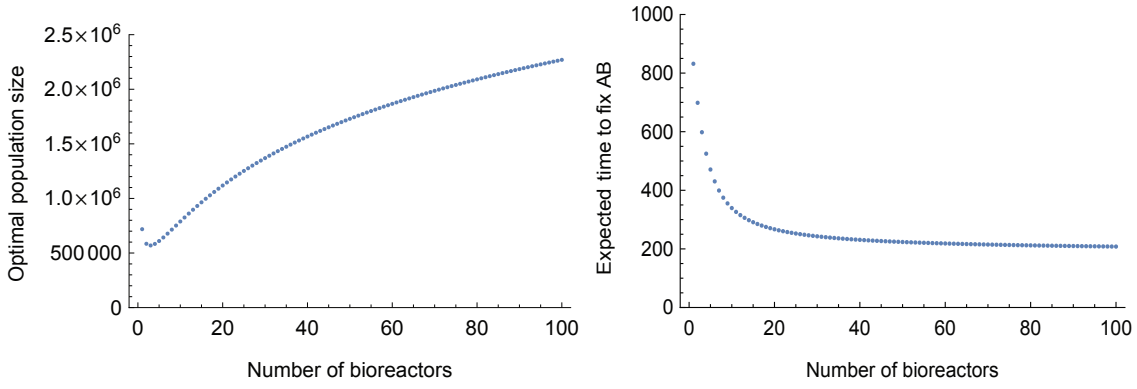

Figure 5.5: The relationship between the number of bioreactors and optimal rate of evolution. Top: As the number of bioreactors increases the optimal population also increases. Intiuitevly, this is because only one need bioreactor needs to follow the fast path allowing more populations to take "risks" with larger populations size that birth mutantants at higher rates. Bottom: The expected time to fix AB at optimal population size for a given number of bioreactors. As you increase the number of bioreactors there are diminshing returns near 10 bioreactors.

may be available by applying knowledge of the metabolic load of expressing enzymes as well as the fitness benefit of downstream metabolites. With an estimate of the optimum fitness and insights gained from the previous sections, we can devise a heuristic control strategy to accelerate evolutionary hill climbs in parallel turbidostats.

We believe that the following heuristics apply in general and can be used to generate a control strategies that accelerate hill climbs of metapopulations.

1. Due to clonal interference, populations on the same order (or greater) as the mutation rate tend to take the largest fitness jumps available.

2. Larger jumps provide diminishing returns and should be avoided.

Using the stated heuristics, we have devised the control strategy outlined in Algorithm 1. To evaluate our control strategy we compared it's performance in simulation to that of the null strategy where N turbidostats are inoculated but left without further manipulations.

Our simulation implements the SHS with continuous state as in equation (5.14) and reset map given in equation (5.10) and terminates when a single chamber reaches 50% population

Algorithm 1

Inoculate N turbidostats
$\varphi_m \leftarrow$ growth rate of inoculum.
$\varphi_M \leftarrow$ hypothesized maximal growth rate.
while $\varphi_m < \varphi_M$ **do**
    for all chambers c **do**
        $\varphi_c \leftarrow$ growth rate of chamber c
        $\Delta \leftarrow \varphi_M - \varphi_m$
        if $\varphi_M - 0.25\Delta > \varphi_c > \varphi_m + 0.25\Delta$ **then**
            Restart all chambers from chamber c
            $\varphi_m \leftarrow \varphi_c$

fraction of the most fit type. We choose a randomly generated fitness landscape with three epistatically interacting loci (e.g. binding affinity, expression, and importation), each with a single alternate allele conferring a fitness benefit regardless of order of fixation (i.e. no sign episatis). Fig 5.6 shows the mean time reach the fitness peak for Algorithm 1 vs the null algorithm. Comparing Algorithm 1 with the null algorithm we see an improvement of nearly 40%. In addition to the improved optimal time, Algorithm 1 is also much more robust to the choice of an overly small population and is no worse than the null algorithm for large populations. The robustness of Algorithm 1 is an important feature because the a precise value for the optimal population size is not known a priori.

Discussion

We introduce a simplified stochastic hybrid systems model that captures the general features of evolving populations in a turbidostat while remaining analytically tractable. With our model we show that the expected time to reach an evolutionary fitness peak can be computed analytically when the fitness landscape is known. From the analytical expression for expected time to hill climb we can optimize the population size to minimize the time to fixation of the most fit genotype. Our optimization then leads to a set of heuristics that can be used to devise control strategies to further optimize the time to evolve by directly manipulating meta-populations of turbidostats. We show that one such control method enables acceleration of evolution by nearly 40% while also making the evolutionary time more robust to choice of population.

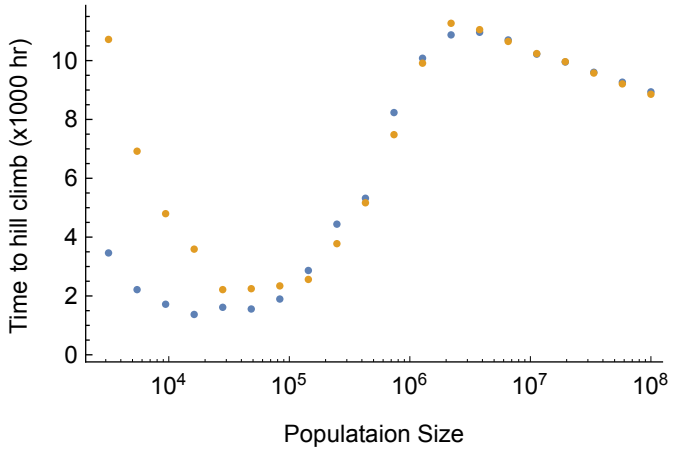

Figure 5.6: Performance of Algorithm 1 vs null algorithm for eight turbidostats. **Orange)** Mean time to hill climb of the null algorithm vs population size. **Blue)** Mean time to hill climb versus the choosen population size. Algorithm 1 still performs well when the population is chosen smaller than is optimal and performs no worse than null for large populations.

Recent work has enabled the real world application of these control policies [12, 15, 49]. Applications could include metabolic engineering problems where optimal growth rates can be extrapolated from known systems, and synthetic biology where it may be used to predict how "unhealthy" a cell may be made before it is likely to mutate in a given time span. Systems where engineered performance can be tied to metabolism may also benefit by showing experimenters how to optimize conditions, which in turn will increase research productivity.

In addition to direct applications, future work may focus on alternate algorithms for controlling meta-populations of turbidostats. Algorithms that allow a wider breath of evolutionary paths simultaneously may work better, especially in rugged landscapes. The application of stochastic remixing of populations may also provide more robust of faster control strategies. We believe that further exploration will reveal a rich space of control methods that have implications for both engineering and experimental evolution.

BIBLIOGRAPHY

[1] K. A. Havens, J. M. Guseman, S. S. Jang, E. Pierre-Jerome, N. Bolten, E. Klavins, and J. L. Nemhauser, "A synthetic approach reveals extensive tunability of auxin signaling," *Plant Physiol.*, vol. 160, pp. 135–142, Sep 2012.

[2] J. H. Merritt, D. E. Kadouri, and G. A. O'Toole, "Growing and Analyzing Static Biofilms," in *Current Protocols in Microbiology* (R. Coico, T. Kowalik, J. Quarles, B. Stevenson, and R. Taylor, eds.), Hoboken, NJ, USA: John Wiley & Sons, Inc., Aug. 2011.

[3] J. N. Zadeh, C. D. Steenberg, J. S. Bois, B. R. Wolfe, M. B. Pierce, A. R. Khan, R. M. Dirks, and N. A. Pierce, "{nupack}: Analysis and design of nucleic acid systems," *J. Comput. Chem.*, vol. 32, pp. 170–173, jan 2011.

[4] A. S. Khalil and J. J. Collins, "Synthetic biology: applications come of age," *Nat Rev Genet*, vol. 11, pp. 367–379, may 2010.

[5] *Synthetic Biology: Industrial and Environmental Applications*. Wiley-Blackwell, 2012.

[6] A. Arkin, "Setting the standard in synthetic biology," *Nat Biotechnol*, vol. 26, pp. 771–774, jul 2008.

[7] O. Kuchner and F. H. Arnold, "Directed evolution of enzyme catalysts," *Trends in Biotechnology*, vol. 15, no. 12, pp. 523 – 530, 1997.

[8] P. Modrich and R. Lahue, "Mismatch repair in replication fidelity, genetic recombination, and cancer biology," *Annu. Rev. Biochem.*, vol. 65, pp. 101–133, jun 1996.

[9] A. Novick and L. Szilard, "Description of the chemostat," *Science*, vol. 112, no. 2920, pp. 715–716, 1950.

[10] V. BRYSON and W. SZYBALSKI, "Microbial selection," *Science*, vol. 116, pp. 45–51, Jul 1952.

[11] K. Tomson, J. Barber, and K. Vanatalu, "Adaptastat–a new method for optimising of bacterial growth conditions in continuous culture: Interactive substrate limitation based on dissolved oxygen measurement," *J. Microbiol. Methods*, vol. 64, pp. 380–390, Mar 2006.

[12] E. Toprak, A. Veres, J. B. Michel, R. Chait, D. L. Hartl, and R. Kishony, "Evolutionary paths to antibiotic resistance under dynamically sustained drug selection," *Nat. Genet.*, vol. 44, pp. 101–105, Jan 2012.

[13] K. M. Esvelt, J. C. Carlson, and D. R. Liu, "A system for the continuous directed evolution of biomolecules," *Nature*, vol. 472, pp. 499–503, Apr 2011.

[14] R. W. Lovitt and J. W. T. Wimpenny, "The gradostat: a bidirectional compound chemostat and its application in microbiological research," *Microbiology*, vol. 127, pp. 261–268, Dec 1981.

[15] A. W. Miller, C. Befort, E. O. Kerr, and M. J. Dunham, "Design and use of multiplexed chemostat arrays," *Journal of Visualized Experiments*, Feb 2013.

[16] G. H. Markx, C. L. Davey, and D. B. Kell, "The permittistat: a novel type of turbidostat," *Journal of General Microbiology*, vol. 137, pp. 735–743, Apr 1991.

[17] G. Larsson, S.-O. Enfors, and H. Pham, "The ph-auxostat as a tool for studying microbial dynamics in continuous fermentation," *Biotechnology and Bioengineering*, vol. 36, pp. 224–232, Jul 1990.

[18] W. Tappe, C. Tomaschewski, S. Rittershaus, and J. Groeneweg, "Cultivation of nitrifying bacteria in the retentostat, a simple fermenter with internal biomass retention," *FEMS Microbiology Ecology*, vol. 19, no. 1, pp. 47 – 52, 1996.

[19] T. M. Conrad, N. E. Lewis, and B. Ø. Palsson, "Microbial laboratory evolution in the era of genome-scale science," *Molecular systems biology*, vol. 7, no. 1, p. 509, 2011.

[20] E. Dekel and U. Alon, "Optimality and evolutionary tuning of the expression level of a protein," *Nature*, vol. 436, pp. 588–592, Jul 2005.

[21] N. Kashtan, E. Noor, and U. Alon, "Varying environments can speed up evolution," *Proceedings of the National Academy of Sciences*, vol. 104, pp. 13711–13716, August 2007.

[22] R. Fisher, *The genetical theory of natural selection*. Oxford: Clarendon Press, 1930.

[23] J. Gillespie, *The cause of Molecular Evolution*. Oxford: Oxford University Press, 1991.

[24] R. E. Lenski, "Long-term evolution experiment with *e. coli*, publication list," 2010. `http://myxo.css.msu.edu/ PublicationSearchResults.php?group=aad`.

[25] B. Canton, A. Labno, and D. Endy, "Refinement and standardization of synthetic biological parts and devices," *Nat. Biotechnol.*, vol. 26, pp. 787–793, Jul 2008.

[26] H. Alper, C. Fischer, E. Nevoigt, and G. Stephanopoulos, "Tuning genetic control through promoter engineering," *Proc. Natl. Acad. Sci. U.S.A.*, vol. 102, pp. 12678–12683, Sep 2005.

[27] E. Olson, L. Hartsough, B. Landry, R. Shroff, and J. Tabor, "Characterizing bacterial gene circuit dynamics with optically programmed gene expression signals," *Nature Methods*, vol. in press, 2014.

[28] F. Ceroni, S. Furini, A. Stefan, A. Hochkoeppler, and E. Giordano, "A synthetic post-transcriptional controller to explore the modular design of gene circuits," *ACS Synthetic Biology*, vol. 1, pp. 163–171, May 2012.

[29] J. R. Kelly, A. J. Rubin, J. H. Davis, C. M. Ajo-Franklin, J. Cumbers, M. J. Czar, K. de Mora, A. L. Glieberman, D. D. Monie, and D. Endy, "Measuring the activity of BioBrick promoters using an in vivo reference standard," *J Biol Eng*, vol. 3, p. 4, 2009.

[30] J. C. Anderson, C. A. Voigt, and A. P. Arkin, "Environmental signal integration by a modular and gate," *Molecular Systems Biology*, vol. 3, Aug 2007.

[31] V. K. Mutalik, J. C. Guimaraes, G. Cambray, Q.-A. Mai, M. J. Christoffersen, L. Martin, A. Yu, C. Lam, C. Rodriguez, G. Bennett, and et al., "Quantitative estimation of activity and quality for collections of functional genetic elements," *Nature Methods*, vol. 10, pp. 347–353, Mar 2013.

[32] V. K. Mutalik, J. C. Guimaraes, G. Cambray, C. Lam, M. J. Christoffersen, Q.-A. Mai, A. B. Tran, M. Paull, J. D. Keasling, A. P. Arkin, and et al., "Precise and reliable gene expression via standard transcription and translation initiation elements," *Nature Methods*, vol. 10, pp. 354–360, Mar 2013.

[33] J. Monod, "The growth of bacterial cultures," *Annual Review of Microbiology*, vol. 3, no. 1, pp. 371–394, 1949.

[34] M. J. Brauer, C. Huttenhower, E. M. Airoldi, R. Rosenstein, J. C. Matese, D. Gresham, V. M. Boer, O. G. Troyanskaya, and D. Botstein, "Coordination of growth rate, cell cycle, stress response, and metabolic activity in yeast," *Mol. Biol. Cell*, vol. 19, pp. 352–367, Jan 2008.

[35] K. Valgepea, K. Adamberg, A. Seiman, and R. Vilu, "Escherichia coli achieves faster growth by increasing catalytic and translation rates of proteins," *Molecular BioSystems*, vol. 9, no. 9, p. 2344, 2013.

[36] M. Scott, C. W. Gunderson, E. M. Mateescu, Z. Zhang, and T. Hwa, "Interdependence of cell growth and gene expression: Origins and consequences," *Science*, vol. 330, pp. 1099–1102, Nov 2010.

[37] J. Monod, "La technique de culture continue, theorie et applications," *Annales d'Institute Pasteur*, vol. 79, pp. 390–410, 1950.

[38] A. J. Saldanha, M. J. Brauer, and D. Botstein, "Nutritional homeostasis in batch and steady-state culture of yeast," *Mol. Biol. Cell*, vol. 15, pp. 4089–4104, Sep 2004.

[39] E. Toprak, A. Veres, S. Yildiz, J. M. Pedraza, R. Chait, J. Paulsson, and R. Kishony, "Building a morbidostat: an automated continuous-culture device for studying bacterial drug resistance under dynamically sustained drug inhibition," *Nature Protocols*, vol. 8, pp. 555–567, Feb. 2013.

[40] J. J. Collins, T. S. Gardner, and C. R. Cantor *Nature*, vol. 403, pp. 339–342, Jan 2000.

[41] P. Wang, L. Robert, J. Pelletier, W. L. Dang, F. Taddei, A. Wright, and S. Jun, "Robust growth of Escherichia coli," *Curr. Biol.*, vol. 20, pp. 1099–1103, Jun 2010.

[42] Accuri, *BD Accuri C6 Flow Cytometer Technical Specifications*. BD Biosciences.

[43] R. C. Dorf and R. H. Bishop, *Modern Control Systems*. Prentice Hall, 10th ed., 2005.

[44] C. Takahashi, F. Ekness, and E. Klavins, "Open source mixture controlled turbidostat." http://students.washington.edu/cnt/pmwiki/, Dec. 2012.

[45] E. B. Joel, "How to solder - through-hole soldering." `https://learn.sparkfun.com/tutorials/how-to-solder---through-hole-soldering`, 2015.

[46] B. Jepson, T. Moskowite, and G. Hayes, *Learn to Solder: Tools and Techniques for Assembling Electronics*. Maker Media, Inc, 2012.

[47] J. D. Bryers, "Biofilm formation and chemostat dynamics: Pure and mixed culture considerations," *Biotechnology and Bioengineering*, vol. 26, pp. 948–958, Aug. 1984.

[48] W. S. Lo and A. M. Dranginis, "FLO11, a yeast gene related to the STA genes, encodes a novel cell surface flocculin," *Journal of Bacteriology*, vol. 178, pp. 7144–7151, Dec. 1996.

[49] C. N. Takahashi, A. W. Miller, F. Ekness, M. J. Dunham, and E. Klavins, "A low cost, customizable turbidostat for use in synthetic circuit characterization," *ACS Synthetic Biology*, vol. 4, no. 1, pp. 32–38, 2015.

[50] "Klavins lab hardware." `http://klavinslab.org/hardware`.

[51] C. C. Brinton, "The structure, function, synthesis and genetic control of bacterial pili and a molecular model for DNA and RNA transport in gram negative bacteria," *Trans N Y Acad Sci*, vol. 27, pp. 1003–1054, Jun 1965.

[52] A. Olsen, A. Jonsson, and S. Normark, "Fibronectin binding mediated by a novel class of surface organelles on Escherichia coli," *Nature*, vol. 338, pp. 652–655, Apr 1989.

[53] C. Prigent-Combaret, G. Prensier, T. T. Le Thi, O. Vidal, P. Lejeune, and C. Dorel, "Developmental pathway for biofilm formation in curli-producing Escherichia coli strains: role of flagella, curli and colanic acid," *Environ. Microbiol.*, vol. 2, pp. 450–464, Aug 2000.

[54] L. A. Pratt and R. Kolter, "Genetic analysis of Escherichia coli biofilm formation: roles of flagella, motility, chemotaxis and type I pili," *Mol. Microbiol.*, vol. 30, pp. 285–293, Oct 1998.

[55] O. Vidal, R. Longin, C. Prigent-Combaret, C. Dorel, M. Hooreman, and P. Lejeune, "Isolation of an Escherichia coli K-12 mutant strain able to form biofilms on inert surfaces: involvement of a new ompR allele that increases curli expression," *J. Bacteriol.*, vol. 180, pp. 2442–2449, May 1998.

[56] B. Diderichsen, "flu, a metastable gene controlling surface properties of Escherichia coli," *J. Bacteriol.*, vol. 141, pp. 858–867, Feb 1980.

[57] P. N. Danese, L. A. Pratt, S. L. Dove, and R. Kolter, "The outer membrane protein, antigen 43, mediates cell-to-cell interactions within Escherichia coli biofilms," *Mol. Microbiol.*, vol. 37, pp. 424–432, Jul 2000.

[58] M. R. Parsek and E. Greenberg, "Sociomicrobiology: the connections between quorum sensing and biofilms," *Trends in Microbiology*, vol. 13, pp. 27–33, Jan. 2005.

[59] H. H. Wang, F. J. Isaacs, P. A. Carr, Z. Z. Sun, G. Xu, C. R. Forest, and G. M. Church, "Programming cells by multiplex genome engineering and accelerated evolution," *Nature*, vol. 460, pp. 894–898, Aug 2009.

[60] K. C. Murphy, "Use of bacteriophage lambda recombination functions to promote gene replacement in Escherichia coli," *J. Bacteriol.*, vol. 180, pp. 2063–2071, Apr 1998.

[61] Q. N. Y. Wong, "Efficient and seamless {dna} recombineering using a thymidylate synthase a selection system in escherichia coli," *Nucleic Acids Research*, vol. 33, pp. e59–e59, mar 2005.

[62] S. K. Sharan, L. C. Thomason, S. G. Kuznetsov, and D. L. Court, "Recombineering: a homologous recombination-based method of genetic engineering," *Nat Protoc*, vol. 4, no. 2, pp. 206–223, 2009.

[63] C. Ofria and C. O. Wilke, "Avida: A software platform for research in computational evolutionary biology," *Artificial Life*, vol. 10, pp. 191–229, mar 2004.

[64] T. S. Ray, "Synthetic life: Evolution and optimization of digital organisms," in *Scientific Excellence in Supercomputing: The 1990 IBM Contest Prize Papers* (K. R. Billingsley, B. H. U. Iii, and E. Derohanes, eds.), pp. 489–531, 1992.

[65] S. Kauffman and S. Levin, "Towards a general theory of adaptive walks on rugged landscapes," *Journal of Theoretical Biology*, vol. 128, pp. 11–45, sep 1987.

[66] S. GERITZ, E. KISDI, G. MESZENA, and J. METZ *Evolutionary Ecology*, vol. 12, no. 1, pp. 35–57, 1997.

[67] S. P. Otto and T. Day, *A biologist's guide to mathematical modeling in ecology and evolution*, vol. 13. Princeton University Press, 2007.

[68] S. Raman, J. K. Rogers, N. D. Taylor, and G. M. Church, "Evolution-guided optimization of biosynthetic pathways," *Proceedings of the National Academy of Sciences*, vol. 111, no. 50, pp. 17803–17808, 2014.

[69] J. P. Hespanha, "Modelling and analysis of stochastic hybrid systems.," *IEE Proceedings – Control Theory & Applications*, vol. 153, no. 5, pp. 520 – 535, 2006.

[70] S. Wright, "The roles of mutation, inbreeding, crossbreeding, and selection in evolution," *Proceedings of the Sixth International Congress on Genetics*, pp. 356–366, 1932.

[71] M. A. Nowak, *Evolutionary Dynamics: Exploring the Equations of Life*. Harvard University Press, 2006.

[72] P. A. P. Moran, *The statistical processes of evolutionary theory*. Clarendon Press, 1962.

[73] H. L. Smith and P. Waltman, *The Theory of the Chemostat*. Cambridge University Press, 1995.

[74] J. H. Gillespie, "Some properties of finite populations experiencing strong selection and weak mutation," *The American Naturalist*, vol. 121, no. 5, pp. pp. 691–708, 1983.

[75] P. Gerrish and R. Lenski, "The fate of competing beneficial mutations in an asexual population," *Genetica*, vol. 102-103, no. 0, pp. 127–144, 1998.

[76] D. G. Gibson, L. Young, R.-Y. Chuang, J. C. Venter, C. A. Hutchison, and H. O. Smith, "Enzymatic assembly of {dna} molecules up to several hundred kilobases," *Nat Meth*, vol. 6, pp. 343–345, apr 2009.

[77] R. Calendar, ed., *The bacteriophages*. Oxford ; New York: Oxford University Press, 2nd ed ed., 2006.

[78] N. G. Copeland, N. A. Jenkins, and D. L. Court, "Recombineering: a powerful new tool for mouse functional genomics," *Nat Rev Genet*, vol. 2, pp. 769–779, oct 2001.

[79] Y. Zhang, F. Buchholz, J. P. Muyrers, and A. F. Stewart, "A new logic for DNA engineering using recombination in Escherichia coli," *Nat. Genet.*, vol. 20, pp. 123–128, Oct 1998.

[80] J. A. Mosberg, M. J. Lajoie, and G. M. Church, "Lambda red recombineering in escherichia coli occurs through a fully single-stranded intermediate," *Genetics*, vol. 186, pp. 791–799, sep 2010.

[81] M. Maresca, A. Erler, J. Fu, A. Friedrich, Y. Zhang, and A. F. Stewart, "Single-stranded heteroduplex intermediates in λ red homologous recombination," {*BMC*} *Mol Biol*, vol. 11, no. 1, p. 54, 2010.

[82] T. Baba, T. Ara, M. Hasegawa, Y. Takai, Y. Okumura, M. Baba, K. A. Datsenko, M. Tomita, B. L. Wanner, and H. Mori, "Construction of escherichia coli k-12 in-frame, single-gene knockout mutants: the keio collection," *Mol Syst Biol*, vol. 2, feb 2006.

[83] B. Strauss, K. Kelly, and D. Ekiert, "Cytochrome oxidase deficiency protects escherichia coli from cell death but not from filamentation due to thymine deficiency or {dna} polymerase inactivation," *Journal of Bacteriology*, vol. 187, pp. 2827–2835, apr 2005.

[84] E. Klavins, "The aquarium project," 2014.

[85] W. Reisig and G. Rozenberg, *Lectures on Petri Nets I: Basic Models Advances in Petri Nets*. Berlin; Heidelberg: Springer-Verlag, 1998.

[86] KlavinsLab, "Klavinslab/protocols," 2014.

[87] H. H. Wang and G. M. Church, "Multiplexed genome engineering and genotyping methods," in *Methods in Enzymology*, pp. 409–426, Elsevier {BV}, 2011.

Appendix A

THYA RECOMBINING WORKFLOW

Introduction

E. coli does not naturally recombine linearized DNA into it's genome. Instead, recombinant DNA is often inserted into a cell though a circular plasmid vector. Plasmids have the advantage of being easily recombined and constructed [76], and can be easily amplified *in vivo*. Ease of insertion and modification makes plasmids the vector of choice for most of synthetic biology.

While the utility of plasmids is unquestioned, it is sometimes useful to genomically integrate changes in the genome. Modifications may include deletion of gene coding sequences, which is an evolutionarily robust strategy to remove function from a cell, or insertion of single copy genes and genetic networks.

To facilitate the recombination of DNA in bacteria, scientists have co-opted the lambda bacteriophage's recombination machinery. The lambda bacteriophage inserts its genome into the host cell's genome as part of its life cycle [77]. Lamda-mediated recombination uses the lambda phage's own insertion machinery to modify the *E. coli* genome without producing phage or killing the host cell [62].

In this work, we present a new semi-automated work flow where a genomic engineer designs linear DNA (lDNA) to edit the genome of an MG1655 derived strain of *E. coli* containing part of the lambda red genome. Once the lDNA has been designed the engineer only needs to order the oligos needed for lDNA construction and enter them into a database. From there the engineer initiates the recombination work flow from a remote computer, where a system named AQUARIUM directs technicians to carry out the series of protocols required to complete the recombination. Abstracting the wet lab work from genomic modification allows the engineer to focus on design and performance rather than construction.

Background

Recombineering

Recombineering, short for recombinogenetic engineering [78], is the process by which a bacterial chromosome or plasmid (in the context of this paper, the *E. coli* genome) is modified through the recombining of an engineered linear DNA fragment targeted by ends that are homologous to specific regions of the genome. The recombination of linear DNA in the recombineering process is mediated by the lambda red system, which consists of the genes *bet*, *exo*, and *gam*. When combined with a screening method it can be an extremely efficient tool [60, 79].

Recombineering exploits the same mechanism and proteins used by the lambda bacteriophage. The proteins Gamma, Exo, Beta, and are transiently expressed prior to insertion of linear DNA by electroporation. Gamma binds to double stranded DNA protecting it from native *E. coli* nucleases [78]. Beta binds to single stranded DNA and mediates annealing to homologous DNA [78]. Exo is a 5' exonuclease that degrades double stranded DNA into single stranded DNA [80] (Figure A.1).

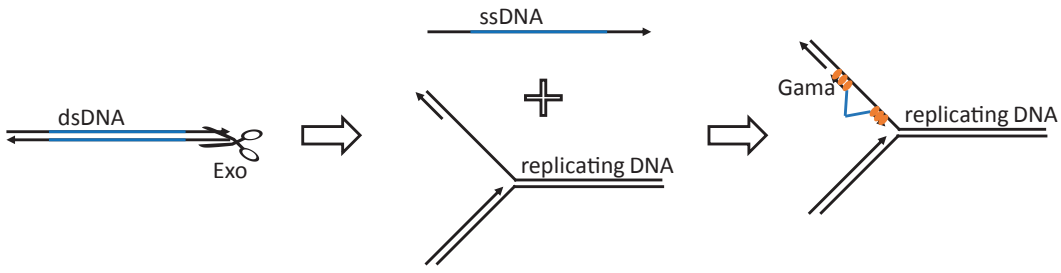

Figure A.1: Invasion of insert fragment. Double stranded DNA protected from endogenous nucleases by Beta (not shown) is degraded into single stranded DNA by Exo. The single stranded DNA may then be incorporated, with the help of Gamma, by invading the lagging strand in place of an Okazaki fragment. The resulting mismatch is either resolved though DNA repair or during the next replication event.

In 2010, Mosberg et al. showed that recombination mediated by lambda red actually undegoes a single stranded intermediate before integration into the genome [80]. In Mosberg's model, Exo degrades dsDNA into a ssDNA product, half of which are homologous to the replication fork's lagging strand. Strands with lagging strand homology can then invade in place of Okazaki fragments during DNA replication creating a hybrid DNA strand, half of which contains the insert. Mosberg's discovery explains the ability of the same lambda red system to incorporate single stranded DNA into the genome at least as easily as double stranded DNA. In fact, single base changes introduced with oligos can be incorporated with over 30% efficiency, but only when targeting the lagging strand during replication [59].

Although lambda-mediated recombineering can have efficiencies as high as 30% for single nucleotide modifications, its efficiency drops off rapidly with the size of the modification [81] and it quickly becomes impractical to screen with methods such as colony PCR. To work around this limitation, modifications are often done in a three step process [82]. In the first step, a selectable marker flanked by a loxP or frt sites is inserted, using lambda red, along with the modification. Once integrants are isolated, cre or flp recombinase efficiently removes the insert leaving either a lox or frt scar. Finally the plasmid encoding cre or flp is cured, leaving an organism with the desired modification along with a scar.

thyA selection/counterselection

Wong et al. describe a method using the single selectable/counter selectable marker *thyA* [61]. Wong's method begins with a *thyA* knockout that is auxotrophic for thymine. Selection and counter selection are then done through the inclusion and deletion of *thyA*. *thyA* expressing strains are then selected for and recovered. *thyA* is then recombined out with a PCR product only containing upstream and downstream homologies, thus creating a scar free modification.

The *thyA* gene encodes the thymidylate synthase A protein ThyA. Without ThyA, *E. coli* cannot produce thymine, an essential nucleobase, and therefore cannot replicate its DNA. Functional *thyA* genes can be selected for by plating on media deficient in thymine (including LB [83] and M9).

ThyA requires the cofactor tetrahydrofolate (THF), which it converts to dihydrofolate(DHF), in the process of creating thymidylate. THF is also important in other essential metabolic processes within *E. coli*. The antibiotic trimethoprim (TMP), disrupts the DHF reductase, folA, responsible for replenishing TMP. In the presence of TMP, ThyA expressing strains quickly exhaust their supply of THF and cannot survive. Therefore, the absence of a functional *thyA* gene can be screened on media supplemented with thymine and TMP.

AQUARIUM

Our group has developed a laboratory automation system called AQUARIUM [84]. The AQUARIUM system is composed of two main components. The first component is an inventory database, which tracks all reagents and samples used for strain construction and experiments. The second component is a protocol interpreter that executes protocols written in a scripting language and instructs technicians to execute steps. Combined, these components can be used to specify explicit workflows that have specific knowledge of the lab environment. Additionally, these workflows can be shared and executed like computer software allowing other laboratories to reproduce results without the ambiguity typically found in materials and methods sections of papers.

The AQUARIUM database stores an entry for a physical *item* as an instantiation of a *sample* definition in one of various *container* types. Items have a location, quantity, reference to their sample type, and a reference to their container. Each sample definition belongs to an abstract *sample type* definition that specifies the properties of the sample associated with them. For example a sample type definition may specify that its name is 'Primer', has a 'Tm', 'Overhang', and 'Annealing' data field, while a Primer sample will have specific values associated with each field (e.g. Tm=65 °C).

A workflow in AQUARIUM is described on two levels, with the first being a protocol. Protocols are chained together into meaningful workflows that produce products or data (e.g. PCR and run gel might be two protocols in a single workflow). An individual protocol is written in a customized version of the Ruby programming language (or a deprecated language called *Plankton*), that includes interfaces to the AQUARIUM database and the

technician. A protocol written in Ruby is composed of any number of optional components, including arbitrary ruby code, inputs, steps, inventory management, and outputs. In a typical protocol, inputs are taken and processed as needed to ensure proper execution given the context. Steps are blocking operations that render instructions to technicians in the laboratory. Steps may instruct a technician to do anything they would normally do in a wetlab including retrieving, and returning inventory, transferring reagents, and using laboratory equipment. Once a step is completed by the technician, it unblocks and execution continues. Finally, any information read, computed or in need of transfer to another protocol is returned as output.

On top of protocols are what we call *metacols*. A metacol is a Petri net [85] like description of a process composed of metacols and associated information flow. Metacols are written in a custom language called *Oyster* that describes the set of protocols to be run in a work flow, the dependencies/transition requirements for each protocol, and the dataflow between protocols.

Finally, metacol inputs may be abstracted into AQUARIUM objects called *tasks*. Tasks are typed data structures that specify all the inputs for a particular execution of a metacol. A task's prptotype will specify all fields and types for a hash that may be retrieved by a metacol. Valid entries are, numbers (used for parameters such as volumes and Tm's as well as item numbers), strings, lists, and hashes.

For example, when doing a colony PCR to validate the insertion of a construct the process may be abstracted into four protocols: `boil cells`, `run PCR`, `pour gel`, and `run gel`. The four protocols are encapsulated by one metacol that takes a list of template items (colonies or overnights), and PCR primers. The PCR primers and Tm for a particular assay may be stored in a task. Abstracting the parameters into a task allows the user to specify a task name (e.g. 'check lacZ') rather than needing to list every item and parameter needed to perform the assay. The metacol would begin by queueing the boil cells and pour gel protocols to be run by technicians because they do not depend on the output of another protocol. Once `boil cells` has completed, `run PCR` may be queued since the PCR step requires boiled template produced by `boil cells`. Finally, once both `run gel` and `pour gel` have generated their output, an item reference for the poured gel and an item reference

for the amplified DNA fragments is ready to be used as input to the `run gel`, terminating with a technician imaging the gel and sending the output to the scientist that submitted the metacol.

Results

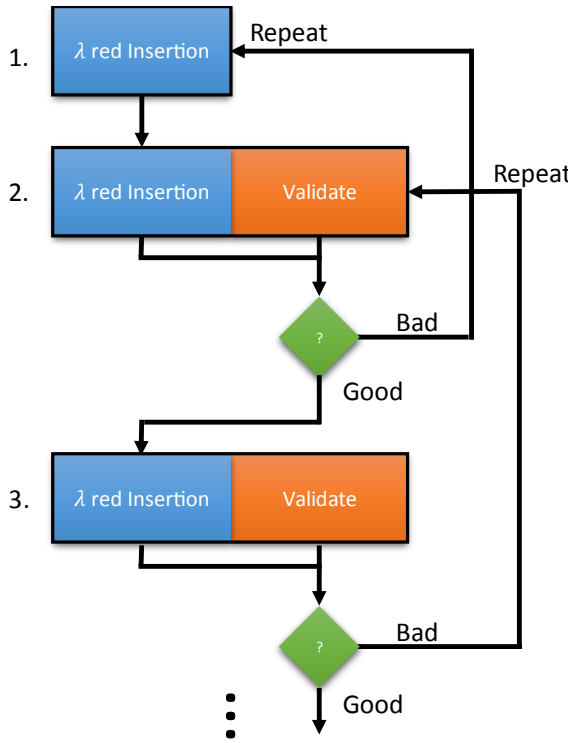

Figure A.2: Genetic modification workflow. 1. The workflow starts with a lambda red positive strain of *E. coli* with heat inducible *bet*, *exo*, and *gam* (lambda positive). A list of single stranded DNA fragments is provided to the protocol along with the names of the new strains that will be created, and a selection type (LB, or TMP+thymine). 2. The workflow is repeated with the next modification fragments plus known working fragments. If the known fragments do not create colonies of the correct phenotype then it can be assumed the input strain has lost its lambda genes and the pipeline is flushed and the process is repeated from the last know lambda positive strains. 3. The process is repeated, alternating between modification cassettes and deletion oligos, until all desired modifications have been made to the cell line.

Within AQUARIUM I have built and validated a simplified and pipelined thyA recombineering workflow that takes advantage of code reuse to implement both the insertion of a

cassette with marker, and scarless deletion with the same metacol (Figure A.2). The metacols abstract out the process of incorporating linear DNA through lambda red mediated recombination, and instead only require that the scientist design a cassette with insertion region homology for DNA insertion and an oligo with homology for scarless marker deletion. A single recombineering integration starting from an overnight culture to a glycerol stocked strain, takes four days to complete. One day is required to perform the transformation, which must be plated and left over night. An additional day is required to restreak and grow an overnight culture for any colony PCR that may be necessary. Finally 12-24 hours is needed to grow the final overnight from a PCR verified colony that has been restruck, which is then glycerol stocked. The colony restreaks are necessary to prevent non-growing but viable cells from being caried forward through the process. When doing multiple passages of the recombineering work flow, cells left over from previous cycles will grow the same as successful transformants.

The Recombinering Metacol

The recombineering metacol `recombineering.oy` consists of six individual protocols starting from an overnight culture as an input that can be created from a standard AQUARIUM protocol. The protocols, derived from Wang et al. [59] and references within, are:

1. `make_log_phase.pl` - Prepares log phase cells for transformation.
2. `finish_log_phase.pl` - Quantifies log phase cells for debug and retrospective analysis.
3. `heat_shock.pl` - Induces lambda genes
4. `quick_comp.pl` - Makes cells electro competent
5. `transform.pl` - Transforms single stranded DNA
6. `plate.pl` - Plates transformants on selection plates

The current version of the protocols are available on Github [86].

Executing `recombineering.oy`

To execute `recombineering.oy`, all the strain engineer needs to do is enter all necessary fragments into the database, define a recombineering task and run `recombineering.oy` in

AQUARIUM.

The recombineering task has the following prototype:

```
{
  "strains": [0],
  "ldna": [0],
  "plates": [""],
  "sampleName": [""]
}
```

which are index-wise related. In other words, `ldna[n]` is the linear DNA to transform into `strains[n]`, after which it will be plated on plate type `plates[n]` and given the name `sampleName[n]`.

Design Considerations

Suggested changes to ThyA recombineering protocol

While the workflow is flexible enough to accommodate the exact design and screen outlined in Strauss et al. [83], we recommend making several simplifying modifications during the design and screening process. Strauss et al. suggest using a heavily modifying minimal media as the basis for selection, while we have found that plain LB does not contain sufficient thymine to interfere with selection and can be used to screen for functional *thyA* phenotypes. Additionally, LB supplemented with $100\,\mu g\,mL^{-1}$ thymine and $50\,\mu g\,mL^{-1}$ TMP from 500x and 200x stocks respectively in DMSO is sufficient for screening *thyA* knockouts. While Strauss et al. also suggest using double stranded DNA fragments for the removal of the *thyA* cassette, we have verified that 90 base oligos are sufficient and don't require any PCR or purification.

Design of MAGE oligos

The most important feature when designing MAGE oligos is to target the lagging strand of dna replication (Figure A.3) [59, 87]. For loci clockwise of OriC to dif (replichore 1), the MAGE oligo should anneal to the + strand. For loci counterclockwise of OriC, the MAGE oligo should anneal to the - strand.

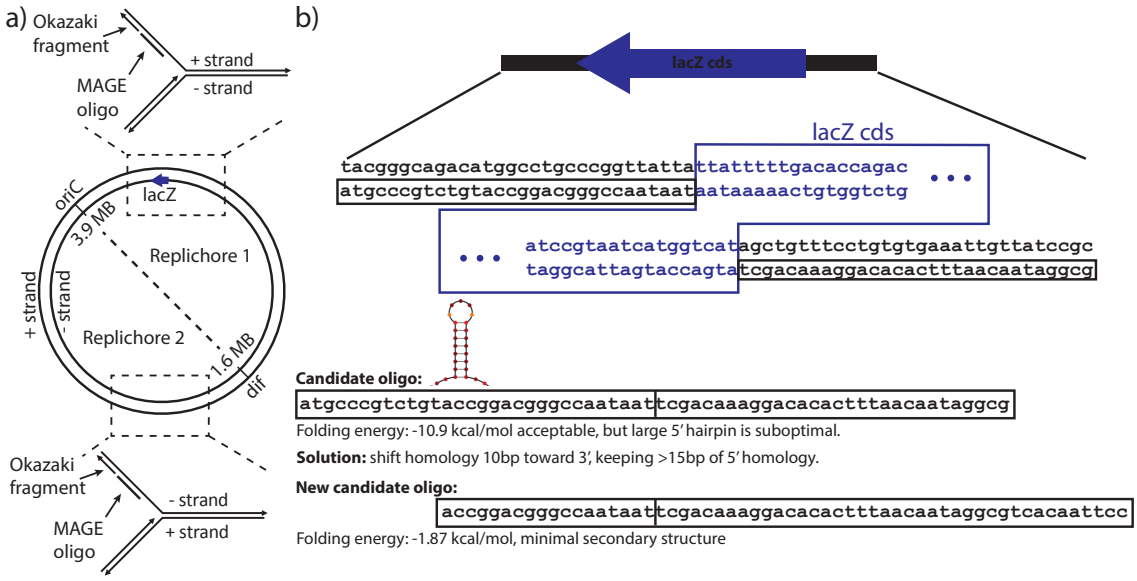

Figure A.3: Design process for MAGE oligos. a) MAGE oligos should be targeted to the lagging DNA strand for replication. The lagging strand depends on the replichore. For replichore 1 oligos should be targeted to the (+) stand. For replichore 2, oligos should be targeted to the (–) strand. b) Example design process where the coding sequence for *lacZ* has been chosen for deletion. 30 bases up and down stream are used to generate a candidate MAGE oligo. Analysis in NuPack [3] shows a folding energy of -10.9 kcal/mol, which is near the suboptimal -12.5 kcal/mol threshold, and a large hairpin near the 5' end. To design around this issue the sequence used is shifted by 10 bases toward the 5' end leaving the required >15 bases of homology.

According to Wang et al [59, 87], MAGE oligos are optimally sized at 90 bases with additional length not conferring any advantage. The 5' end should optimally contain four phosphorothioated bases (denoted by a*, t*, g*, or c* when ordering from IDT) to prevent degradation after transfection. It should be noted that these recommendations are optimal and when combined with a screen, such as that used in *thyA* recombineering, lengths can be relaxed to 60 bases and two phosphorothioated bonds.

Discussion and Conclusion

Traditionally, the majority of the work involved in strain engineering involved either wetlab work, or the careful management of technicians executing a standard set of protocols. By combining modern strain engineering techniques with streamlined protocols and AQUARIUM, we have developed a semi-automated workflow that abstracts the wetlab work from the designer, leaving more time to work on additional projects yielding higher intellectual productivity.

Future additions to the pipeline can include integration with programatic and graphical design tools such as Coral[1] and `Benchling.com` integration. With Coral and Benchling integration, primers and single stranded DNA fragments can be automatically generated from just a pair of loci and a DNA insertion sequence stored in Benchling. A strain engineer would only need to specify a start and end point for DNA replacement (start=end, would be an insertion) and an insertion sequence, which may be empty for genomic deletion. This information alone is enough to unambiguously specify the insertion fragment and selection deletion oligo.

[1]Coral is a Python package that is being actively developed in our lab by N. Bolten. It allows for the easy construction, importation, and manipulation of DNA objects in a programatic way. Integration with `benchling.com`, a graphical cloud DNA editor, is forthcoming.

Appendix B

ADDITIONAL FLEXOSTAT DESIGN AND CHARACTERIZATION

B.1 Python interface

The turbidostat software provides a simple python interface to allow the user to program control modules (modules that compute dilution rates).

Below is the stub code for the computeControl function. The computeControl function may make use of an optional state variable of user defined type State (or any builtin Python type). Each call to computeControl passes the exact State object that was returned by the last call thereby allowing a controller to keep state between function calls. Dilution rates computed by computeControl may also be functions of the OD, chamber, and current time.

```
class State:
  """ The state variable for the control function.

  This does not need to adhere to any proper interface although a
  readable __str__() method is highly recommended to allow for debugging.
  """

  def __init__(self):
    pass #any initialization code goes here

  def __str__(self):
    return " " #code for stringifying State goes here


def computeControl(self,od,z=None,chamber=0,time=0.0):
  """  Controller function

  self: self refers to the main controller object that contains
  all state such as the parameters file.  computeControl should never write
  to any members of self
  od: current od of the camber
  chamber: the chamber number indexed from zero
  time: the current time since start up.

  Returns: a tuple (list of dilution values for this chamber, state object)
  """

  #computation of dilution rate u, and state z goes here.
```

```
    return (u,z)
```

B.2 Additional Flexostat Characterization Data

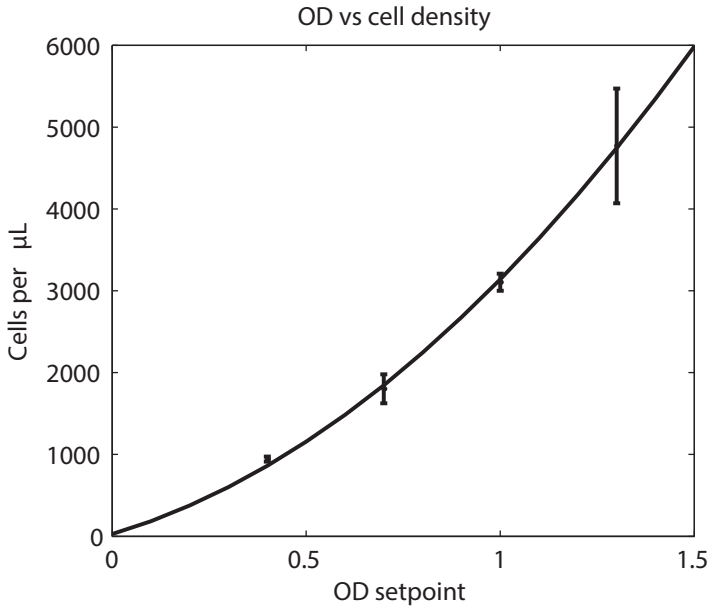

Figure B.1: The relationship between measured OD and *S. cerevisiae* cell density with the second degree polynomial fit $f(x) = 1716x^2 + 1396x + 28$.

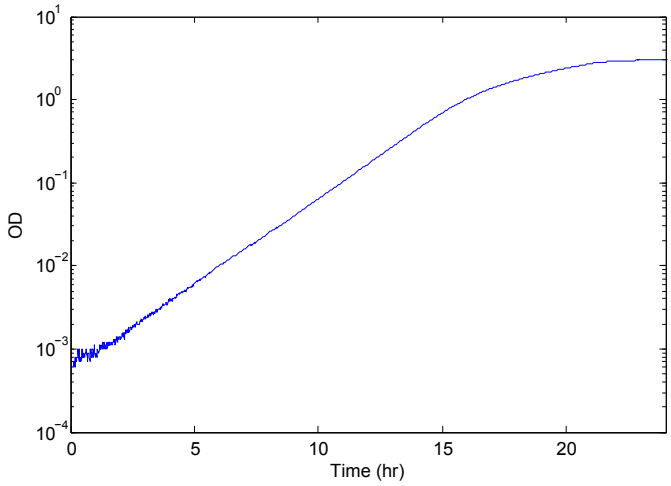

Figure B.2: A typical growth curve as measured in the Flexostat. *S. cerevisiae* was grown in synthetic complete medium at 30 C and OD measurements were recorded once per minute. A growth rate of 0.485/hr (approx 86 minute doubling time) was fit to the exponential growth phase.

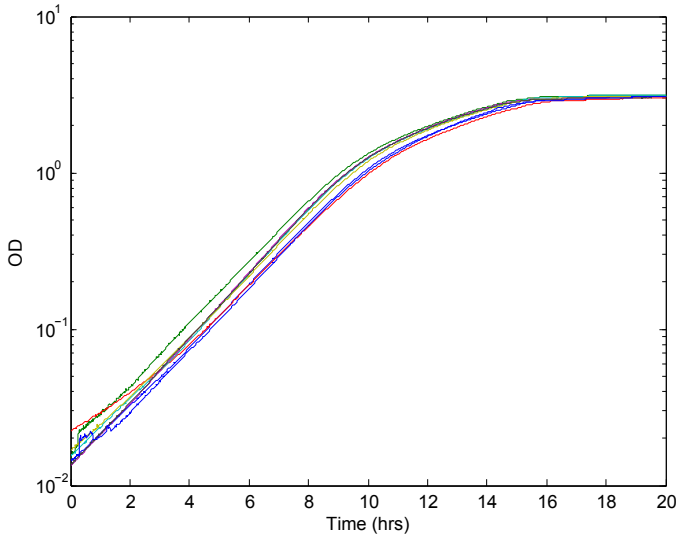

Figure B.3: Eight simultaneous growth curves under the same conditions as in figure B.2. Discrepancies between replicates can be explained by differences in inoculum volumes.

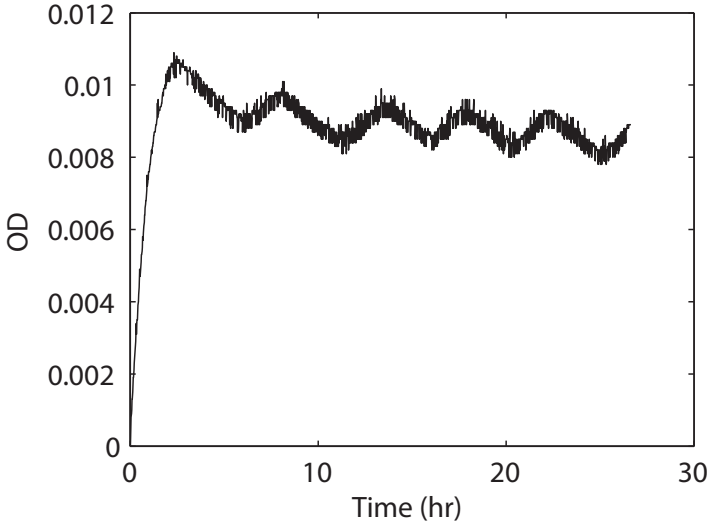

Figure B.4: A typical measurement of OD noise for the first 24 hours of operation. The initial drift ($t = [0, 3]$) is caused by the device (primarily the laser diode) reaching thermal equilibrium and can be compensated for by a preheating period before blanking and inoculation. The remaining noise (t=[3,24]), consists of a slight decaying exponential, super imposed with high frequency noise and a slow ($T \approx 5$ hour) oscillation. The high frequency noise comes primarily form the light sensors, while the slight decay comes from the incubator recovering from light temperature overshoot (approx 0.2-0.3 C). The slow oscillations come from a slightly unstable incubator controller ($\pm$0.1 C). The source of this instability likely comes from the heat propagation delay between the heating element through the water jacket to the temperature sensor. The primary source of temperature sensitivity comes from the laser diode. As with all diodes, the efficiency and therefor light output is negatively impacted by temperature. Previous design iterations that did not include a second photosensor for noise rejection where much more susceptible to temperature changes.

	ch1	ch2	ch3	ch4	ch5	ch6	ch7	ch8
Openloop STD (OD$\times 10^{-3}$)	0.227	0.558	0.294	0.297	0.432	0.217	0.474	0.391
Pump rates (μL/unit)	0.49	1.47	1.37	1.51	1.6	1.58	1.58	1.53
Pump rate STD (nL/unit)	335.4	52	68.6	26.6	79.9	24.2	44.3	43.8

Table B.1: Chamber by chamber for OD noise and pump rates. Open-loop STD measured in milli OD units represents the standard deviation of measurement noise in each chamber after the initial warm up period. The pump rate measurement is the average pump volume in micro liters per dispense unit using a NORM-JECT 3 ml syringe computed from the data in Figure B.8. The pump rate STD is the standard deviation of the pump rates in figure B.8 computed through bootstrapping.

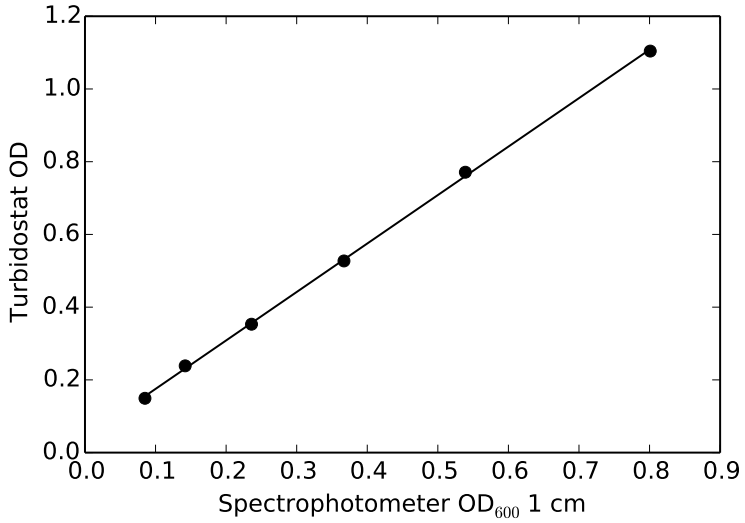

Figure B.5: Spectrophotometer (Spec.) vs Flexostat OD measurements. MG1655 derived *E. coli* strain BF003 was grown to stationary in M9 minimal medium and serially diluted in m9-salts. Each dilution was measured by both the turbidostat and the Edmunds Optics BRC111A-USB-UV/VIS spec. (dots). A constant conversion factor (Turbidostat/Spec) of 1.33 was then fit by linear regression (line).

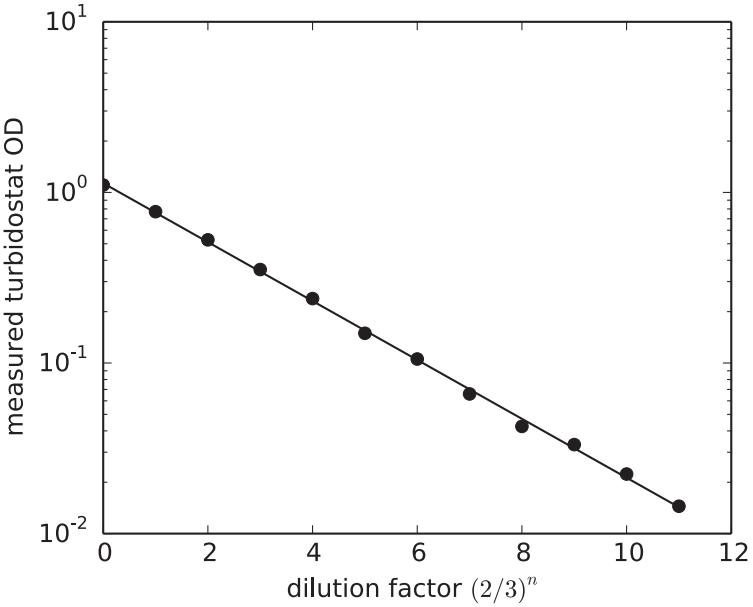

Figure B.6: Twelve serial dilutions (1:2, M9-salts:culture) of the culture in figure B.5 were measured in the turbidostat to demonstate linearity over two orders of magnitude.

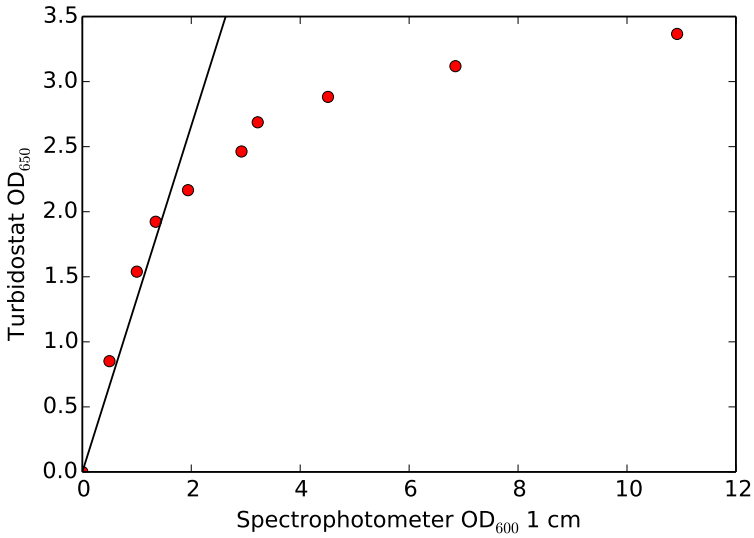

Figure B.7: To determine the linear range of the device's absorbance measurement stationary phase *E. coli* was diluted from approximately OD_{600} 10 down to OD_{600} 0.5. These reference samples were measured both in our spectrometer (diluted into the linear range) and the turbidostat (undiluted) (red dots). Coplotting the points against the linear conversion factor computed in supplemental figure B.5 we determined the linear range of our device to be between OD 0.0 and 2.0.

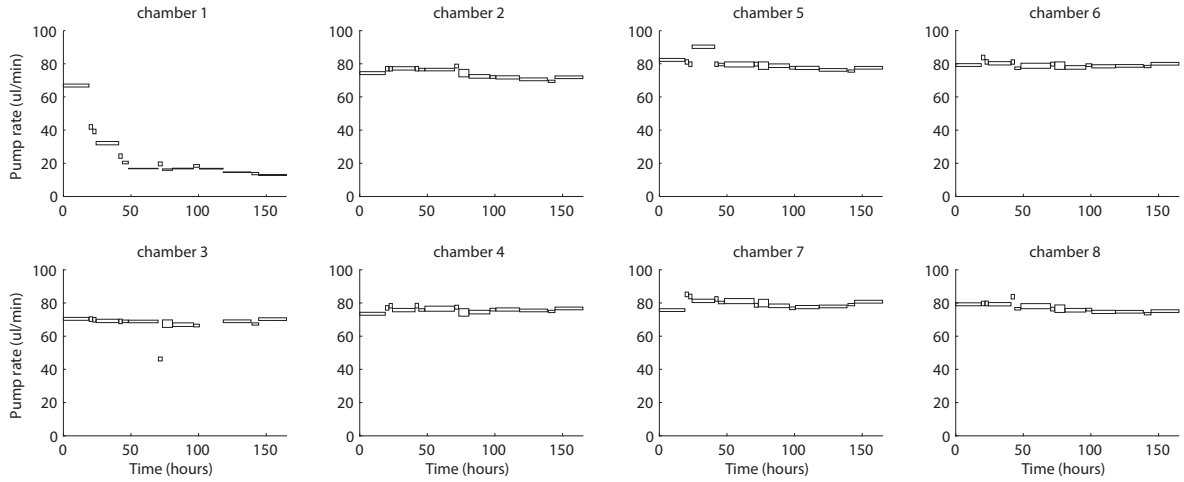

Figure B.8: The chamber by chamber pump rates over a 160 hour period. The Turbidostat was set at a constant 50 unit dilution rate and effluent was periodically collected and measured in a graduated cylinder. The width of each box represents the collection time while the height represents the accuracy of the graduated cylinder used (i.e. one graduation). Chamber 1 is the first chamber to be dispensed into and is therefore the chamber that is subjected to hysteretic effects of the syringe plunger stretching. All experiments in this paper other than the one depicted here are preformed with an additional redispense step where 100units of media are pumped back into the media bottle. This redispense step fully compensates for all mechanical hysteresis.

B.3 Parameter dependence on cell density

Table B.2: Individual k_5 values for each experiment shown in figure 2.4c

k_5	Replicate 1	Replicate 2
Batch	0.0706	0.0608
OD 0.4	0.0407	0.0361
OD 0.7	0.0519	0.0537
OD 1.0	0.0795	0.0705
OD 1.3	0.1603	0.1711

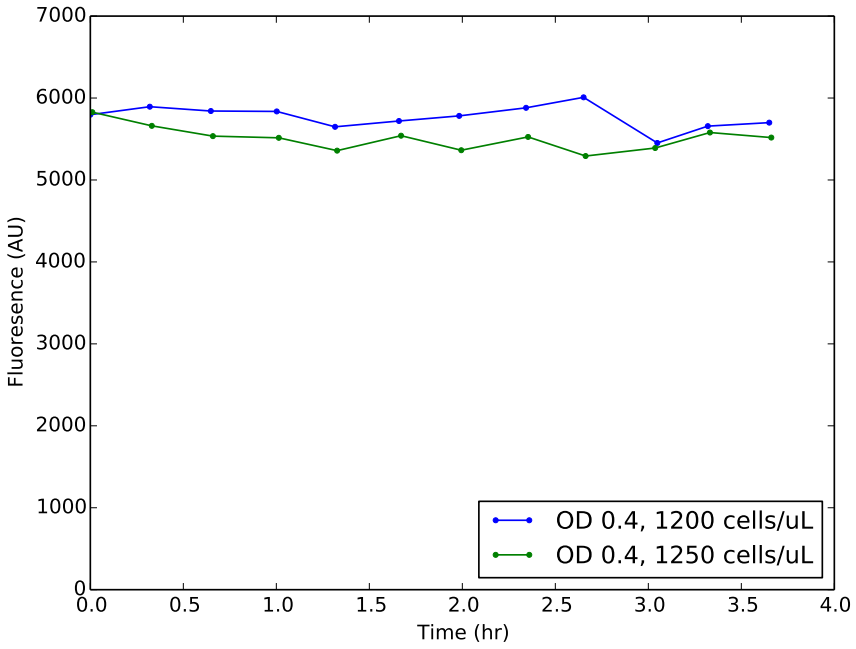

Figure B.9: *S. cerevisiae* strain YKL73's steady state fluorescence (without auxin) showing no significant change in fluorescence without treatment over a multi hour timescale. YKL73 was grown in the turbidostat at OD 0.4 for 2 days prior to fluorescence measurement. An identical model but different cytometer was used to obtain this data making direct fluorescence comparison's impossible.

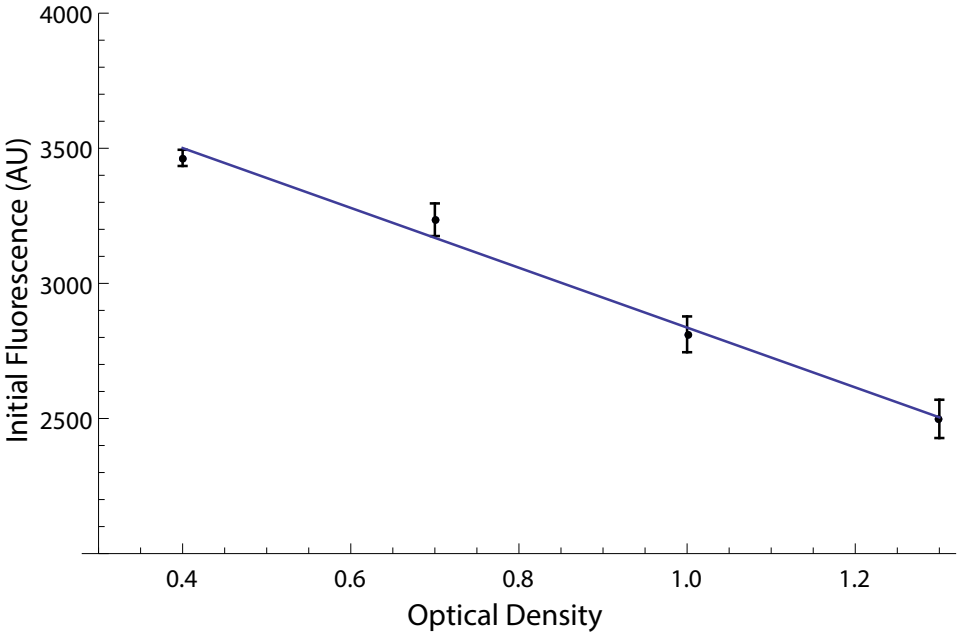

Figure B.10: Initial fluorescence plotted as a function of OD for the data in figure 2.4b. The affine function $y = 3944 - 1107x$ was fit to the data.

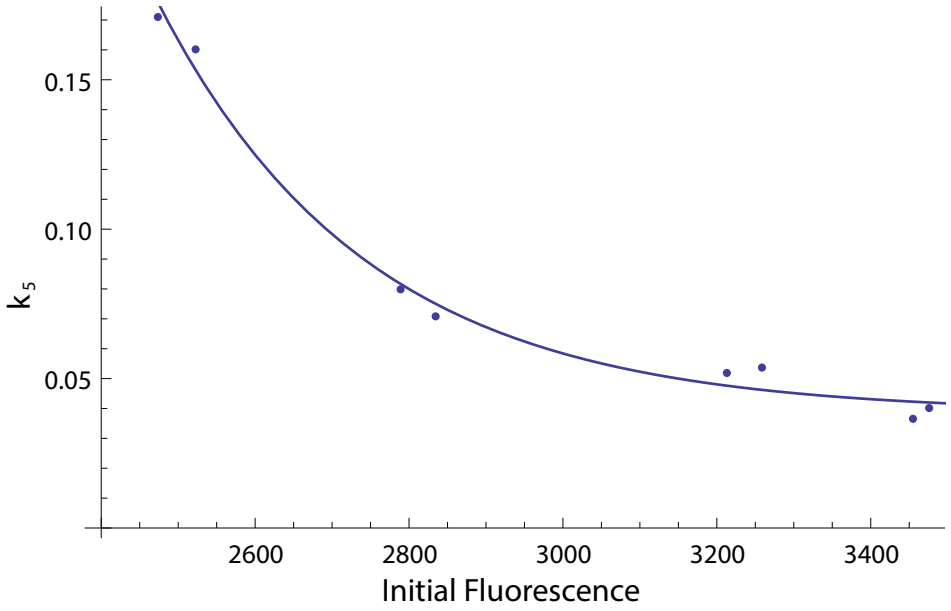

Figure B.11: k_5 plotted as a function of initial fluorescence (dots). A fit was found to the exponential function $y = 0.03854 + 1210e^{-3.67\times10^{-3}x}$ (line).

B.4 Fluorostat

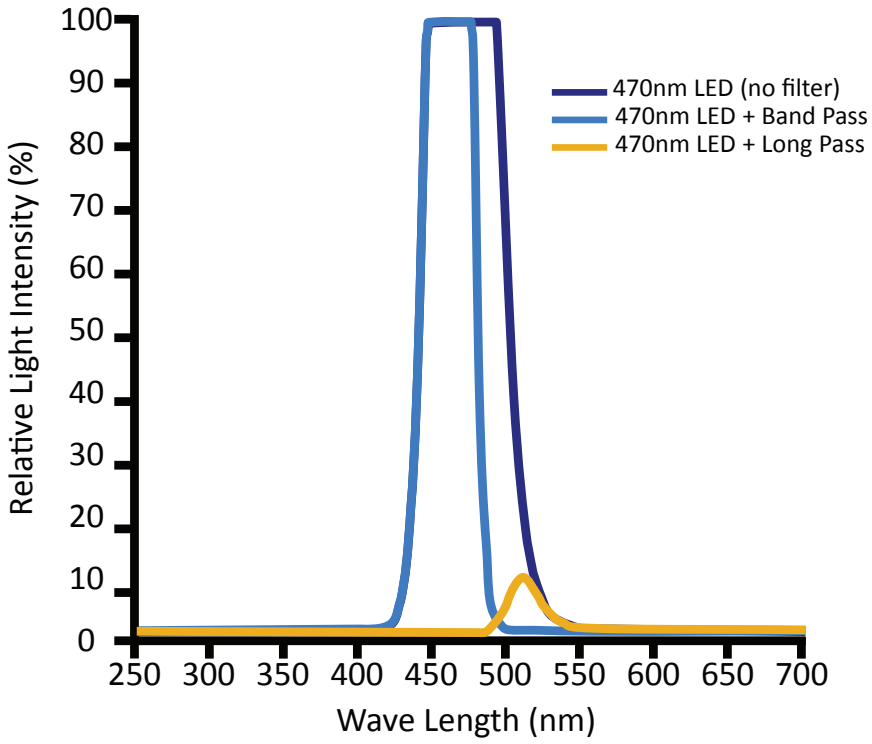

Figure B.12: Measured spectrum of excitation LED (dark blue) through filters. The Bandpass filter removes longer wavelengths emitted by the LED (light blue) that have the potential to leak into the long pass filter's pass band (yellow). No significant light is transmitted though the combination of both filters allowing only light generated though florescence to be measured.

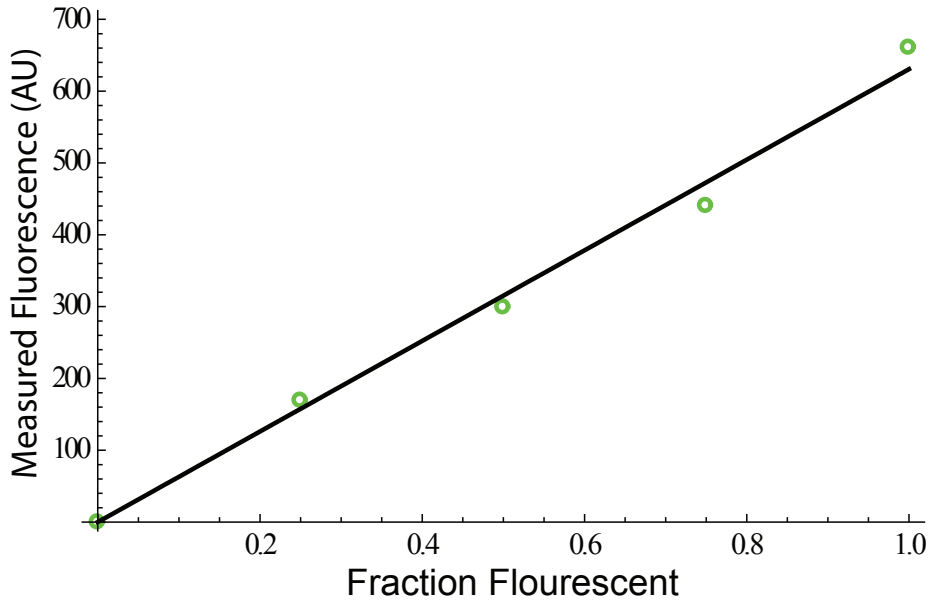

Figure B.13: Stationary fluorescent *E. coli* were mixed with stationary wild type cells to create cultures of varying fluorescent intensity and measured in the fluorostat. Autofluorescence was determined by measuring the wild type cells and subtracted from each measurement (green circles). The points were then fit to a linear model (black line).

B.5 3D models

All 3D models are available on the website.

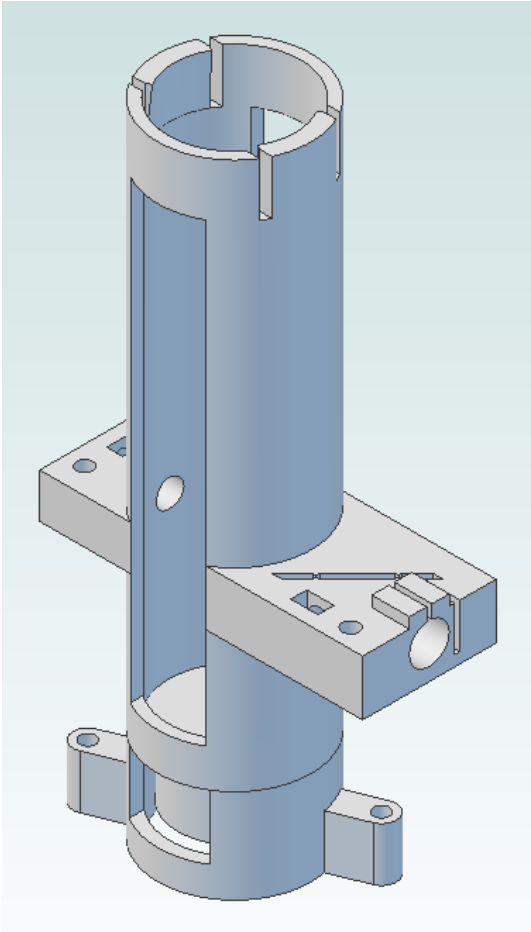

Figure B.14: Drawing of all 3D printed parts in the main chamber assembly.

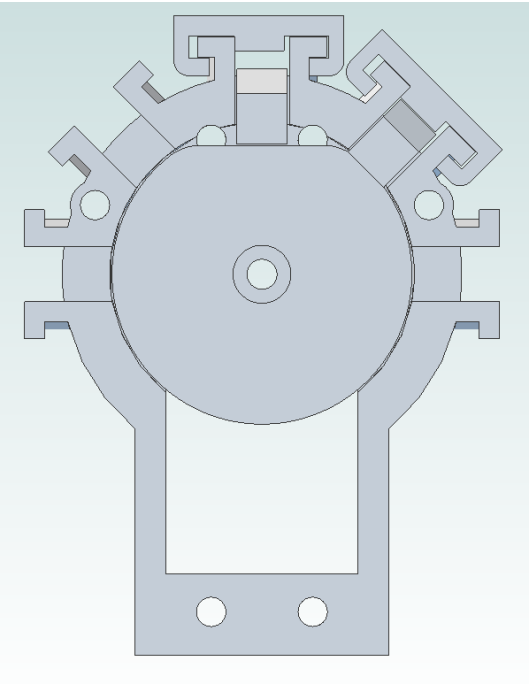

Figure B.15: Drawing of 3D printed pinch valve assembly with face removed. The pinchers and center cam are laser cut from Delrin while all other parts are 3D printed. The left slot is normally left unused to provide a position where all valves are closed. Shown in the assembly are two assembled pinchers. The top pincher is in the open position while the upper right pincher is in the closed position. Tubes are fed through on the axis normal to the page.

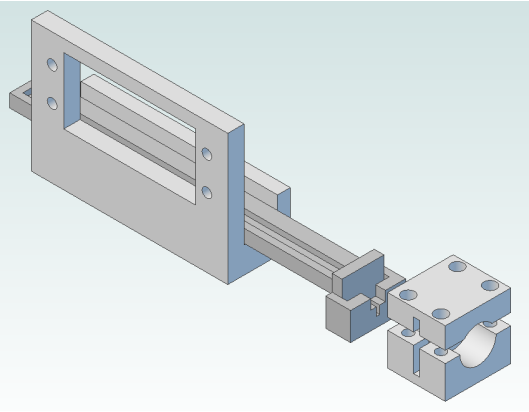

Figure B.16: Drawing of the 3D printed syringe pump components. A servo motor actuates the slide attached to the syringe piston while the syringe body is clamped in place.

B.6 Electrical Circuits

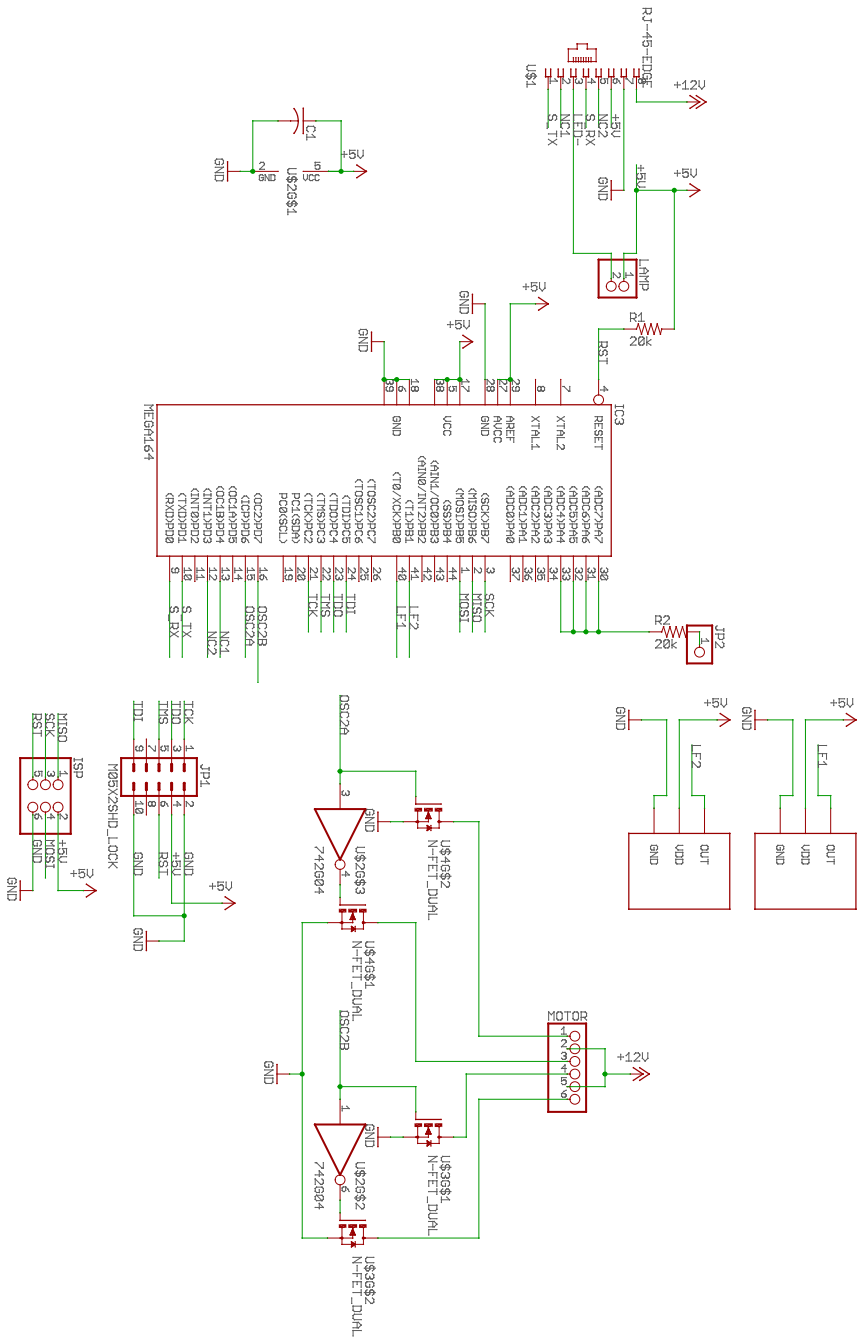

Figure B.17: Schematic diagram for the chamber electronics. This circuit controls stirring speed and takes light measurements from each light sensor.

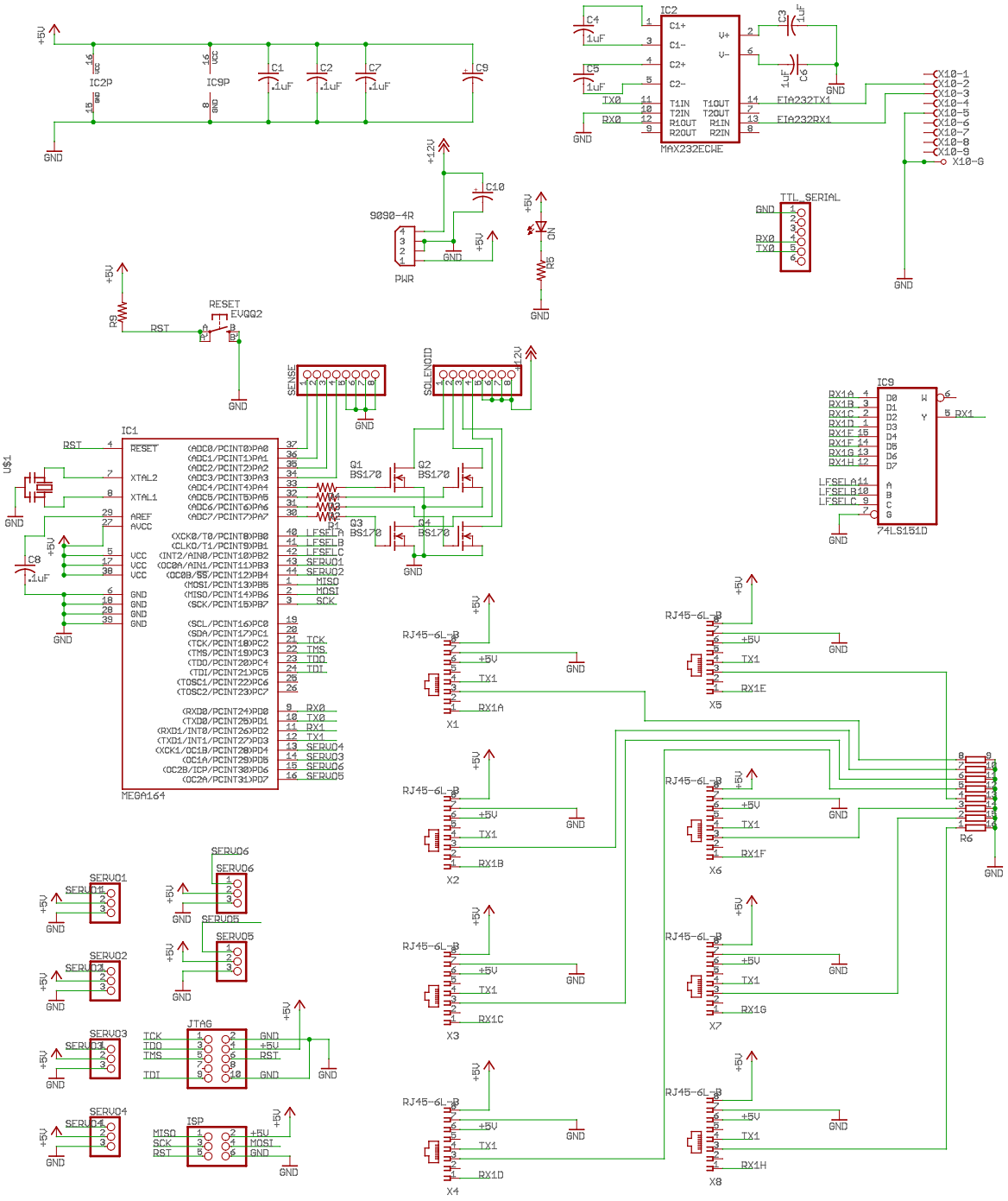

Figure B.18: Schematic diagram for the main board electronics. The main board routes all communications between the chambers and controls all valves and pumps.

VITA

Chris Takahashi grew up in the Pacific Northwest, which is where he has spend the majority of his life. After getting bachelors degrees in computer engineering and electrical engineering at the University of Washington, he took a brief detour to the University of Michigan for his masters degree in control theory from the department of EE: Systems before returning to UW for his PhD.